Dynamic Response to Wet Deck Slamming

A Fast Numerical Method for a Heavy-Lift Catamaran in Head Seas

K.R. Baggus

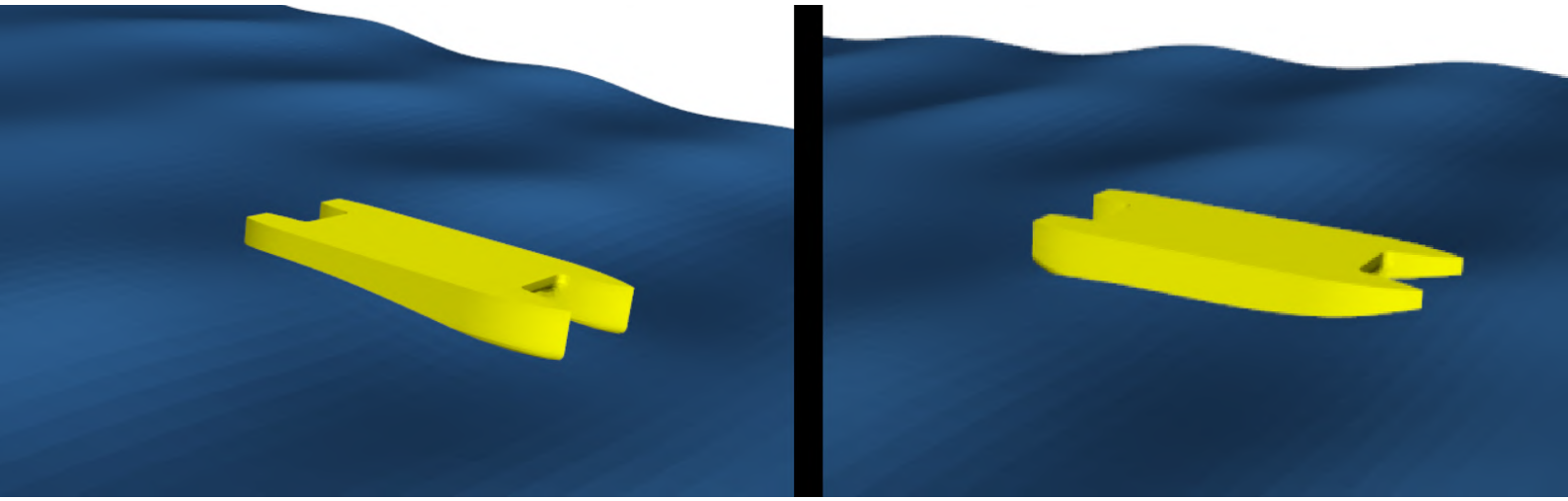

TU Delft

VUYK ENGINEERING

Thesis for the degree of MSc in Marine Technology in the specialisation of
Ship and Offshore Structures and *Ship Hydromechanics*

Dynamic Response to Wet Deck Slamming

A Fast Numerical Method for a Heavy-Lift Catamaran in Head Seas

by

K.R. Baggus

Performed at

Vuyk Engineering Rotterdam

This thesis **MT.24/25.047.M** is classified as confidential in accordance with the general conditions for projects performed by the TUDelft

to be defended publicly on Wednesday 23rd of July, 2025 at 1:00 PM.

Company supervisors
Daily Supervisor: Ir. M.P.G.J. Verdult

Thesis exam committee
Chair/Responsible Professor: Dr. A. Grammatikopoulos
Staff Member: Dr. H.C. Seyffert
Company Member: Ir. M.P.G.J. Verdult

Author Details
Student number: 4998987
Author contact e-mail: Koen@baggus.net

Cover: Motions resulting from wave excitation calculated with Capytaine

An electronic version of this thesis is available at `http://repository.tudelft.nl/`.

TU Delft

VUYK ENGINEERING

Preface

The start of my academic journey can be traced back to a young age. All the technical subjects throughout elementary and high school piqued my interest. Aside from my technical interest, I inherited my parents' passion for water and boats by sailing on their over 100-year-old 'ijsselaak'. So, when it was time to choose a study direction, the combination of a technical study and ships seemed logical. Although initially, there was much doubt whether this was the study for me. Over time, I became increasingly interested and did not mind the long hours. Ultimately, it was the right fit, but I do have to thank some people for their help along the way.

To begin, I want to express my gratitude to Apostolos Grammatikopoulos and Michiel Verdult for their guidance and discussions throughout the project. They showed me that it's essential to be critical of your results, but also remain hopeful that in the end, it will work out.

Secondly, I would like to thank Anabel Keser and Michael Katsouros. Anabel created the flexible model and did a great deal of the legwork on the structural modelling. Michael conducted experimental slamming measurements on the model, which results allow for validating my proposed numerical model. Without either contribution, the project would not have been possible in the available time frame.

I would like to thank Harleigh Seyffert for serving on the graduation committee; her constructive feedback on the thesis was invaluable, significantly enhancing the coherence and readability of this thesis.

The next word of thanks goes out to all the incredible people I have met at D.S.R. Proteus-Eretes, the student rowing association, both from rowing myself and coaching crews. I have gained many unforgettable memories, and these have also helped me through the tough study days.

Lastly, I would like to thank my parents and sister for their unwavering support over the years and for always being a warm place to come home to after being away for a while.

K.R. Baggus
Delft, July 2025

Abstract

In offshore construction, there is a demand for vessels with ample deck space. Large catamarans could provide larger deck space for the same tonnage. However, one operational concern for catamarans is wet deck slamming. Wave impact with the wet deck can excite the global flexible vibration modes of the vessel. While extensively studied for high-speed catamarans, the dynamic response induced by slamming in large, slow-moving, heavy-lift catamarans remains poorly understood.

This thesis presents a fast numerical method for predicting the dynamic response of a heavy-lift catamaran subjected to wet deck slamming in head seas. The method combines Capytaine, a BEM potential flow solver, with ANSYS Mechanical, a finite element software package. ANSYS calculates the dry modal properties, and Capytaine includes the water effects to obtain the wet modal properties. Capytaine also finds the rigid body motions resulting from wave loading. A simplified slamming pressure formulation based on immersion velocity and wetted length is applied. Both monochromatic and bichromatic wave conditions are investigated to assess their influence on the immersion behaviour.

It was found that monochromatic waves produce immersion of long duration. The proposed method cannot accurately determine forces and responses due to the varying properties during a slamming event. Additionally, the limited impulse can not effectively excite the eigenmodes due to the long wetting time compared to the natural periods. In contrast, bichromatic wave conditions lead to shorter and more severe immersion events. For the bichromatic wave loading, the modal dynamic oscillatory response was found as a result of wet deck immersion.

To assess the accuracy of the proposed numerical method, a validation against experimental measurements is performed. The comparison focused on accelerations resulting from slamming events and the intervals between such events. The resulting accelerations of the proposed numerical method slightly underestimated the measured accelerations. One problematic finding was that significant slamming events could disrupt the vessel's oscillatory motions and that resolving the disruption cannot be achieved in the frequency domain. The proposed numerical method can be used to identify conditions where slamming can be problematic quickly. However, to obtain accurate displacements, accelerations, and stresses, further analysis by another method is required.

The thesis provided insight into the dynamic behaviour of a heavy-lift catamaran induced by slamming. An indication of slamming effects can be calculated in the early design stages. More importantly, identifying problematic wave loading cases can be done at a relatively low numerical cost. The exact magnitude of the slamming effects requires a more detailed time-domain analysis.

Contents

List of Figures

List of Tables

Nomenclature

Abbreviations

Abbreviation	Definition
BEM	Boundary Element Method
CFD	Computational Fluid Dynamics
DIC	Direct Image Correlation
DOF	Degrees of Freedom
FEM	Finite Element Method
FS	Full Scale
FSI	Fluid Structure Interactions
IE	Instantaneous Energy
LCG	Longitudinal centre of gravity
MS	Model Scale
RAO	Response Amplitude Operator
RANS	Reynolds Averaged Navier Stokes
TCG	Transverse Centre of Gravity
VCG	Vertical Centre of Gravity

Symbols

Symbol	Definition	Unit
a	Amplitude mode shape	[-]
a_p	Accelerations of sensor p	[m/s^2]
$[A]$	Added mass matrix	[kg]
B	Breadth	[m]
$[C]$	Added stiffness matrix	[N/m]
D	Depth	[m]
f	Frequency	[Hz]
g	Gravity	[m/s^2]
h	Water depth	[m]
k	Wave number	[1/m]
L	Length	[m]
M	Mass	[kg]
$[K]$	Stiffness matrix	[N/m]
$[M]$	Mass matrix	[kg]
p	Pressure	[N/m^2]
T	Draft	[m]
U	Forward speed	[m/s]
u_{flow}	Flow speed	[m/s]
V	Slamming velocity	[m/s]
$\vec{u}$	Displacement vector	[m]
z_{rel}	Relative wave height	[m]
z_{vel}, w_{rel}	Relative velocity	[m/s]
δ	Dirac delta impulse	[-]
ϵ	Phase	[rad]
λ	Scaling factor	[-]

Symbol	Definition	Unit
λ_ζ	Wave length	[m]
μ	Dynamic viscosity	[kg/(ms)]
ϕ	Velocity potential	[m^2/s]
Ψ	Mode shape	[m]
ρ	Density	[kg/m^3]
ω	Angular frequency	[rad/s]
ζ_a	Wave amplitude	[m]

1. Introduction

In offshore construction, there is a demand for vessels with ample deck space. Catamarans could provide such deck space, but the application of this hull type is not typical for heavy-lifting vessels. Part of the reason is the inexperience with catamarans as heavy-lifting vessels. To create a safe ship design, it is essential to evaluate the various types of loading that the vessel may experience throughout its lifetime. For catamarans, there is a loading case that other vessels do not experience. Where the bottom of the cross deck, also known as the wet deck, comes in contact with water. This immersion into the water can create a slam when the vessel and the wave surface collide at a significant speed. There are two consequences to slamming: the first is the high local pressures resulting from the slam, and the second is the excitation of global flexible behaviour. The latter is of particular interest in this thesis.

The goal is to investigate the dynamic response resulting from wet deck slamming. For this, a fast numerical calculation method is desired during the early design stages. The problem of slamming and subsequent responses is one where the fluid and structure interact, a research field also known as Fluid-Structure Interactions (FSI) or hydroelasticity.

Recent research on cross-deck slamming has focused primarily on high-speed catamarans. Only a minimal amount of research is conducted on large heavy-lift catamarans, which operate at lower speeds compared to naval or ferry applications. It is unknown whether heavy-lift catamarans are susceptible to whipping effects due to slamming.

This thesis addresses this research gap by developing a fast numerical method to predict the slamming-induced dynamic response of a heavy-lift catamaran operating in head seas. The method integrates a potential flow BEM solver with flexible modal response data from FEM analysis, incorporating a simplified slamming pressure formulation based on immersion velocity and wetted length. Both monochromatic and bichromatic wave loading is considered to assess the influence of wave interference patterns on slamming events.

The numerical predictions are compared with available measurements of accelerations and possible whipping effects. The measurements were taken on a scaled, fully flexible model developed in earlier research by Keser [1]. The findings contribute to a better understanding of the dynamic behaviour of large catamarans subjected to wet deck slamming. First, a brief literature review will discuss relevant findings related to this topic.

1.1. Numerical Slamming

Slamming is an event of high-pressure loading with a very short duration compared to periodic wave excitation. For this thesis, cross-deck slamming, also known as wet deck slamming, is the focus. Fundamental slamming concepts are based on momentum theory, which relates displaced water to pressures or forces on the structure. From experimental research, it was found that as long as the angle between the water surface and the impacting element is greater than 5° air compression is not significant for the flow behaviour [2].

1.1.1. Fluid Modelling

The effect of water slamming against the structure results from motions excited by wave loading and fluid behaviour close to the vessel. There are various ways to model the fluid Reynolds-Averaged Navier-Stokes (RANS)-based Computational Fluid Dynamics (CFD). While CFD offers considerable freedom, the setup time and computational cost are significant. Due to large differences in length scales that are important in RANS-CFD analysis, there is some trouble with scaling CFD results from the model to full scale. The long setup time and high computational cost are especially undesirable in the early design stages.

Another much quicker method is solving fluid problems with a Boundary Element Method (BEM) solver. The BEM solver combines sources and sinks so that no fluid propagates through the hull, making the hull watertight. The application of Green's function for sources and sinks eliminates the need for meshing the free surface and seabed. The conditions for BEM with Green's source are listed below:

- The flow is inviscid
- The flow is incompressible
- The sea bed is watertight
- The ship hull is watertight
- No disturbances far away from the ship
- The pressure at the free surface is atmospheric
- The particles at the free surface stay there (kinematic boundary condition)

With these requirements, the question arises how they relate to the problem at hand. Various experiments show good agreement with potential flow solvers, even though eddies occur on the surface [3]. It indicates that the inviscid assumption is acceptable, introducing limited error. As mentioned at the start of the section, the incompressible assumption holds for impact angles greater than 5°.

The only constraining requirement is related to the kinematic boundary condition. If breaking waves occur in the applied wave loading, the kinematic boundary condition no longer holds. In experimental measurements on the model executed by Katsouros [4], breaking waves were not noted. The numerical model is validated using experimental measurements from Katsouros. Since no comments were made on breaking waves, it is assumed that for the tested wave heights, this constraint will hold.

A BEM solver can incorporate nonlinearities, such as the second-order wave force and the instantaneous wetted surface. However, these methods require solving in the time domain [5]. Solving in the time domain increases the computational cost significantly, although an initial linear frequency domain solution can partially mitigate the increase in computation cost. The increased computational cost directly results from calculating the source strength again for each time step. In the frequency domain, the calculation of source strengths is performed only once.

1.1.2. Structural Modelling

A structural model is required to reflect the structure response to the loading. The derivation of displacements, accelerations and stresses is then possible with structural models, the last of which is most useful during ship design. Common methods for determining displacement and stresses include beam models. Where the complex ship structure is simplified to a beam with similar properties. The most basic is the Euler-Bernoulli beam, which accounts for bending moments. A further improvement is the Timoshenko beam, which also considers shear effects. A Vlasov beam approximation should be applied when torsional effects are essential. It can include non-symmetric deformation in open cross-sections. The various beam methods mentioned are continuous over the beam. Another option is a Discrete modular beam, where rigid sections are coupled with a stiffness matrix that represents the structural properties. With all the mentioned beam methods, it is possible to have varying properties over the ship's length.

One problem with beam models for catamarans is that there are two demi-hulls. A possibility is to model each demi-hull as one beam with some transverse coupling between the two beams; However, if global bending behaviour and its resulting stresses are desired. It is likely a poor method for observing behaviour in the cross-deck. Another method is to reduce the model into finite elements and calculate the result over each small section. Finite element software reduces the complex geometry into a system of equations with corresponding boundary conditions. Solving the system of equations yields displacements, which allow for the calculation of stresses, strains, and accelerations. For acceleration, a time-dependent component is important. While for evaluating static stresses and strains, the response can also be calculated quasi-statically.

One method that takes into account the dynamics is a modal analysis. Here, instead of solving the problem in the time domain, the frequency domain is utilised. The modal response analysis significantly reduces the degrees of freedom of each node to just a few mode shapes. A property of eigenmodes is that they are orthogonal. This property allows for the superposition of the different eigenmodes. This relation works both ways, where a force signal can be decomposed into the excitation of various eigenmodes.

The superposition of oscillating eigenmodes with their corresponding eigenfrequencies enables the evaluation of the total response in a modal analysis. Such a method is highly effective for periodic loading, short impulse loading, and investigating subsequent oscillations.

1.1.3. Whipping

Detection of slamming events can be useful in determining the vessel's response to waves. The evaluation of response to the waves and slamming can be more effectively achieved through whipping-based slamming criteria. Whipping here means the excitation of the flexible behaviour of the hull. Whipping measurements implicitly consider the transfer of momentum in slamming events. Dessi [6] proposed two criteria based on vertical bending moment and its directional derivative exceeding a threshold. But these two criteria are closely linearly correlated, thus they are reduced to one criterion 1.1 for whipping identification [6]. $\hat{M}_y(t)$ is the peak vertical bending moment and η is the threshold value. The threshold value should be set at the greatest quasi-static load. When this is exceeded, it results from dynamic whipping behaviour.

$$\hat{M}_y(t) \geq \eta \tag{1.1}$$

Another method for identifying whipping is through empirical modal decomposition, where the intrinsic mode functions are extracted from the oscillatory signal [7]. From the IMF, a spectral density can be calculated. A filter is required to remove the rigid behaviour. With a subsequent Hilbert transform, the Instantaneous Energy (IE) can be calculated. A peak in IE at the natural eigenfrequencies indicates the excitation of the flexible modes and whipping of the hull.

1.2. Fluid-Structure Interactions

During ship design, the structure is assumed to be rigid in hydromechanical motion analysis. In the structural analysis, static and dynamic pressures resulting from motion calculations are applied to assess the structure's response to waves. The field of Fluid-Structure Interactions (FSI) examines the relationship between hydromechanical and structural calculations.

FSI has recently garnered attention in research and design for several key reasons. Large ships are generally more flexible, which increases the likelihood that the encounter frequency of typical wave spectra will align with the vessel's structural natural frequencies. Additionally, the use of high-tensile steel reduces the total weight and increases the hull's flexibility. The last reason of interest is the interrelated effects when faced with significant dynamic behaviour. The interaction can be either one-way or two-way coupled. In literature, the latter is often referred to as hydroelasticity. Bereznitski [8] investigated local slamming effects and found that fluid-structure interaction should be considered when the duration of the slamming impact is very short. The criteria in equation 1.2 relate the slam duration to the first natural frequency of the structure. If true, FSI likely impacts the loading and response of the hull.

$$T_{slam}/T_{\omega 0} \leq 2 \tag{1.2}$$

1.2.1. Effects of Hydroelasticity in Slamming

Faltinsen wrote his review article on hydroelastic slamming that: "The slamming problem must be hydrodynamically studied from a structural point of view" [9]. The reason that it is primarily a hydrodynamic study is that the structure does not undergo significant deflections. Nevertheless, the displacements and vibrations do affect the flow and loading. Faltinsen further found that local hydroelastic effects are not essential in global hydroelastic analysis [9].

Unit Impulse

The response to a unit impulse method examines a ship where a Dirac delta impulse $\delta(t)$ applies an instantaneous unit force. When the impulse is applied along all longitudinal wetted coordinates n, the application is expressed in the form described by equation 1.3. Here, $\vec{F_\delta}$ represents the unit impulse and $\dot{\vec{z}}(x')$ is the vertical velocity. Note that both $\vec{F_\delta}$ and $\dot{\vec{z}}$ are vectors of length n corresponding to each

coordinate.

$$\vec{F_\delta} = \dot{\vec{z}}(x')\delta(t) \tag{1.3}$$

Equation 1.3 is then used as forced loading in the equation of motion, resulting in a system of equations as described by equation 1.4. Subsequently, this equation is manipulated by a Fourier transform and the Hamiltonian method to find the impulse response matrix $[\mathbf{h}]$. $[\mathbf{h}]$ can be multiplied by the unit impulse and motion/shear force distribution to obtain the representative value over time. For a complete derivation, see chapter 9.2 in the book by Bishop and Price [10]. It is important to note that this mathematical formulation is only valid for a ship sailing at constant speed in flat, calm water.

$$[M + A(\omega_e)]\ddot{u}(t) + [D(\omega_e)]\dot{u}(t) + [K + C]u(t) = \vec{F_\delta} e^{-i\omega_e t} \tag{1.4}$$

Slamming in Regular Waves

The unit impulse method mentioned in the previous section is not applicable in regular waves. Bottom slamming occurs when the hull of a vessel is lifted out of the water. This happens when the relative wave amplitude $z_{rel}(x,t)$ exceeds the local draught $T(x)$. When this situation arises, the relative velocity $Dz_{rel}(x,t)/Dt$, and acceleration $D^2 z_{rel}(x,t)/Dt^2$ become crucial in determining the loading on the structure. The derivative in equation 1.6 also accounts for the forward speed.

$$z_{rel}(x,t) = z(x,t) - \zeta(x,t) \tag{1.5}$$

$$\frac{D}{Dt} = \frac{\partial}{\partial t} - U\frac{\partial}{\partial x} \tag{1.6}$$

The impact slamming theory method connects the wetting of the hull to the slam impact force. It involves discretising a section of the hull that transitions from an unwetted to a wetted state, which is then applied as a forced loading (equation 1.8). Once the hull becomes wetted, the ship's dynamics are calculated as a free beam.

$$p(x,t) = \frac{1}{2}\rho k_1 |Dz_{rel}(x,t)/Dt|^2 \tag{1.7}$$

$$F(x,t) = \frac{p_{max}}{T_0} G(x) t e^{(1-t/T_0)} \tag{1.8}$$

In Equations 1.7 and 1.8 z_{rel} represents the relative vertical position of the water, U is the forward ship speed, $G(x)$ is a shape function and T_0 is the duration between slam and maximum loading. T_0 is vessel dependent; to indicate the order of magnitude, T_0 was 10 milliseconds for a destroyer [10].

The momentum slamming method combines the transient force's time history with the change of momentum in the surrounding fluid, as well as immediate buoyancy effects. The hull is discretised into transverse strips, on which momentum evaluation is conducted.

$$F(x,t) = -\{\frac{D}{Dt}[m(x,t)\frac{D}{Dt}z_{rel}(x,t)] - \rho g S(x,t)\} \tag{1.9}$$

Here $m(x,t)$ represents the water mass affected by the hull vibration, $S(x,t)$ is the wetted cross-sectional area.

Differences 2D and 3D Hydroelasticity

The methods developed by Bishop and Price rely on a 2D assumption [10]. In their method, the ship is simplified to a beam, allowing hydrodynamic evaluations to be performed on strips.

While modelling the hull as a beam is effective for monohulls and facilitates 2D calculations, this approach is insufficient for assessing global loads for multi-hull vessels or semi-submersibles. For such cases, 3D evaluation of dynamic behaviour induced by waves is necessary. To extend the 2D methods, the hull needs to be discretised in panels instead of strips.

The general system of equations is evaluated in other research. The key difference lies in the inclusion of 3D effects and the use of numerical methods to assess the force.

1.3. Current Research on Cross-Deck Slamming

Most research related to slamming of the cross-deck has been conducted on high-speed catamarans with a wave-piercing hull design. The application of high-speed catamarans used as ferries or military platforms. Davis and Whelan [11] found that for such high-speed catamarans, air entrapment was important for the slamming problem. However, this was for a case in following seas where the high-speed catamaran would dive into the subsequent wave. Julianto et al. [12] found that the two-way coupling of FSI has little effect on the slamming force but does affect the vertical bending moment. The effect on vertical bending moments implies that the coupling impacts the transfer of momentum between the water and the structure.

Haugen [13] conducted research on the slamming of stiffened plates for a catamaran's wet deck. She identified three critical parameters for hydroelastic behaviour and stresses: the relative normal velocity, global accelerations, and relative angle. Davis et al. [14] investigated 25 parameters for a catamaran in random head seas. They found, through a combination of Pearcon's and Spearman's rank correlation, the following nine potentially impactful parameters:

1. Relative normal velocity
2. Global accelerations
3. Relative angle
4. Maximum relative velocity prior to slam
5. Maximum pitch angle prior to slam
6. Pitch velocity at slam instant
7. Slam location
8. Forward speed
9. Maximum pitch velocity

Experimental Research

To validate the numerical results, experiments are conducted on physical models. The most common experimental method to investigate hydroelastic behaviour is with a flexible backbone model. In such a model, rigid sections are then connected to a continuous beam. A scaled-down model is towed in a wave tank that simulates wave loading at sea. A relatively new method involves creating a fully elastic model. The fully flexible model should be more accurate in incorporating all flexible FSI effects. There is one caveat: a flexible model also introduces some uncertainty in the results, as a representative model is more challenging and impacts the analysis. One flexible model is a heavy-lift catamaran with scaled stiffness, developed by Keser [1]. Slamming behaviour on the flexible catamaran model was further investigated by Katsouros [4]. In model tests, Katsouros measured the accelerations and global whipping effects of the catamaran for bichromatic wave loading.

1.4. Research Proposal

Knowledge gap

Regarding slamming, extensive experimental and numerical research has been conducted. The findings have also been applied to wet deck slamming. However, the emphasis was on high-speed catamarans in previous work. For this thesis, the vessel considered is a heavy-lift catamaran sailing at a lower speed. Measurement data is available for slamming on a fully flexible heavy-lifting catamaran model. However, a numerical slamming investigation for a heavy-lifting catamaran is yet to be conducted. The difference in sailing speed and less extreme motions and flow phenomena could enable a more efficient numerical model in the frequency domain. Furthermore, for such a heavy-lifting catamaran, it has not yet been researched whether hydroelastic effects are significant and should be addressed in the load modelling.

Research Question

From the assessed knowledge gap, the main research question became: *"What are the characteristics of the structural dynamic response of a heavy lift catamaran induced by wet deck slamming?"*

With the following sub-questions:

- What is an efficient numerical method for evaluating the occurrence of slamming and the response induced by slamming?
- To what extent does a numerical two-way coupling influence the slamming-induced response?

- How does the numerical slamming-induced response relate to experimental data?
- Is a heavy-lifting catamaran experiencing whipping due to wet deck slamming?

1.5. Methodology

The proposed workflow is shown in Figure 1.1. The corresponding chapters and sections are also mentioned in square brackets. From a structural space-claim model, two meshes are created. A structural mesh and a hydromechanical mesh. This is because different requirements are desired from the hydro and structural meshes for further computation. On the structural mesh, a modal analysis is performed in ANSYS to obtain the natural frequencies and dry mode shapes that represent the oscillatory behaviour of the structure. A hydromechanical mesh is created in Rhino 7, which will subsequently be used in Capytaine. Capytaine is an open-source BEM solver written in Python. Capytaine shows good potential for incorporating flexible modal behaviour. Combined with dry modal data from Ansys, Capytaine yields wet mode shapes and wet natural frequencies.

Separately, Capytaine was used for a rigid motion analysis, in which the immersion of the wet deck will be investigated. Data related to immersion will be converted to loading through a Wagner pressure formulation, which is based on the wetted length and impact velocities.

A Python code was written that combined the rigid slam loadings with the wet modal data, yielding the excitation of flexible response. An additional iteration over the slamming load calculation utilising the flexible response will yield a two-way coupled response analysis.

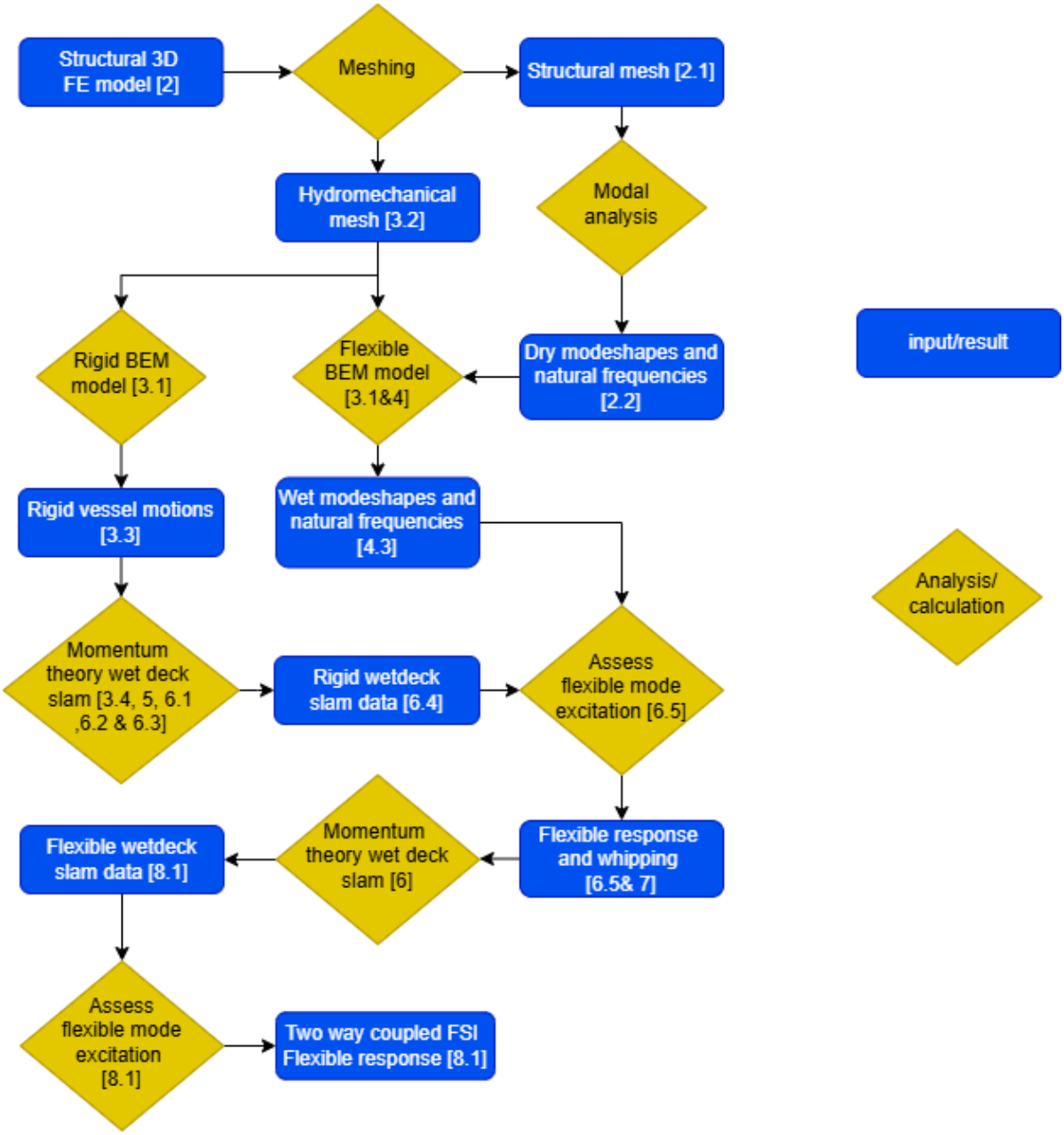

Figure 1.1: Flow chart of model, calculations and results. In square brackets the relevant chapters and sections are mentioned

2. Structural Model

Keser [1] created a 3D-printed flexible model of a heavy-lift catamaran for experimental research into wet deck slamming. By adjusting the thickness of the shell plating, the scaled stiffness was representative on the structural level of girders and panels. The various scaling factors for Froude scaling are listed in Table 2.1. It was not possible to include the details on the stiffener level due to limitations on minimum printing thickness.

Table 2.1: Scaling factors for Froude scaling

property	Acceleration	Density	Force	Frequency	Length	Mass	Speed	Stiffness (EI)
SI-units	m/s^2	kg/m^3	N	$1/s$	m	kg	m/s	Nm^2
Scaling factor	λ^0	λ^0	λ^3	$1/\sqrt{\lambda}$	λ	λ^3	$\sqrt{\lambda}$	λ^5

The design and properties of the heavy-lift catamaran used are listed in Table 2.2. Only the total weight differed from the design; the impact will be further discussed in Section 7.2. This design of the heavy-lift catamaran is utilised since experimental measurements of this model were available for subsequent validation of the numerical slamming model.

Table 2.2: Heavy lift catamaran properties at full-scale and model-scale

Property	Full scale	Model scale target	Model scale as produced
L	198 m	1100 mm	1100 mm
B	90 m	500 mm	500 mm
D	26 m	144.4 mm	144.4 mm
T	10.5 m	58.3 mm	58.3 mm
M	84662 ton	14.52 kg	15.89 kg
LCG	96 m	533.3 mm	534 mm
TCG	0 m	0 mm	-2.9 mm
VCG	25 m	138.9 mm	140 mm

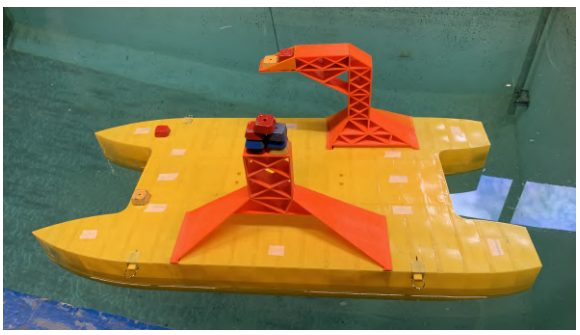

(a) "Fully elastic model after production"[1]

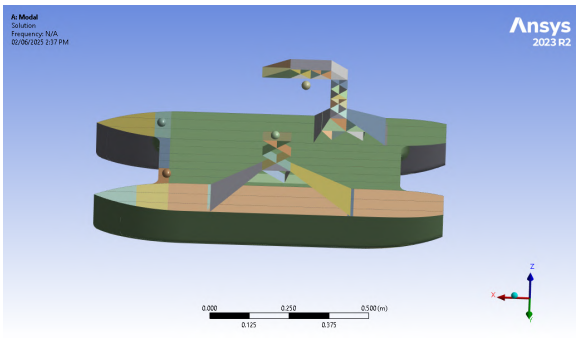

(b) ANSYS scaled down model

Figure 2.1: The physical experimental and numerical reference model

2.1. Structural Mesh

To apply a Finite Element Method (FEM) the structure is divided into smaller elements; this process is called meshing. To minimise computational cost, it is desirable to use the largest mesh size possible. The problem with too big elements is that local phenomena might not be accurately represented. Therefore, there is an upper limit to the mesh sizing for accurate results. Another vital factor for a trustworthy finite element analysis is that the hull, girders and decks of the structural mesh are connected. In Figure 2.2, the mesh created in ANSYS is displayed. The connections between elements are displayed in various colours. Black is desired for continuous panels, purple indicates a connection between the hull and a deck or girder. Yellow connections are expected at the bottom of the bilge radius. At that line, a deck within the demi-hull joins the vertical part of the hull and the start of the bilge radius. Additionally, Figure 2.2 displays the internal structure. The purple and yellow which also shows the positions of the decks, longitudinal and transverse girders.

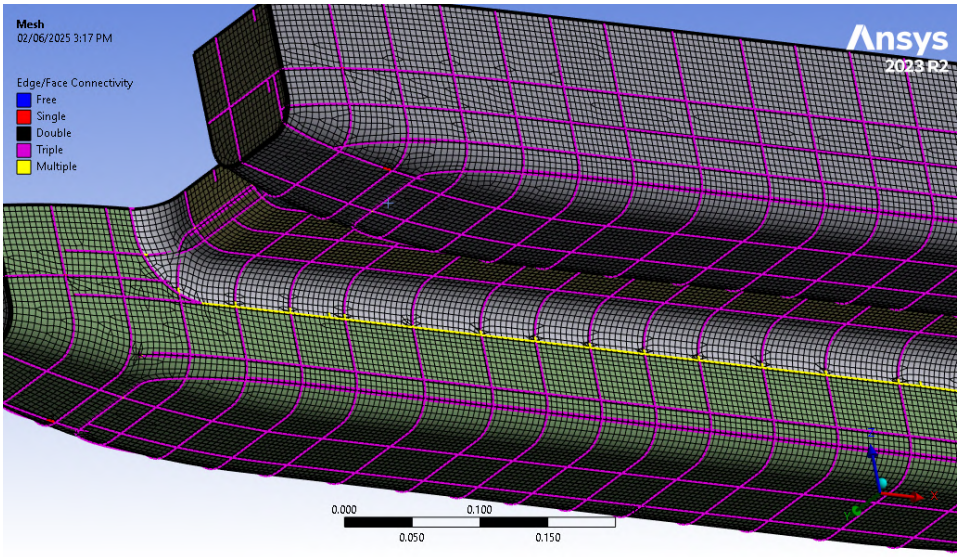

Figure 2.2: Mesh used in ANSYS highlighting no over-connections (yellow colour) in the bilge radius. Additionally, the purple and yellow connections display the internal structure.

There was a balance between the size of the elements and the connections between them. The way the different elements are connected is based on distance; elements are linked when the distance is within a specified tolerance. When regions of smaller elements were defined, several connections would bunch together. In Figure 2.2, this can already be seen where some elements connecting the bilge radius are incorrectly connected. The incorrect connections introduce a modelling error. The mesh sizing was optimised to ensure as few disconnected elements as possible and to minimise incorrect connections; adjustments were required to reduce the modelling error, but many connections on curved sections were problematic for meshed elements smaller than 2.5 mm. Keser [1] conducted a modal analysis on the physical model, which showed agreement between the physical model and the numerical ANSYS model for the used mesh size. The mesh size and connection tolerance used were 5 mm and 0.5 mm, respectively. Of the 160 thousand elements, the number of disconnected ones was on the order of 10, located in various parts of the hull. The elements were of type SHELL181, which can model linear and rotational deformations well for 6 Degrees of Freedom (DOF). Shell elements are commonly used in ship modelling, as the thickness is relatively thin compared to the length and width of the plates. This reduces the numerical cost but removes information about through-thickness stress distributions. This is no problem except for a local fatigue analysis on a structural detail. At that point, it would be numerically more efficient to model only the detail.

2.2. Dry Modal Analysis

In a modal analysis, the equation of motion (Equation 2.1) is reduced to Equation 2.2. This simplification is possible since the frequencies and mode shapes are independent of applied loads. Ignoring the damping as the total full-scale damping is small; up to 3% in unfavourable conditions [15]. In the excitation phase, damping makes a minimal contribution, and omitting it yields a conservative estimate. However, damping is a crucial factor in the response decay following the excitation phase. The inclusion of damping will be further discussed in Section 6.5.3.

The reduced equation of motion creates an eigenvalue problem that can be solved for n degrees of freedom, resulting in n eigenmodes. Each eigenmode has a corresponding eigenvalue λ and an eigenvector $\vec{v}$ of size n. A property of eigenmodes is that each eigenvector is orthogonal. The orthogonality means that a superposition of eigenmodes can express each displacement or loading state of the hull. In modal analysis, the eigenvector is referred to as the mode shape characterised by the sign Ψ_i. The eigenvalues are expressed as the eigenfrequency ω_i, where the subscript i refers to the ith mode.

$$[M_m]\ddot{\vec{u}} + [D_m]\dot{\vec{u}} + [K_m]\vec{u} = \vec{f}(t) \tag{2.1}$$

$$[M_m]\ddot{\vec{u}} + [K_m]\vec{u} = \vec{0} \tag{2.2}$$

The displacements can be separated into an uncoupled time- and space-dependent part displayed in Equation 2.3. In calculations, the mode shapes Ψ_n are often normalised so that the largest positional displacement is 1. The excitation of the mode shapes is then taken into account by the $a_n(t)$ term. Together $\Psi(\vec{x})$ and $a_n(t)$ return the actual displacement of the mode at that time. Summing all modes yields the total displacements of a point at a time. It should also be noted that $\vec{x}$ is a vector, as this is not limited to one dimension.

$$\vec{u}(t, \vec{x}) = \sum a_n(t) \cdot \Psi_n(\vec{x}) \tag{2.3}$$

Then the $[M_m]$ and $[K_m]$ matrices represent the modal mass and stiffness obtained by Equations 2.4 and 2.5.

$$[M_m] = \vec{\Psi}_T[M]\vec{\Psi} \tag{2.4}$$

$$[K_m] = \vec{\Psi}_T[K]\vec{\Psi} \tag{2.5}$$

The modal motion equation should be adjusted to include a force loading to investigate the excitation of the modes. In equation 2.6, the modal force is added to the modal motion equation. The modal force $\vec{f_m}$ maps the force from physical space to the modal system through Equation 2.7.

$$[M_m]\ddot{\vec{u}} + [K_m]\vec{u} = \vec{f_m}(t) \tag{2.6}$$

$$\vec{f_m}(t)_= \vec{\Psi}_T\vec{f}(t) \tag{2.7}$$

In ANSYS, the node IDs, positions and modal displacements of the modes with the 10 lowest eigenfrequencies are calculated and extracted in the format shown in Equations 2.8 and 2.9. The first six modes represent rigid body translations and rotations with eigenfrequencies very close to zero. The following four modes are the different flexible modes and are of most interest in the analysis of flexible behaviour. In a flexible BEM analysis into stresses Iijima [16] found that the inclusion of additional modes rapidly converges. The first three flexible modes already achieved an error of less than 3% for stresses. The choice of four flexible modes is a result of the availability of validation data of the experimental model by Keser [1] and Katsouros [4]. Additional modes would marginally increase the accuracy but come at quite a considerable computational cost.

$$position_n = [I\vec{D}_n, \vec{x_n}, \vec{y_n}, \vec{z_n}] \tag{2.8}$$

$$displacements_{n,i} = [I\vec{D}_n, \vec{ux}_{n,i}, \vec{uy}_{n,i}, \vec{uz}_{n,i}] \tag{2.9}$$

The first four flexible modes are displayed in Figure 2.3. The elements with attached point masses are modelled as rigid. This choice resulted from the lead blocks being significantly larger than a point mass, which added rigidity to the connected elements. Elastic modelling of point masses and the

superstructure primarily yielded mode shapes with unrealistic local excitation of point masses. The primary focus is on the hull's response. Therefore, the crane and superstructure were modelled as rigid connections, taking into account the masses. The magnitude of the largest displacements varies for each flexible mode. Currently, the modes are scaled to have unit mass. The scaling itself does not matter as long as a consistent unit system is applied.

It can be seen that the first flexible mode (Figure 2.3a) is a combination of the two demi hulls pitching in opposite directions and an inward rotation about the longitudinal axis. The second flexible mode (Figure 2.3b) is purely the two demi-hulls pitching in opposite directions. The third flexible mode (Figure 2.3c) is mainly a result of the opposite heaving of both demi-hulls with a small hogging contribution of the starboard demi-hull. The fourth flexible mode is mainly a sagging motion of the starboard demi-hull.

The small displacements of the port side demi-hull are a result of the significant stiffness added by the superstructure. On the starboard demi-hull, the crane has a much smaller footprint (Figure 2.1). Resulting in greater displacement in the starboard demi-hull.

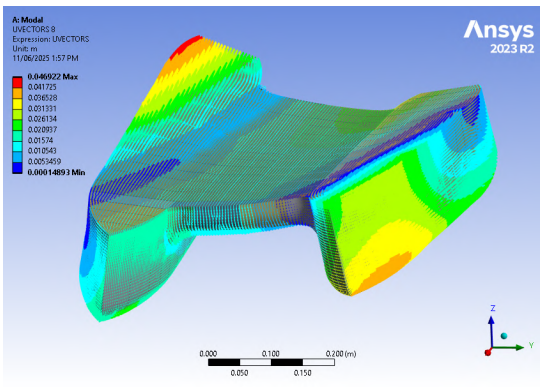

(a) ANSYS displacement vectors of the first flexible mode with $f_{dry,1} = 21.65$ Hz

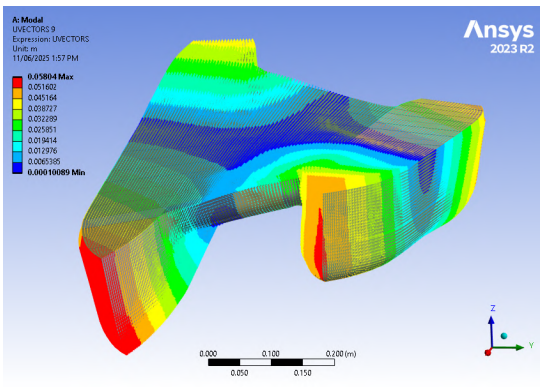

(b) ANSYS displacement vectors of the second flexible mode with $f_{dry,2} = 23.69$ Hz

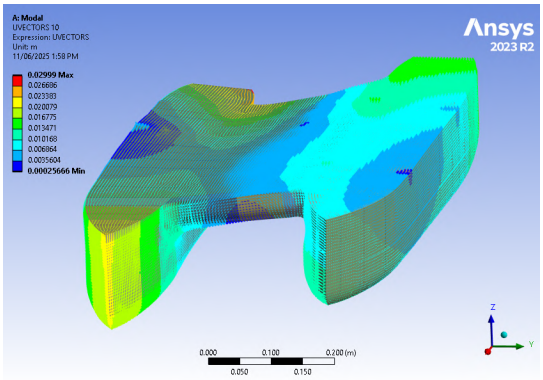

(c) ANSYS displacement vectors of the third flexible mode with $f_{dry,3} = 39.86$ Hz

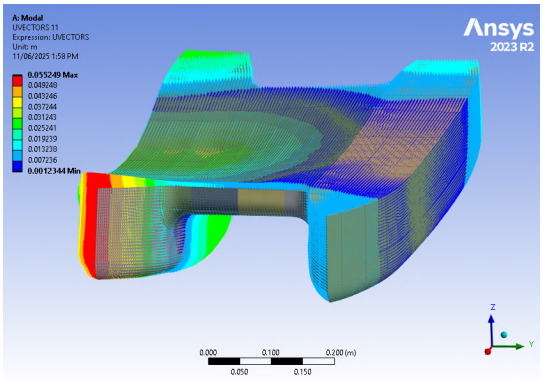

(d) ANSYS displacement vectors of the fourth flexible mode with $f_{dry,4} = 44.14$Hz

Figure 2.3: Exaggerated deformations of first four flexible modes shapes and natural frequencies.

3. Hydromechanical Model

For modelling the fluid behaviour, Capytaine is utilised. It is a relatively new open-source Python package with its origins in Nemoh, an older, more established Boundary Element Method (BEM) potential flow solver written in Fortran. Computational Fluid Dynamics (CFD) can include viscous effects within a flow. The inclusion of viscous terms incurs a significant computational cost, as it necessitates solving the problem in the time domain. BEM employs several mathematical properties to reduce numerical intensity by resolving the fluid problem in the frequency domain.

3.1. Theory Boundary Element Method

All Newtonian fluid problems can be accurately described by the Navier-Stokes Equation 3.1. This is the most general fluid model, but it is also a nonlinear vector equation. To numerically resolve the flow, simplifications must be made.

$$\rho(\overbrace{\frac{\partial \vec{u}_{flow}}{\partial t}}^{\text{Unsteady term}} + \underbrace{\vec{u}_{flow} \cdot \nabla \vec{u}_{flow}}_{\text{Convection term}}) = \overbrace{-\vec{\nabla} p}^{\text{Pressure term}} + \underbrace{\rho g \hat{z}}_{\text{Gravity term}} + \overbrace{\mu \nabla^2 \vec{u}_{flow}}^{\text{Viscous term}} \tag{3.1}$$

The first simplification is an assumption that the flow is incompressible, which is very accurate to a Mach number of 0.3. The lower limit at which compressibility starts affecting the flow's behaviour is at a speed of over 450 m/s. The second simplification is to assume the flow is inviscid, where $\mu \to 0$. As a result of no friction, it is only a small assumption that flow is irrotational. Non-uniform flow speeds are unable to create vorticity. In reality, there are some viscous effects in the flow, as friction causes eddies near the boundary layer of the hull. However, it should be noted that these are small enough that the assumption of $\Gamma \to 0$ can yield meaningful results.

These simplifications form the basis of potential flow theory. The velocity potential is a function of space and time. The potential function $\phi(x, y, z, t)$ is such that the derivatives in space yield the local flow velocity (Equation 3.2). The main benefit of potential flow is that the time trace of the exact fluid motions is not required. Changes in the potential then describe the flow, independent of time. If these changes are expressed in the frequency domain, the resulting forces and motions will also be in the frequency domain.

$$u = \frac{\partial \phi}{\partial x}, \;\; v = \frac{\partial \phi}{\partial y}, \;\; w = \frac{\partial \phi}{\partial z} \tag{3.2}$$

The assumptions from potential flow are then:

- The flow is incompressible $\vec{\nabla} \cdot \vec{u}_{flow} = 0$
- The fluid is irrotational $\vec{\nabla} \times \vec{u}_{flow} = 0$
- The fluid is inviscid $\mu = 0$

3.1.1. Application Potential Flow

The hull and boundaries are discretised into panels. On each panel, either a source or a sink is located. In BEM, the resulting Partial Differential Equations (PDEs) are solved numerically. These PDEs are formulated in integral form, allowing for integration over the boundary. The BEM solver's objective is to balance all sources and sinks, ensuring that there is no penetration of water through the panels of the ship's hull. This means that the fluid velocity acting on the panels is equal to the normal velocity of the panel. The resulting fluid velocities are therefore equal to the ship's motion. The balancing of potentials resulting from ship motions is called the radiation problem, and balancing with wave potential

is referred to as the diffraction problem. Both will be further discussed in section 3.1.2. The result of the diffraction and radiation problem is a Response Amplitude Operator, which defines the motions in relation to the applied wave amplitude and frequency. However, there is a limit. If the wave amplitude approaches 1/7th of the wave length λ_ζ, the wave breaks, and the linear wave assumption no longer holds.

In the application of potential flow, the following assumptions are added:

- The ship hull is watertight
- The sea bottom is flat and watertight
- Wave amplitude ζ_a should not exceed $\lambda_\zeta/7$

3.1.2. Capytaine Mathematics

For a linear problem, a solution in the frequency domain requires the least amount of computation. The velocity potential is then defined as Equation 3.3.

$$\phi = Re(\Phi e^{-i\omega t}) \tag{3.3}$$

The partial differential equations are then Equation 3.4 for a linearised free surface boundary condition, Equation 3.5 for no velocity condition on the sea bottom located at -h and Equation 3.6 for the normal velocity on the wetted body surface S. Here $\hat{\vec{n}}$ is the vector normal to surface S at the considered position.

$$g\frac{\partial \Phi}{\partial z} - \omega^2\Phi = 0, \quad \text{on } z = 0 \tag{3.4}$$

$$\frac{\partial \Phi}{\partial z} = 0, \quad \text{on } z = -h \tag{3.5}$$

$$\vec{\nabla}\Phi \cdot \hat{\vec{n}} = \vec{u} \cdot \hat{\vec{n}}, \quad \text{on } S \tag{3.6}$$

Radiation problem

Regarding the Radiation potential, the potential is calculated as a result of movement along one degree of freedom. The watertight hull combined with the condition on the normal velocity at the wetted surface yields the Laplace problem in Equation 3.7. Solving the Laplace problem allows for the derivation of the added mass and radiation damping for the considered degree of freedom.

$$\vec{\nabla}^2\phi = 0 \tag{3.7}$$

Diffraction Problem

Capytaine considers Airy's waves for the potential according to Equation 3.8. For Airy's waves, β describes the incoming wave angle, and $\beta = -\pi$ represents head waves. The wave frequency ω is defined by the dispersion relation in Equation 3.9.

$$\Phi_0 = -i\frac{g}{\omega}e^{kz}e^{ik(x\cos\beta + y\sin\beta)} \tag{3.8}$$

$$\omega^2 = kg\tanh(kh), \quad \text{for } h \to \infty \Rightarrow \omega^2 = kg \tag{3.9}$$

This only provides information about the incoming wave and not yet anything related to the wetted hull. For that, a Green function will be applied as it has some beneficial properties.

3.1.3. Green Function

A Green function $G(\vec{x}, \vec{\xi}, f, \epsilon)$ can be applied to find the source strength. The exact Green function and the numerical details will not be discussed in this thesis. Noblesse [17] goes into great detail on the function and how to resolve numerical problems. Equations 3.10, 3.11 and 3.12 describe the properties of the Green function. The term $\vec{x}$ relates to the field point, while $\vec{\xi}$ represents the position of the singular point, which is either a source or a sink. δ is a Dirac delta function. The Laplacian of the Green function is dependent on the distance between the field point and the singular point (Equation 3.10). One significant result of this property is that all sources and sinks affect the flow. Every panel on the hull has a source or sink. The computational cost then scales by a factor of n^2.

$$\vec{\nabla}^2 G = \delta(x-\xi)\delta(y-\eta)\delta(z-\zeta) \quad \text{in} \quad z < 0 \tag{3.10}$$

The second property in Equation 3.11 relates to the free surface. The result is that no panels are required to evaluate the free surface. This is highly beneficial, as it significantly reduces the required panels. The application of the Green function for sources in a BEM enables rapid evaluation, especially since it is resolved in the frequency domain. All panels fluctuate with a frequency f and have an individual phase ϵ. Finding and balancing all the strengths and phases of the sources and sinks with the Green function is a numerically intensive process, but no further transient iteration is required.

$$G_z - f(1+i\epsilon)^2 G = 0 \quad \text{on} \quad z = 0 \tag{3.11}$$

The last property of the Green function is that the influence of the sources reduces to zero as the distance of the panels approaches infinity. This requirement implies that the integral over the far-field boundary is zero. No further discretisation and meshing over the water depth is then required.

$$G = \mathcal{O}(1/r) \quad \text{as} \quad r = |\vec{x} - \vec{\xi}| \to \infty \tag{3.12}$$

All these properties combined result in a mesh of only the wetted hull that can describe the response to incoming waves. Capytaine solves the potential formulation in Equation 3.13 to find the source distribution $\sigma(\xi)$ where it sums over the entire wetted surface S with the discretised panels s.

$$\Phi(\vec{x}, f) = \iint_S \sigma(\xi) G(\vec{x}, \vec{\xi}, f, \epsilon) ds(\xi) \tag{3.13}$$

The additional assumptions in applying a Green function to obtain source strengths are then:

- No disturbances far away from the ship.
- The pressure at the free surface is constant $p = p_{atm}$.
- Kinematic boundary condition, particles at the free surface stay there.
- Calculation cost scales with the number of panels squared due to the interdependent source strengths.

3.2. Hydromechanical Mesh

As mentioned in Section 3.1.3, Capytaine only requires panels on the hull. It only considers potentials on the static submerged hull and not the actual instantaneous water position. The result is that only panels have to be meshed for z =[-T,0]. Capytaine is then used to solve the diffraction and the radiation problem on the mesh. A phenomenon that can occur is the formation of standing waves in the fluid within the hull at specific wave frequencies. This is a result of the calculation method. Capytaine treats the problem as if there is fluid inside the hull. Only the normal velocity on the wetted hull panels is matched, assuring no fluid transfer through the hull. Capytaine doesn't differentiate between fluid outside or inside the hull. The behaviour at irregular frequencies can be removed by adding a second mesh. This mesh covers the surface area within the hulls and counteracts the non-physical fluid behaviour at irregular frequencies. Both the hull and lid mesh were made in Rhino7 with an additional step to create a quadrilateral mesh for consistent mesh sizes, although elements near the plane cutting the waterline could also result in being triangular.

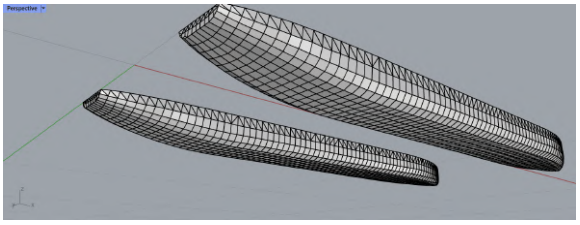

(a) Coarse hydromechanical mesh consisting of 1863 panels.

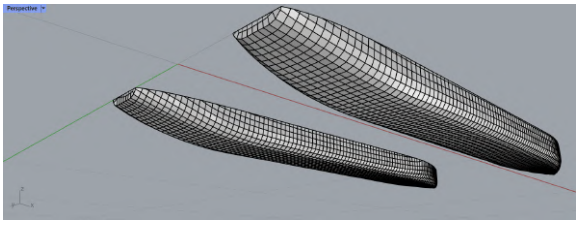

(b) Fine hydromechanical mesh consisting of 7110 panels.

Figure 3.1: Coarse and fine hydromechanical mesh

3.2.1. Hydromechanical Mesh Convergence

To investigate whether the mesh is of sufficient quality, a mesh refinement study is done. Four levels of mesh refinements were used in the study, consisting of 1863, 2843, 4248, and 7110 panels. The RAOs of translation and rotation are displayed in Figures 3.2 and 3.3, respectively. The general behaviour of all graphs is about as expected. The head waves only excite a surge, heave and pitch response. The surge and heave amplitudes start at an RAO of about one at a low frequency. Thus, the vessel's motion approaches the wave's orbital movement for long waves. Consequently, the pitch RAO is close to zero as the waves are so long that almost no pitch behaviour is excited. The pitch RAO approaches a peak at a wave frequency of 6.5 rad/s, corresponding to a wavelength $\lambda \approx 3/2L$. The waves are slightly longer than the ship and result in the most significant pitching motions.

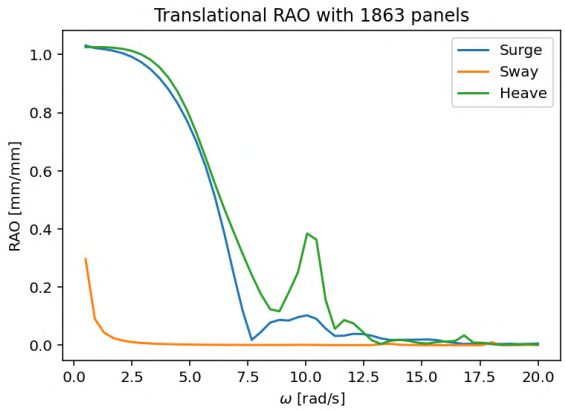

(a) Translational RAOs for submerged hydro mesh of 1863 panels

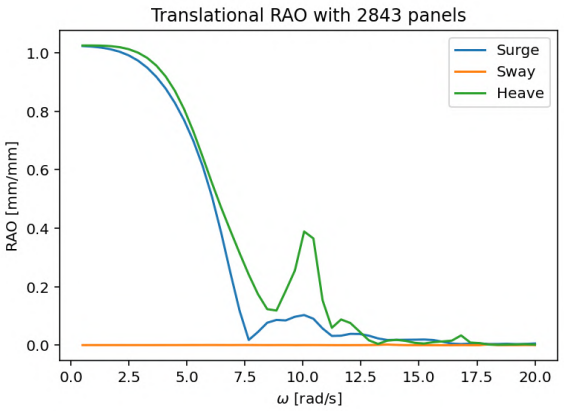

(b) Translational RAOs for submerged hydro mesh of 2843 panels

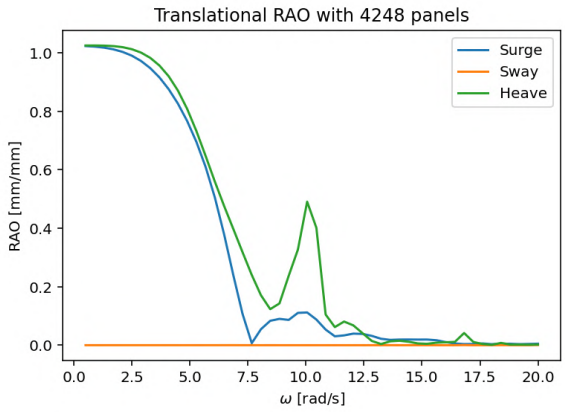

(c) Translational RAOs for submerged hydro mesh of 4248 panels

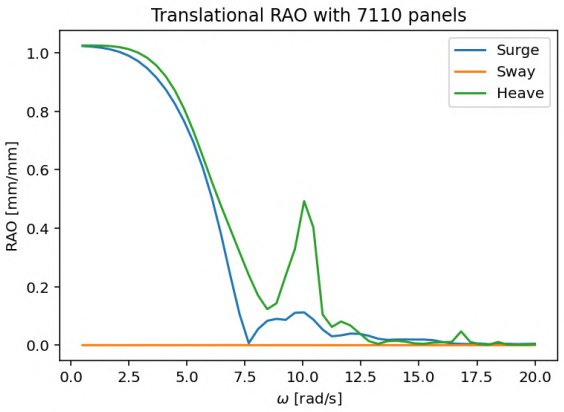

(d) Translational RAOs for submerged hydro mesh of 7110 panels

Figure 3.2: Mesh convergence of translational RAOs

Beyond the peak in pitch RAO, the wavelength is equal to the ship at about 7.5 rad/s. As the surge excitation approaches zero, the heave RAO reduces, but it does not approach zero. The reason this does not occur for heave is that the hull is not symmetrical about the yz-plane. The heave has a smaller peak at approximately 10 rad/s and a wavelength of $\lambda \approx 2/3L$. The wavelength at this frequency is such that the widest part of the vessel can be at a peak or trough. There is a logical reason why the response is much smaller than the wave. Inertial effects start to dominate as the frequency increases. The wave forces are applied so briefly that, due to inertia, the vessel no longer responds to them. That is also why, for even larger wave frequencies, all RAO amplitudes approach zero.

Some peculiarities can be pointed out in the mesh convergence. What can be seen in Figures 3.2a and 3.3a is that in the coarse mesh of 1863 panels, there was a non-zero sway and yaw value at low wave frequencies. It appears that as a result of the meshing step, the 1863 panel mesh was no longer fully symmetrical. Figures 3.2c and 3.2d show that the peak of heave around a wave frequency of 10 rad/s becomes more pronounced for both the 4248 and 7110 panel meshes.

Regarding the rotational RAOs, it can be observed that in the coarse meshes (Figures 3.3a and 3.3b), there are some unexpected small peaks in pitch behaviour at frequencies over 15 rad/s. The rotational RAOs of the two more refined meshes displayed in Figures 3.3c and 3.3d show a more distinct peak of the pitch RAO at both 9 and 11 rad/s. Differences between the 4248 and 7110 panel meshes are minor. Hence, it is concluded that for the finest mesh, the RAO has converged. The computation cost for these two meshes was still relatively low; in subsequent analysis, the mesh of 7110 panels is utilised. If even more frequencies or many geometries need to be calculated, it would be more efficient to use the coarser mesh of 4248 panels.

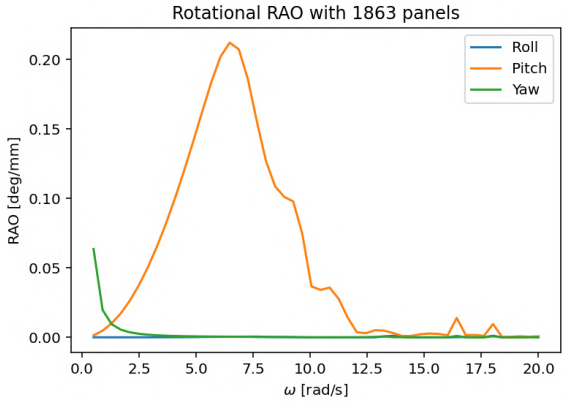

(a) Rotational RAOs for submerged hydro mesh of 1863 panels

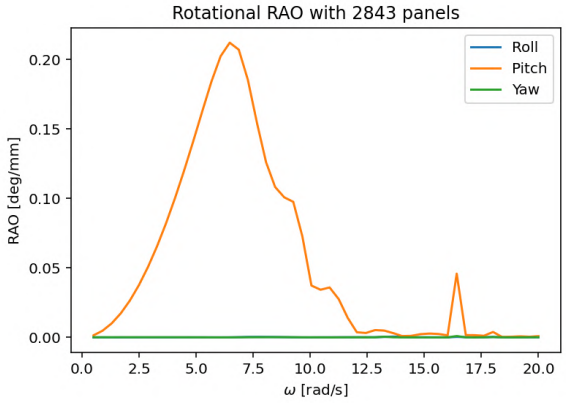

(b) Rotational RAOs for submerged hydro mesh of 2843 panels

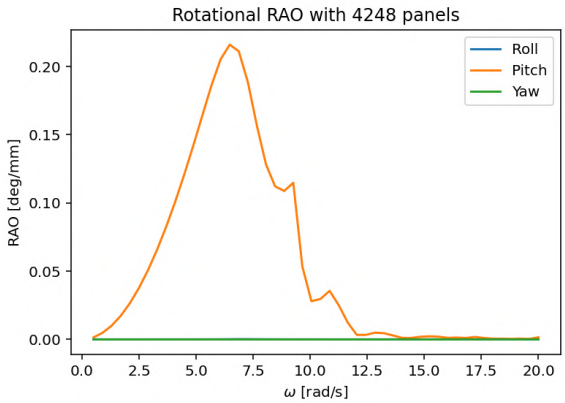

(c) Rotational RAOs for submerged hydro mesh of 4248 panels

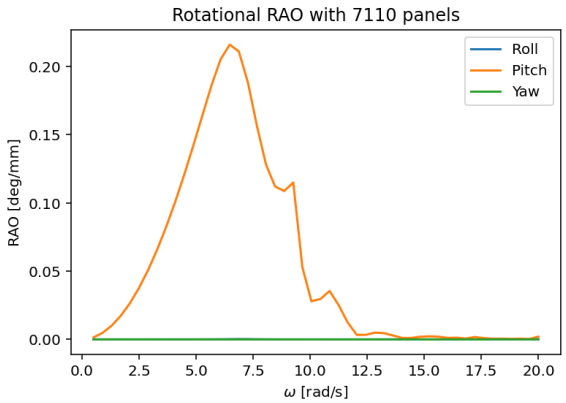

(d) Rotational RAOs for submerged hydro mesh of 7110 panels

Figure 3.3: Mesh convergence of rotational RAOs

3.3. Motion Response

The finest mesh was again evaluated, now for steps in frequency of 0.05 rad/s. The results at the increased frequency resolution are shown in Figure 3.4. Vertical lines are plotted at frequencies of interest ω_i, which are chosen for several reasons. Immersion of the wetdeck is expected as a result of large pitch and or heave amplitude with unfavourable phasing compared to the wave. When checked for various frequencies, three cases appeared to be of interest. The first investigated wave frequency $\omega_{i,1}$ is at 6.5 rad/s. The pitch RAO was at its peak and slightly out of phase compared to low wave frequencies, where the ship exactly follows the wave. The second case at a wave frequency $\omega_{i,2}$ of 9.5 rad/s still exhibits a relatively large pitch RAO. Additionally, there is a Heave RAO that is significantly out of phase. The last case considered, $\omega_{i,3}$ of 10.1 rad/s, has a smaller but lagging pitch RAO. What makes this case worthwhile to investigate is the significant amplitude of the out-of-phase heave RAO. The motions of these three cases will be further investigated for the slamming behaviour.

Phasing of RAOs

A phase lag between the heave and the wave corresponds to the vessel's movement compared to the wave at the origin. At low frequencies, the phase difference is close to 0 radians. The waves are longer than the vessel, and it moves quasi-statically with the wave surface. A phase difference close to plus or minus π is then interesting. The peak amplitudes occur at the same time but in opposite directions, reducing the distance between the wave surface and the wet deck. On the pitch phase, it can be commented that it is initially $\epsilon_{pitch} \approx \pi/2$ where again it follows the long waves. The most significant pitch amplitude is obtained for a leading phase $\epsilon_{pitch} > \pi/2$, with a leading phase, the bow pitches down earlier compared to the wave. Which makes forward slamming more likely. A lagging phase $\epsilon_{pitch} < \pi/2$ results in a closer distance between the surface and the wet deck aft, making it more likely to cause an impact there.

Table 3.1: RAOs and phases of various wave frequencies

ω [rad/s]	RAO_{heave} [mm/mm]	$\epsilon_{heave}[rad]$	RAO_{pitch} [deg/mm]	$\epsilon_{pitch}[rad]$
2.5	1.013	0.001	0.037	1.59
5	0.781	-0.014	0.151	1.677
6.5	**0.489**	**-0.194**	**0.215**	**1.905**
7.5	0.254	-0.580	0.162	2.157
9.5	**0.257**	**-2.541**	**0.118**	**2.004**
10.1	**0.499**	**-2.091**	**0.026**	**1.486**
12.5	0.035	2.882	0.004	-2.026
15	0.004	-1.985	0.002	1.032
17.5	0.019	-1.358	0.003	0.066
20	0.003	-0.527	0.002	-1.112

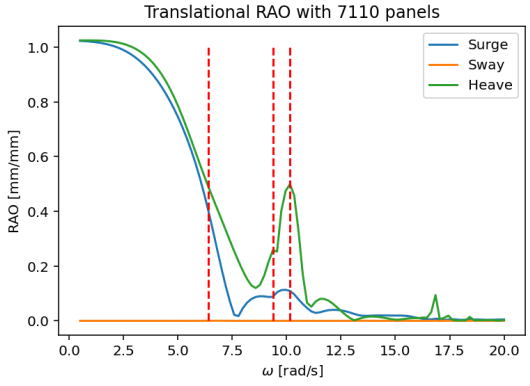

(a) High resolution translational RAOs with 7110 panel hydro mesh

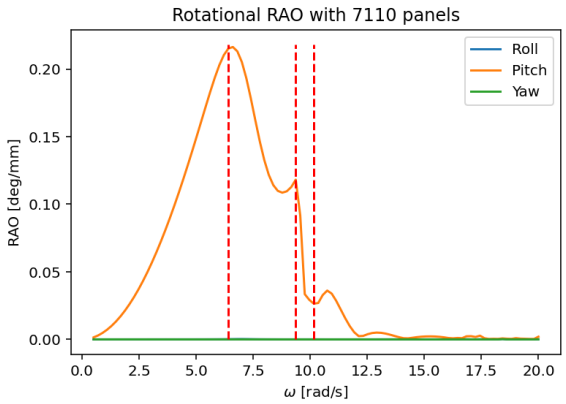

(b) High resolution rotational RAOs with 7110 panel hydro mesh

Figure 3.4: RAOs for 200 wave frequencies, the red dashed lines indicate cases which will be further investigated for immersion

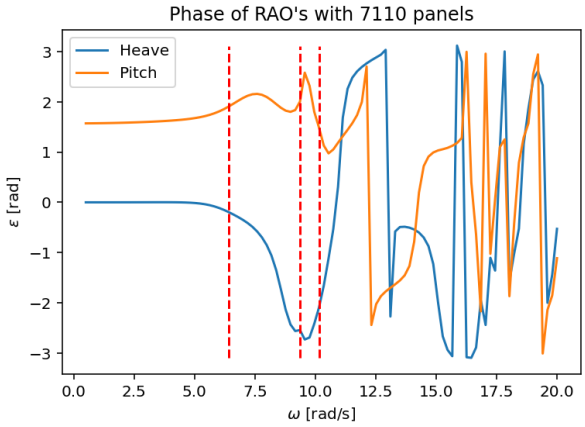

Figure 3.5: High resolution phase of heave and pitch RAO with 7110 hydro panel mesh, the red dashed lines indicate cases which will be further investigated for immersion

3.4. Slamming Force on the Wet Deck

The motion analysis based on the RAO only considers the mean submerged hull. There are then no interactions between the water and the wet deck calculated in the motion analysis, since no part of the cross deck is submerged in the water at design draught. To determine the forces resulting from contact, a different calculation method should be applied.

Wagner [18] developed an impact theory based on potential flow theory. Represented by Equation 3.15, the pressures approach infinity at the point of wetting. The Wagner slam pressure is a result of the Bernoulli pressure formulation with the potential described by Equation 3.14. The asymptotic behaviour presents difficulty in obtaining analytical maximum slam pressures to compare to experimental measurements. The exact peak pressures are somewhat less of a concern in this thesis, as the structural response is the primary focus. This results in an emphasis on the transfer of momentum from water to the structure. With sufficiently small time steps, the asymptotic behaviour near the wetted length c should converge. To check whether convergence occurred, the sum of the force multiplied by the time step approaches a constant value for an increasing number of time steps.

$$\varphi(t,x) = -V \cdot \sqrt{c(t)^2 - x^2} \tag{3.14}$$

$$p(t,x) = \rho V \frac{c(t)}{\sqrt{c(t)^2 - x^2}} \frac{dc}{dt} \quad \text{for } x < c(t) \tag{3.15}$$

The underlying theory in this method originates from a wedge impact into water. It should be investigated whether such a wedge slamming could approximate the slamming behaviour of the wet deck. For this, the water should be flat or at least the relative angle between the deck and the water surface should remain constant. It is almost certain that this will not be the case. However, instead of a wedge entry problem, the wet deck slamming could be more accurately described by a plate wave impact case. In such a case, a wave at constant velocity impacts a flat plate. This requires an accurate description of the wetted length c over time. The immersion of the wet deck can be investigated through the rigid body motions resulting from waves. Subsequently, pressures can be derived from immersion events.

There are only two implications when utilising this method to evaluate slamming pressures:

- The immersion event should be of short duration, so that the vessel's pitch remains almost constant.
- The impulse of the slamming impact should be small compared to the wave loading of the hull; otherwise, the motion analysis is no longer accurate.

4. Wet Modal Analysis

An essential part of structural analysis on a ship is the water effects. The modal analysis described in Section 2.2 was performed for the hull in a vacuum. To include the water effects, Capytaine is again utilised. Capytaine solves the diffraction and radiation problem of the hydromechanical mesh for a given degree of freedom (DOF). One nice feature is that the various flexible modes can be specified as DOFs. Along the flexible DOFs, the hydromechanical diffraction and radiation problem is solved. In this chapter, the specifics of the wet modal analysis will be discussed.

4.1. Mapping Dry Modes to Hydromechanical Mesh

There are different requirements for the structural mesh (Section 2.1) and the hydromechanical mesh (Section 3.2). For the modal analysis in ANSYS, a fine mesh is required to obtain sufficiently converged modal results. The same resolution mesh is very undesirable for Capytaine. As in a BEM solver with Green's sources, the computational cost scales n_{panels}^2. The computational cost is even more problematic for Capytaine compared to commercial BEM solvers. The method it employs to solve the matrices required for computation comes at a significant cost in Random Access Memory (RAM). To give an impression, the fine mesh of 7110 panels used in Chapter 3 utilised about 10GB of RAM.

Method 1: Vertical Bending and Roll

To incorporate flexible modes from ANSYS in the degrees of freedom, a mapping step was required. Then the flexible deformations can be applied in Capytaine. The first method of mapping the modal deformations involved determining the average rotation about the longitudinal axis and vertical displacements of numerous cross-sections over the length. The averaging was conducted separately for each demi-hull. It was expected that this model would sufficiently capture the flexible mode shapes (depicted in Figure 2.3) while also ensuring a smooth transition in displacements. The resulting mapped displacements of the first two modes are displayed in Figures 4.1 and 4.2. What can be seen is that the fit of the vertical displacements and cross-sections is well fitted to the average. The ANSYS values do not fully extend to 0 and 1.1 m as they are positioned with a centre point and a small range in both directions. Thus, the average of the first cross-section is taken for a longitudinal slice with a tolerance. The first cross-section was for x between 0.045 m and 0.055 m. The process is repeated over the length in steps of 0.05 m. It can be expected that panel centres and nodes are located till both longitudinal ends, but at these ends fewer elements are averaged. The fit is extrapolated fully on the domain of 0 to 1.1 meters. The mapped displacements appear to be okay at first glance. However, when the mapped displacements were compared to the ANSYS displacements, they appeared to be lower. From the z displacements in the deck and bottom in Figure 4.3. It can be seen that in the averaging step, the transversely varying z-displacement results in a single value per cross section. It appeared that the average rotation could not subsequently reintroduce the locally varying displacements. In Figure 4.4, the roll rotation is based on y displacements in the deck and bottom and z displacements in the side shell. The lack of uniform rotation for all panels of the hull led to a new approach. The magnitude of the roll angle seems ridiculously large. However, this is a result of scaling the displacements to the unit vectors. The rotations would never be realistically achieved. Since the scaling is applied consistently, this would have no further impact on the analysis.

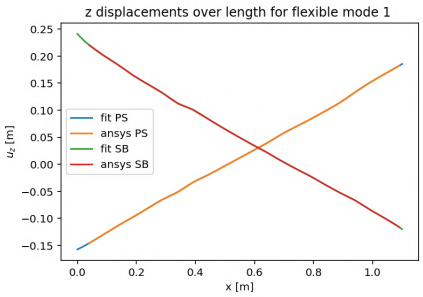

(a) Average z displacements mapped for 1st flexible mode

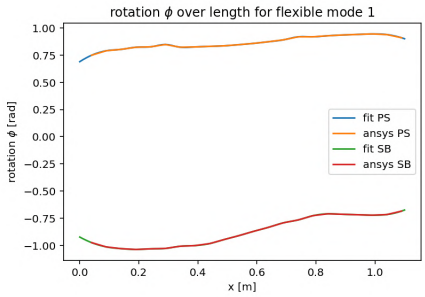

(b) Average roll rotation ϕ mapped for 1st flexible mode

Figure 4.1: Interpolation and extrapolation of 1st dry mode

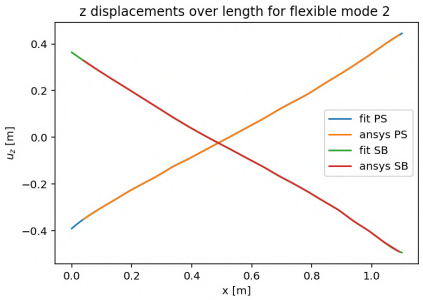

(a) Average z displacements mapped for 2nd flexible mode

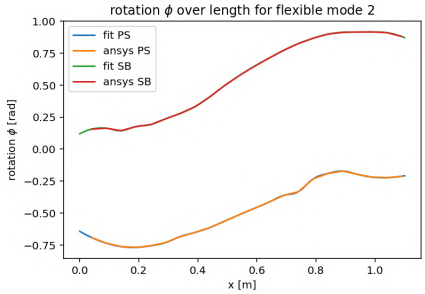

(b) Average roll rotation ϕ mapped for 2nd flexible mode

Figure 4.2: Interpolation and extrapolation of 2nd dry mode

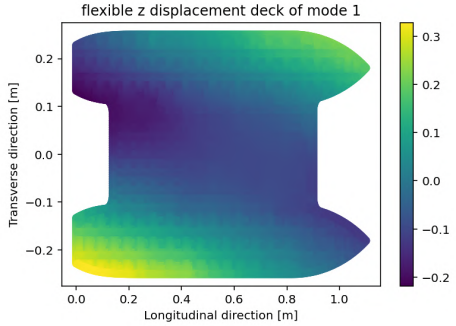

(a) Z displacements plotted on the deck

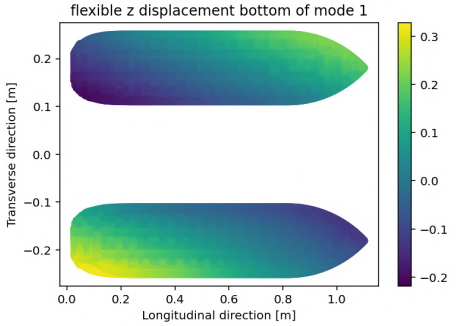

(b) Z displacements plotted on the bottom

Figure 4.3: Z displacements in the deck and bottom

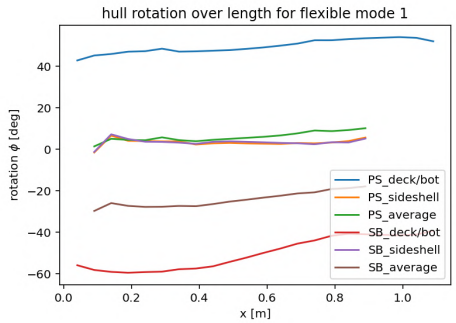

Figure 4.4: Roll rotations based on various parts of the shell plating

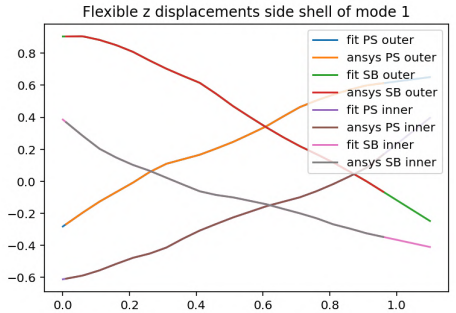

Figure 4.5: Z displacements of the side shell for the first flexible mode using the second method

Method 2: Positional Displacements of Compartments

Since the first method was not able to accurately map the dry mode shape, a second method is proposed. Per cross-section, each demi-hull is divided into four compartments, shown in Figure 4.6. The displacements of the sides, top, and bottom are averaged in the x, y and z directions. The more localised averaging allows for the inclusion of more accurate local behaviour. One downside is that the displacement behaviour is not continuous across the edges separating the compartments, as pointed out by the red arrows in Figure 4.7. This would introduce a minor error, but local flexible behaviour that closely approximates the dry modes of ANSYS is more critical. Further possibilities to improve the mapping to the hydromechanical mesh will also be discussed in Chapter 9. Additionally, the shape shown in Figure 4.7 is quite exaggerated compared to the expected excitation. It is not expected that, as a result of a slamming event, the structure will vibrate with displacements approaching 1/10 of the length.

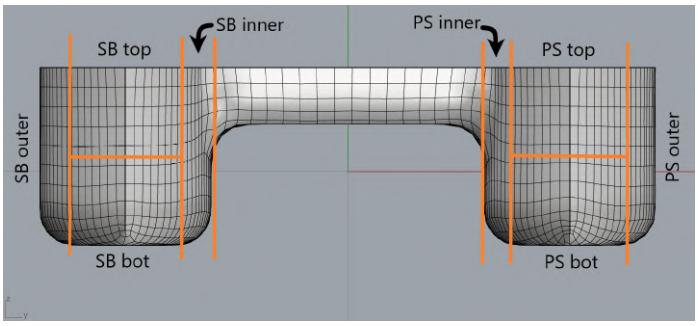

Figure 4.6: Front view showing the four compartments of each demi hull over which displacements are averaged.

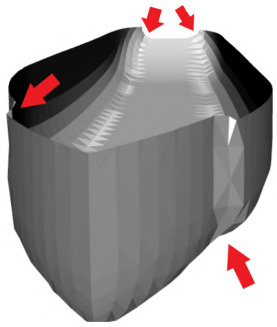

Figure 4.7: Exaggerated Modal displacements mapped to hydromechanical mesh.

4.2. Wet Modal Analysis

With the flexible mode shapes mapped to the hydromechanical mesh, Capytaine is again utilised to solve the diffraction and radiation problem. However, the four flexible modes are now considered as additional degrees of freedom. One crucial factor in a wet modal analysis is to run the BEM solver at the frequency of the mode shapes, as the hydromechanical behaviour in response to excited mode shapes can be obtained. The Wet modal analysis should therefore include an iteration, as the hydromechanical behaviour changes slightly between the dry and wet natural frequencies. To obtain the wet natural frequencies, the eigenvalue problem in Equation 4.1 is solved. The modal mass is an input from ANSYS; the modal stiffness can then be calculated with Equation 4.2.

$$([M_m] + [A(\omega)])\ddot{\vec{u}} + ([K_m] + [C(\omega)])\vec{u} = \vec{0} \tag{4.1}$$

$$[K_m] = \vec{\omega}^2_{dry}[M_m] \tag{4.2}$$

4.2.1. Scaling of ANSYS Results

For the modal analysis, the scaling between the rigid and flexible modes should be the same to enable comparison of the order of partial results. Capytaine uses a unit vector for the greatest displacement vector, as per Equation 4.3. This means the vectors are 1 in the corresponding axis for each rigid body translation. For rotations, the vectors are scaled such that the largest displacement vector becomes one. The flexible modes from ANSYS should then be scaled by a factor $\lambda_{modeshape}$ such that the magnitude of the largest displacement vector is also 1. The scaling step also affects the modal mass, which scales with the $\lambda^2_{modeshape}$. The resulting stiffness is not directly scaled, but it is recalculated using the new scaling, as shown in Equation 4.2. For the modal stiffness $[K_M]$, the dry frequencies are utilised.

$$max(|\vec{u}|) = max(\sqrt{u_x^2 + u_y^2 + u_z^2}) = 1 \tag{4.3}$$

4.2.2. Panel Length and Wave Frequencies

One thing to note is that in a BEM analysis, the length of a panel should be up to one-eighth of the wavelength to ensure stability. This criterion is problematic for the BEM analysis at the high frequencies associated with the wet modes. To keep the fourth mode shape within the requirement, the element should be smaller than $l_{max} < \lambda_\zeta/8 = \frac{2\pi}{8\omega_{d,4}^2/g} \Rightarrow l_{max} < 0.0001m$. The required elements to obtain such a fine mesh are on the order of 3 to 7 million. Considering the computing cost scales with n_{panels}^2, the required mesh size is not feasible to execute. As a result of not adhering to the criteria on the panel length, the convergence process was not monotonic, although over iterations, the wet frequency did converge. The higher frequencies that do not adhere to the criteria are not utilised in further analysis.

4.2.3. Convergence of Wet Modes

For each dry frequency, the code was run and subsequently iterated until the wet frequency was within 1% of the average value of the last five iterations. To more accurately model the added mass and stiffness of the mode shapes, the code is run at the wet frequencies $\omega_{w,i}$. New wet mode shapes are calculated and matrices $[A]$, $[C]$ for added mass and stiffness are obtained. This process is iterated until the wet frequencies converge. The convergence of the wet frequencies is non-monotonic. The convergence criterion utilised is based on the average wet natural frequency of the last few iterations. Convergence is achieved if the last iteration's $\omega_{w,i}$ is within 1% of the average $\omega_{w,i}$ of the last five iterations. To investigate the uncertainty added from the larger panels, a convergence study was done for various mesh sizes, shown in Figure 4.8. There were some differences, but the converged wet natural frequencies were overall quite similar. Showing a difference of only a couple of percentage points when compared to the results of the finest mesh investigated. The converged frequencies of the finest mesh are listed in Table 4.1.

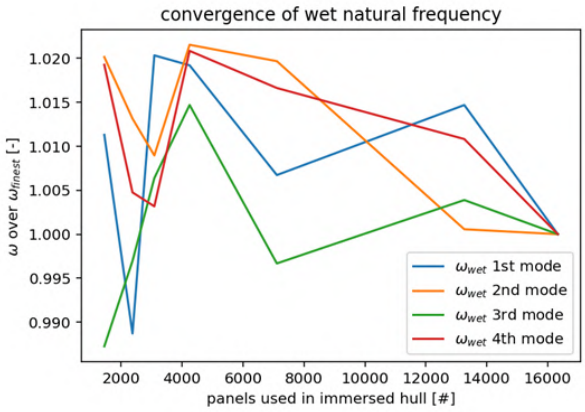

Figure 4.8: Ratio of Wet natural frequencies to the finest wet natural frequency calculated

Mode	Dry natural frequency f_d [Hz]	Wet natural frequency f_w [Hz]
1	21.65	17.72
2	23.69	21.47
3	39.86	36.11
4	44.14	37.93

Table 4.1: Converged wet natural frequencies

4.3. Wet Modal Properties

The result of the wet modal analysis is then a total Modal mass matrix and the wet natural frequencies. The total stiffness, including the added stiffness from the water, can then easily be extracted with Equation 4.2. The eigenfrequencies of the eigenmodes are listed in Table 4.1. The frequencies of the rigid body motions should all approach zero. The dry structural modal mass [M] and total modal mass [M+A] are listed below. The modal masses in the matrix could not be calculated simultaneously for every wet

modal frequency. Thus, it was chosen to take the greatest frequency for which the panel length was within the desired length prescribed in Section 4.2.2. The upper limit was approximately 3 Hz or 18.8 rad/s, which is well above the range of the incoming wave frequencies.

$$M = \begin{bmatrix} 15.89 & 0 & 0 & 0 & 0 & 0 & 0 & 0 & 0 & 0 \\ 0 & 15.89 & 0 & 0 & 0 & 0 & 0 & 0 & 0 & 0 \\ 0 & 0 & 15.89 & 0 & 0 & 0 & 0 & 0 & 0 & 0 \\ 0 & 0 & 0 & 0.9045 & 0 & 0 & 0 & 0 & 0 & 0 \\ 0 & 0 & 0 & 0 & 6.278 & 0 & 0 & 0 & 0 & 0 \\ 0 & 0 & 0 & 0 & 0 & 6.1389 & 0 & 0 & 0 & 0 \\ 0 & 0 & 0 & 0 & 0 & 0 & 7.904 & 0 & 0 & 0 \\ 0 & 0 & 0 & 0 & 0 & 0 & 0 & 3.800 & 0 & 0 \\ 0 & 0 & 0 & 0 & 0 & 0 & 0 & 0 & 4.313 & 0 \\ 0 & 0 & 0 & 0 & 0 & 0 & 0 & 0 & 0 & 2.587 \end{bmatrix}$$

$$[M+A] = \begin{bmatrix} 16.12 & 7.92e\text{-}5 & 0.40 & -1.00e\text{-}5 & 0.30 & -1.14e\text{-}7 & -0.02 & -6.53e\text{-}3 & 0.01 & 0.03 \\ 5.30e\text{-}5 & 20.49 & 1.81e\text{-}3 & 0.33 & 1.02e\text{-}4 & 0.20 & -0.24 & -0.17 & 0.47 & -0.25 \\ 0.40 & 1.75e\text{-}3 & 34.19 & 9.37e\text{-}5 & 0.41 & -2.90e\text{-}5 & -1.44 & 0.25 & -0.04 & -0.95 \\ 9.11e\text{-}6 & 0.33 & 5.34e\text{-}5 & 1.465 & 1.80e\text{-}5 & 1.14\text{-}2 & 0.20 & 0.05 & -0.25 & 0.50 \\ 0.30 & -9.92e\text{-}6 & 0.41 & 1.05e\text{-}5 & 7.408 & -3.09e\text{-}5 & -0.01 & -0.02 & -0.07 & -0.07 \\ -2.00e\text{-}5 & 0.20 & -1.10e\text{-}4 & 0.01 & -3.97e\text{-}5 & 6.509 & 8.78e\text{-}3 & -0.07 & 0.03 & -0.08 \\ -0.02 & -0.24 & -1.44 & 0.20 & -0.01 & 8.43e\text{-}3 & 9.574 & -1.61 & -0.13 & 2.25e\text{-}3 \\ -0.01 & -0.17 & 0.25 & 0.05 & -0.02 & -0.07 & -1.61 & 5.93 & -0.10 & 0.40 \\ 0.01 & 0.47 & -0.04 & -0.25 & -0.07 & 0.03 & -0.13 & -0.10 & 4.833 & 0.08 \\ 0.03 & -0.25 & -0.95 & 0.50 & -0.07 & -0.08 & 2.60e\text{-}3 & 0.40 & 0.08 & 3.837 \end{bmatrix}$$

Now, all wet structural properties are obtained. Almost all parts of the modal motion equation (Equation 2.6) are known. The last part required to investigate the excitation of mode shapes is the modal force (Equation 2.7). The modal force is obtained by multiplying the force at the nodes by the local displacement for each mode. One thing to note is that the wet mode shapes are not computed for the entire structure. Therefore, the modal force is calculated with dry mode shapes on the structural mesh. Due to the averaging step in mapping displacements to the hydromechanical mesh, some local information is lost. Therefore, the structural mesh and modal displacements are utilised, as the local excitation of modes is then best included.

5. Response to Monochromatic Waves

Haugen [13] and Davis et al. [14] found potentially impactful parameters for slamming. Equations for relative height (5.1), relative velocity (5.3) and relative angle (5.4) are used to investigate the parameters initially. For these equations, subscripts H, P and w relate to the motions resulting from respectively Heave, pitch and the wave surface. z_{AG} is the air gap distance between the evaluated point and the waterline calculated with Equation 5.2. The RAO is used for the amplitude of the motion, and ϵ for the phase. u is a reference to undisturbed waves taken into account. An undisturbed wave should be alright in representing wet deck immersion near the front of the cross deck. However, this is not a good representation near the aft, as the incoming wave is disturbed there due to interactions with the hull. Before calculating forces, the effect of the disturbed wave is taken into account. One note on the positional argument x_{COG} with its origin in COG and x_O with the origin located at most aft middle part of the vessel. These are the same when the hydro mesh is transposed so that x_{COG} is located at x_O. At this point, the calculation does not account for the forward speed resulting from actual motion. However, it approximates the behaviour by increasing the wave frequency to the corresponding wave encounter frequency, which excludes some of the advection effect in the flow. For a slow sailing vessel, these are likely to be limited. Forward speed will be further discussed in Chapter 9.

$$z_{rel,u}(x,t) = z_H(t) + z_P(x,t) - z_{w,u}(x,t) + z_{AG}(x,y) = \zeta_a \cdot RAO_H \cdot sin(\epsilon_H - \omega t) + tan(\zeta_a \cdot RAO_P) \cdot x_{COG} \cdot sin(\epsilon_P - \omega t) - \zeta_a \cdot sin(kx_O - \omega t) + z_{AG}(x,y) \quad (5.1)$$

$$z_{AG}(x,y) = z(x,y) - T \quad (5.2)$$

$$w_{rel,u}(x,t) = \dot{z}_{rel,u}(x,t) = \dot{z}_H(t) + \dot{z}_P(x,t) - \dot{z}_{w,u}(x,t) = -\zeta_a \cdot RAO_H \cdot \omega \cdot cos(\epsilon_H - \omega t) - tan(\zeta_a * RAO_P) \cdot x_{COG} \cdot \omega \cdot cos(\epsilon_P - \omega t) - \zeta_a \cdot \omega \cdot cos(kx_O - \omega t) \quad (5.3)$$

$$\theta_{rel,u}(x,t) = \theta_P(t) + \theta_{w,u}(x,t) = \zeta_a \cdot RAO_P \cdot sin(\epsilon_P - \omega t) - arctan(\zeta_a \cdot k \cdot cos(kx_O - \omega t)) \quad (5.4)$$

5.1. Verification of Immersion

Table 5.1: Coordinates of the points investigated, the origin is located at the aft centre at the height of the keel.

ID	x [m]	x_{COG} [m]	y [m]	z [m]
1	0.824	0.280	0	0.098
2	0.872	0.328	0	0.098
3	0.892	0.348	0	0.106
4	0.900	0.356	0	0.126
6	0.820	0.276	-0.111	0.071
7	0.870	0.326	-0.111	0.071
11	0.278	-0.266	0	0.098
12	0.221	-0.323	0	0.098
13	0.167	-0.377	0	0.098
14	0.147	-0.397	0	0.106
15	0.139	-0.405	0	0.126
21	0.278	-0.266	-0.111	0.071
22	0.223	-0.321	-0.111	0.071
23	0.167	-0.377	-0.111	0.071

In table 5.1, the considered points along the hull are displayed where the values for x have the aft as the origin. The points that only have a different y-value are, for now, ignored. The transverse position can be ignored since the undisturbed formulation of relative positional arguments has no y-dependency.

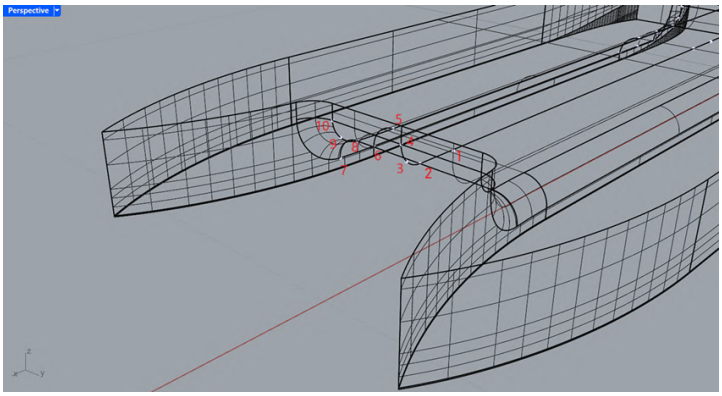

(a) Points near bow of cross deck which were initially investigated for immersion

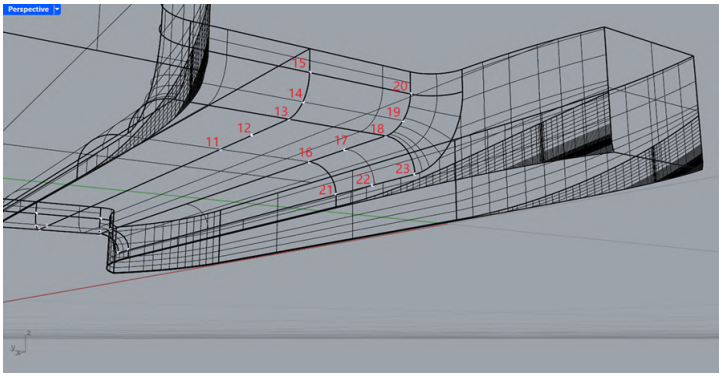

(b) Points near aft of cross deck which were initially investigated for immersion

Figure 5.1: Points evaluated for verification of initial immersion

As shown in Figure 5.2, various points become immersed at the frequencies of interest indicated in chapter 3.3. ζ_a was taken as 30 mm corresponding to $\zeta_{a,FS}$ of 5.4 m. The air gap height is included in the relative distance z_{rel}. Thus, when the relative distance becomes negative, the panels will be immersed in the water.

The colours are based on the different Z positions compared to the waterline. Purple is the height of the bottom of the radius connecting the cross-deck. Blue is the air gap height equal to the distance from the waterline to the wet deck. Green is located midway along the radius from the wet deck to the vertical plating, and red is at the top.

These points were chosen to investigate the immersion behaviour. If green and especially red experienced significant immersion, the slamming problem would also include a substantial longitudinal component as a result of a slam. Since the vessel is not sailing at high speeds, the extent to which the vessel dives into the waves remains limited. However, the pitching motions remain substantial when the wavelength is close to the ship's length. If the phasing between the pitching motions and the wave is unfavourable, immersion of the wet deck does occur (figure 5.2a). The points aft seem to experience more significant submersion, likely a result of the distance to the COG being greater.

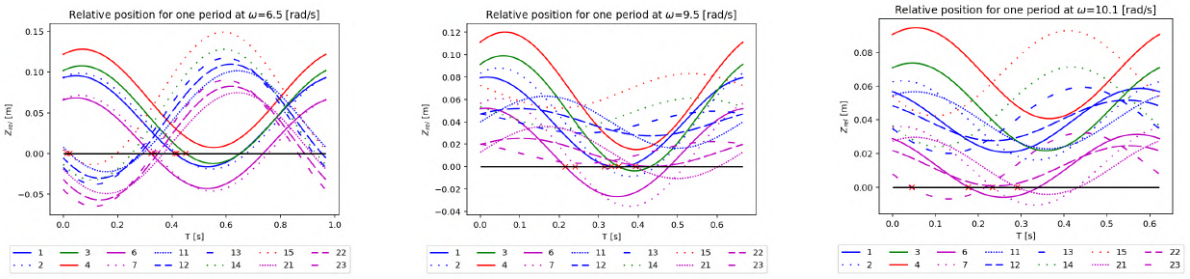

(a) Relative position for ω=6.5 [rad/s] **(b)** Relative position for ω=9.5 [rad/s] **(c)** Relative position for ω=10.1 [rad/s]

Figure 5.2: Relative position between wave and water for frequencies of interest

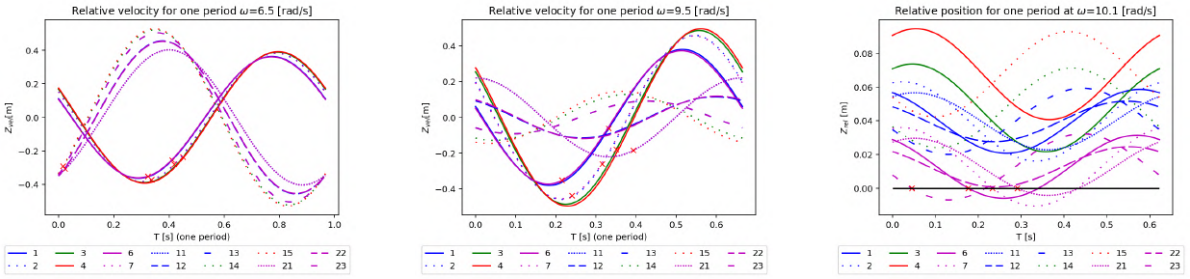

(a) Relative velocity for ω=6.5 [rad/s] **(b)** Relative velocity for ω=9.5 [rad/s] **(c)** Relative velocity for ω=10.1 [rad/s]

Figure 5.3: Relative velocity between wave and water for frequencies of interest

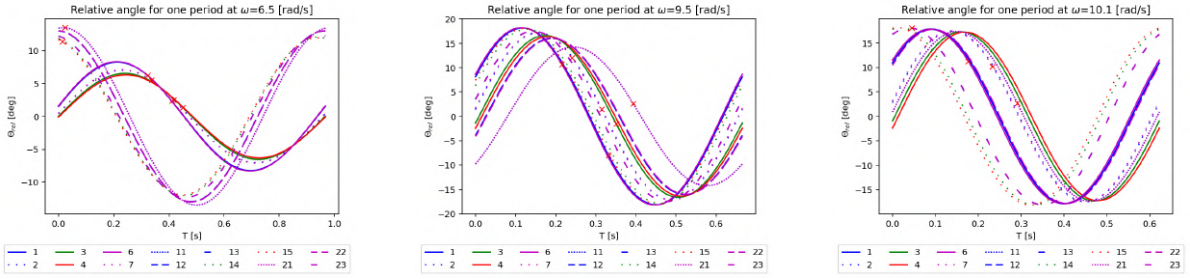

(a) Relative angle θ_{rel} for ω=6.5 [rad/s] **(b)** Relative angle θ_{rel} for ω=9.5 [rad/s] **(c)** Relative angle θ_{rel} for ω=10.1 [rad/s]

Figure 5.4: Relative position between wave and water for frequencies of interest

5.2. Disturbed Wave

To include the interaction between the wave and hull in the positional arguments, the free surface elevation is evaluated over various points in Capytaine. This yields the amplitude and phasing of the wave surface elevation at those points. The result for a wave frequency of 6.5 rad/s is displayed in Figure 5.5. For immersion calculation of the wet deck, the orange box should be further inspected. The orange box represents the entire flat surface between the radiuses that join the cross deck to the hull. Later graphs in this section will depict that area. The reason the connecting radii are ignored is that the wedge impact or plate wave impact theory does not apply to curved surfaces. This will likely affect the resulting forces and should be addressed when validation against experimental values is performed in Chapter 7.

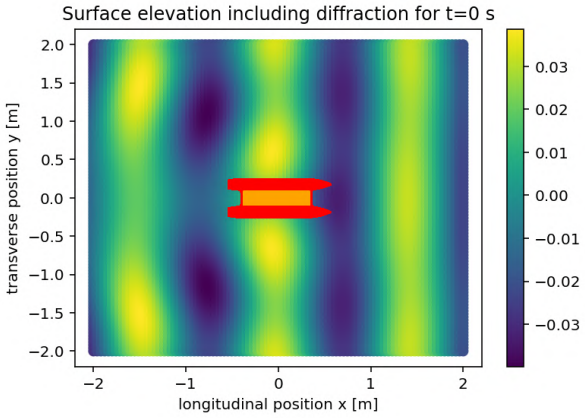

Figure 5.5: Wave surface elevation around Catamaran in monochromatic waves with a frequency ω=6.5 [rad/s]

With knowledge of the undisturbed wave Equations 5.1 and 5.3 can be adjusted so that the wave height and velocity include the diffraction effects. The result is shown in Equations 5.5 and 5.6. The value for the relative angle cannot be obtained as easily. It requires discretisation over the length from where the angle would be slightly different if, due to diffraction, the wave was not travelling purely in the longitudinal direction. The 3D effects will be examined in further slamming analysis in Section 6.1.

$$z_{rel,d}(x,y,t) = z_H(t) + z_P(x,t) - z_{w,d}(x,y,t) + z_{AG}(x,y) = \zeta_a \cdot RAO_H \cdot sin(\epsilon_H - \omega t) + tan(\zeta_a \cdot RAO_P) \cdot x_{COG} \cdot sin(\epsilon_P - \omega t) - \zeta_a \cdot RAO_{w,d}(x,y) \cdot sin(\epsilon_{w,d}(x,y) - \omega t) + z_{AG}(x,y) \quad (5.5)$$

$$w_{rel,d}(x,y,t) = \dot{z}_{rel,d}(x,y,t) = \dot{z}_H(t) + \dot{z}_P(x,t) - \dot{z}_{w,d}(x,y,t) = -\zeta_a \cdot RAO_H \cdot \omega \cdot cos(\epsilon_H - \omega t) - tan(\zeta_a * RAO_P) \cdot x_{COG} \cdot \omega \cdot cos(\epsilon_P - \omega t) + \zeta_a \cdot RAO_{w,d}(x,y) \cdot \omega \cdot cos(\epsilon_{w,d}(x,y) - \omega t) \quad (5.6)$$

The wave surface amplitude ($RAO_\zeta \cdot \zeta_a$) for a ζ_a of 30 millimetres is plotted at various points on the wet deck in Figure 5.6. The phases of the RAOs are plotted in Figure 5.7. For a wave frequency of 6.5 rad/s, the vessel interacts with the wave such that the amplitude of elevation is reduced at the aft. There is a slight increase near the centre as a result of wave interactions with the hull.

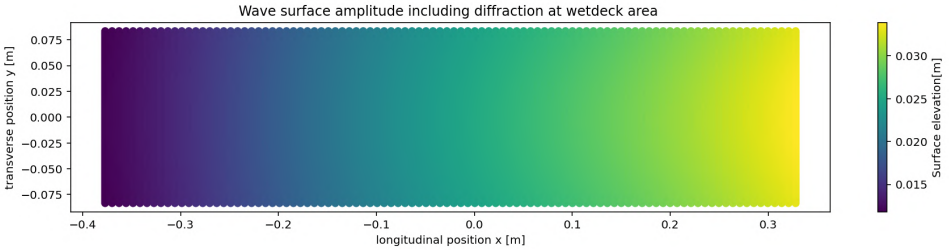

Figure 5.6: Wave surface elevation below the wet deck for $\zeta_a = 30mm$ and $\omega = 6.5rad/s$

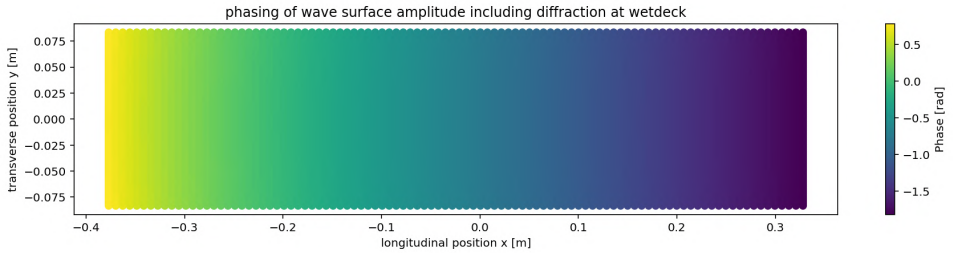

Figure 5.7: Phase of wave surface elevation below the wet deck for $\omega = 6.5 rad/s$

The second frequency of interest was $\omega = 9.5$ rad/s in Figures 5.8 and 5.9, where the wave surface amplitude and phasing of the RAO are plotted. What can be seen is that near the centre, there is a quite prominent peak where waves reach up to 65% higher than the incoming wave. This effect also occurs near the aft of the wet deck, but is limited to an increase of about 45%. Regarding the phasing, it can be seen that almost the complete phase range is now occurring below the wet deck. This is a result of the shorter waves, approximately the length of the wet deck.

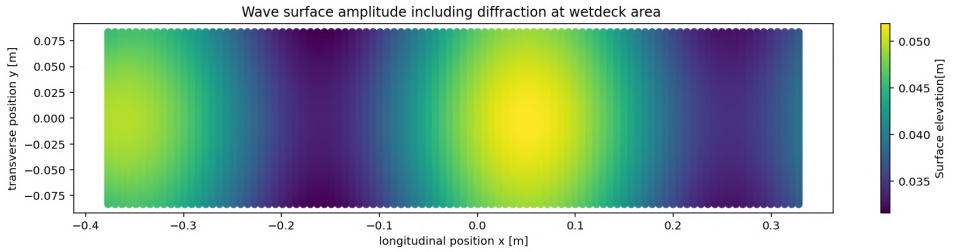

Figure 5.8: Wave surface elevation below the wet deck for $\zeta_a = 30mm$ and $\omega = 9.5 rad/s$

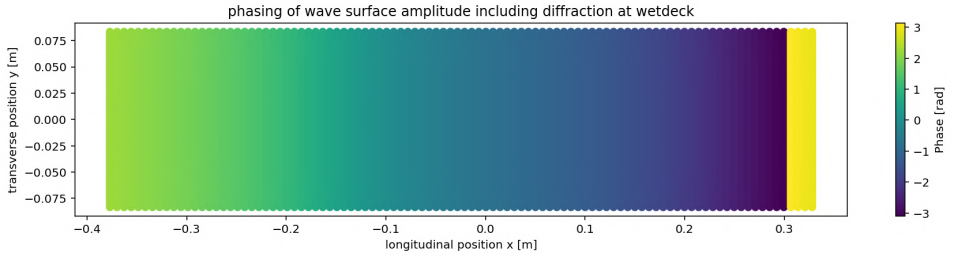

Figure 5.9: Phase of wave surface elevation below the wet deck for $\omega = 9.5 rad/s$

The peaks in RAO are located in three places for an incoming wave frequency of 10.1 rad/s, shown in Figure 5.10. The peaks are slightly less extreme, with a 55% increase compared to an undisturbed wave. Figure 5.11 displays that there is now an overlap in the phasing over the entire wet deck. Showing that the wavelength is now shorter than the wet deck length. The phase shows that both aft and fwd are roughly in the same phase. This seems appropriate for the third case of interest. The main resulting motions are in the heave direction and out of phase. The phasings of the points below the wet deck, shown in Figure 5.11, correspond to such movement.

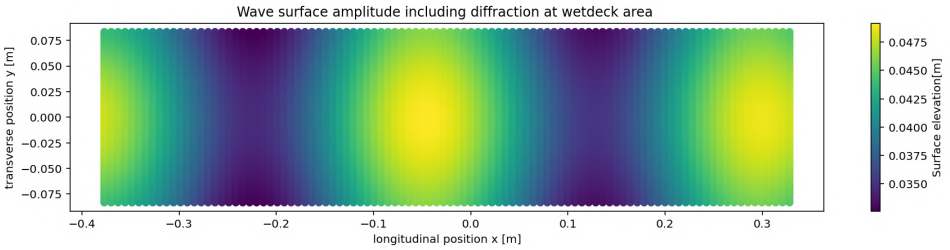

Figure 5.10: Wave surface elevation below the wet deck for $\zeta_a = 30mm$ and $\omega = 10.1rad/s$

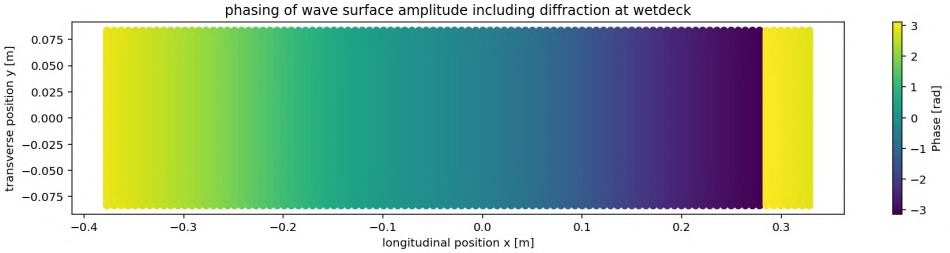

Figure 5.11: Phase of wave surface elevation below the wet deck for $\omega = 10.1rad/s$

5.2.1. Immersion Monochromatic Wave

The wave RAOs were recalculated for the structural mesh, as the forces are ultimately required to be applied to the structural mesh, as discussed in Section 4.3. The immersion case for a wave frequency of 6.5 is shown in this section; Immersion behaviour of wave frequencies 9.5 and 10.1 rad/s is displayed in Appendix A. The Panel centres are plotted in Figure 5.12 where the colour corresponds to the panel Area. The areas are also required to translate the pressures into forces, which are subsequently used to obtain the modal forces. It should also be noted that the panel centres slightly differ. The variation in spacing is beneficial for modelling propagating slam pressures, so that the load is not applied all at once. Additionally, all the areas are quite small, measuring approximately 1x1 mm in size. It can be noticed that most elements are triangular. Since the triangular elements cause inconsistent longitudinal and transverse spacing, resulting in white space. This would slightly decrease the accuracy as the distance between the panel centre and the edges corresponding to that element is slightly larger when compared to a quadrilateral mesh element of the same area.

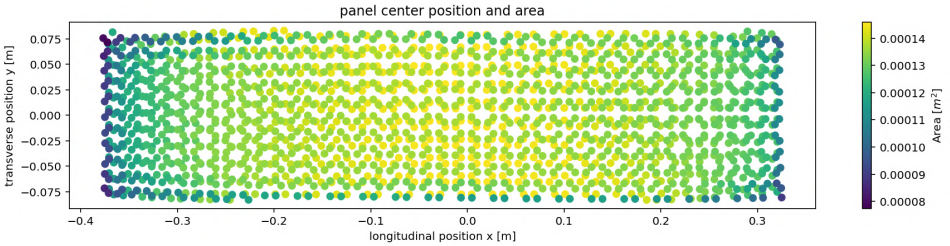

Figure 5.12: Panels and area of the structural mesh.

In Figure 5.13, the wetted time of a panel is shown. The wetted time is the duration during which the structure is submerged for one wave period. For immersion the criteria $z_{rel,d} < 0$ where $z_{rel,d}$ is defined by Eqaution 5.5. The red panels indicate that no wetting occurred. The longest duration of wetting occurred at both ends. This is in line with expectations, as a wave frequency of 6.5 rad/s primarily excited pitching motions. It should be noted that the immersion of these panels does not occur simultaneously. It is a result of pitching motions moving the wet deck closer to flat water; the additional wave elevation causes the fore or aft ends of the wet deck to submerge.

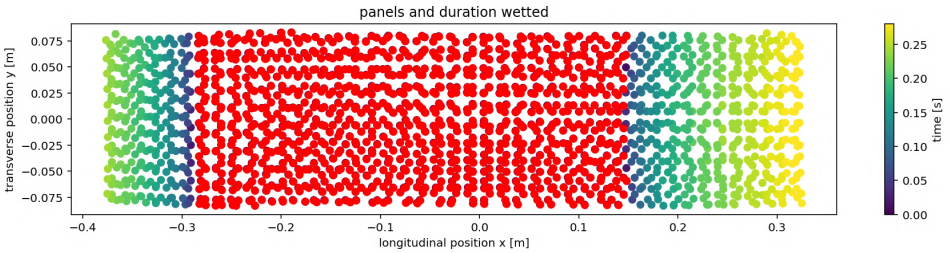

Figure 5.13: Duration of immersion panels in one wave period, red panels were not immersed

Looking at the magnitude of the immersion in Figure 5.14. It can be seen that the most significant values for immersion are at both the forward and aft ends. Again, it is worth noting that these immersions do not occur simultaneously. The forward slam seems to be more intense as a larger negative relative distance is achieved.

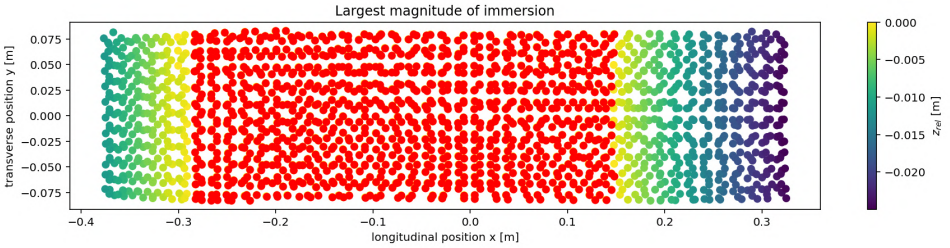

Figure 5.14: Largest immersion experienced by each panel, red panels were not immersed

Figure 5.15 displays the wetting time at which the panels are immersed. Additionally, it can be observed that the events do not occur simultaneously. The two events happen at $t \approx 0$ seconds near the aft of the vessel and at about $t \approx T_{\omega,1}/2 = (2\pi/6.5)/2 = 0.48$ seconds forward. The timescale of each immersion event is approximately 0.16 seconds aft and 0.22 seconds at the fore end of the cross deck. This is equivalent to one-sixth to one-quarter of the total wave period.

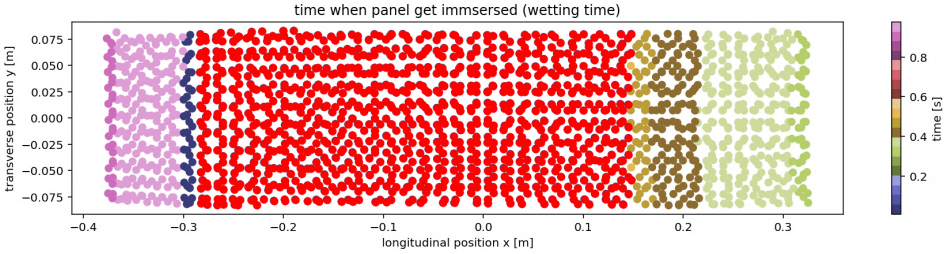

Figure 5.15: Time of wetting for each panel, red panels were not immersed

Other important indicators for assessing slamming are the relative velocity at immersion and the relative angle. The first indicator is crucial for evaluating the severity of a slamming impact. Figure 5.3 shows that at both ends, the slamming velocity was larger with a more pronounced effect forward. The second option is mainly important for a wedge immersion case to assess whether air inclusion would occur. When slamming is of the wave plate impact type, the angle varies greatly. It can be seen in Figure 5.17 that near the front of the wet deck, the immersion is of wave plate impact type. At the aft, the angle is more constant and would be closer approximated by a wedge slam case.

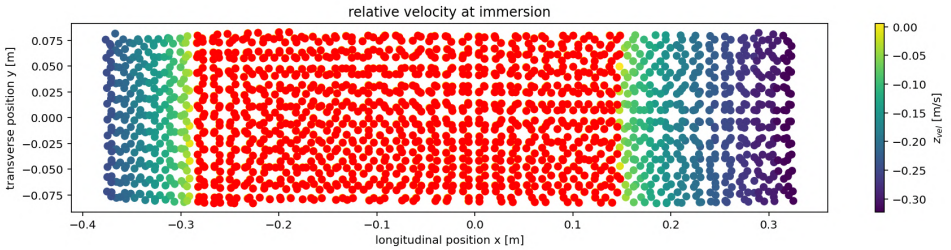

Figure 5.16: Relative velocity between the water surface and the wet deck when the panels get immersed

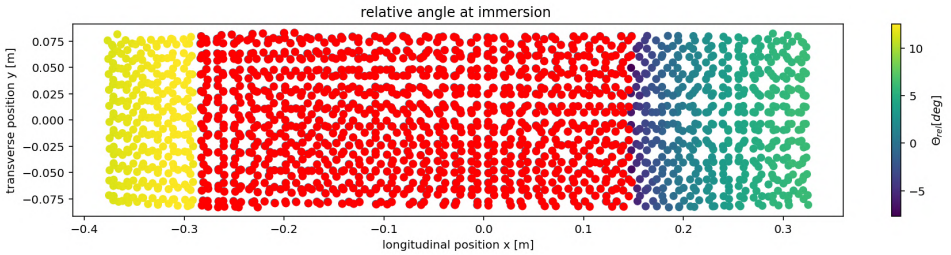

Figure 5.17: Relative angle between the water surface and the wet deck when the panels get immersed

5.3. Relating Immersion to Forces

The duration of the slam was quite long for all chromatic wave cases, as displayed in Figure 5.15 for a wave frequency of 6.5 rad/s. The figures for the other two frequencies are listed in Appendix A. To efficiently excite the mode shapes, loading should have a short duration up to the natural period of the mode shapes. This is approximately 60 ms or shorter. The other two wave frequencies of interest gave greater relative immersion and relative velocities. However, the wetting time was much longer, on the order of 0.2-0.3 seconds, when the waves roll over the bottom of the wetdeck. The slamming theory described in Section 3.4 is made for constant conditions. The loading periods found for monochromatic waves are of a length at which the motions of the vessel change, such that the slamming theories discussed can't be applied accurately. Due to the longer duration, mainly the pitch motions change significantly. To resolve these loading durations for a longer wetting time. The evaluation of the slamming force should be done by actual contact with the wet deck. For this, the BEM calculation should be converted to a transient method where the instantaneous wetted surface is evaluated per timestep. However, this is not compatible with the Green function for the sources, and a significant benefit of the fast BEM method would be lost. Further implications will be discussed in chapter 9

A method to create shorter loading periods that can excite the flexible modes is to investigate the response to a bichromatic wave. The superposition of two waves of constant frequency creates possibilities for a much shorter wetting time. The shorter wetting time is desirable for examining the oscillatory response resulting from a slam using this method. Besides, it would better represent slamming in random sea states where various wave conditions are met.

6. Response to Bichromatic Waves

For the application of the slamming pressure definition, the motions of the vessel should not vary significantly during a slamming event. Therefore, the wetting time of a slam should be relatively short, so that the constant impact velocity and geometry remain valid. These slamming cases are also the most interesting as the wetting times are then smaller than the natural periods. Slamming events of durations longer than the natural periods can still excite a flexible response, but much less efficiently than slams with short wetting time. To obtain wetting of a shorter duration, a superposition of two monochromatic waves is applied. Both waves are described with an amplitude ζ and a wave frequency ω. Where subscripts 1 and 2 indicate the respective waves. The resulting wave loading is then bichromatic, which can create slamming events of shorter duration.

Katsouros conducted experimental measurements of slamming events in bichromatic wave conditions [4]. In his research, only limited slamming was observed, but no significant response was noted in exposure to monochromatic waves. Whereas, for the bichromatic waves, the slamming and whipping response was measured. The tested wave parameters are for total wave heights ranging from 0.04 to 0.07 meters. While the frequencies were in the range of 4 to 7 rad/s, a forward speed of 0.1-0.2 m/s was used.

6.1. Implications and Effects of Bichromatic Waves

To obtain the bichromatic wave properties, a combination of two amplitudes and frequencies is required. The choice for wave amplitude was that both waves were of equal wave amplitude $\zeta_1 = \zeta_2$. For calculations on the bichromatic wave, a ratio was selected between the first and second wave frequencies. The primary frequency is one of the frequencies of interest. A secondary frequency is taken as a ratio of the frequencies of interest. This is done to limit the calculation time while still evaluating all combinations of RAOs. The case considered in this section is a frequency interest of 9.5 rad/s and a secondary frequency of 4/9th of the original which is 4.22 rad/s. Only nine wavelengths of the short wave, with a higher wave frequency, will then result in all the possible superposition cases before repeating itself. The unique combinations of the superpositioned RAOs are displayed in Figure 6.1.

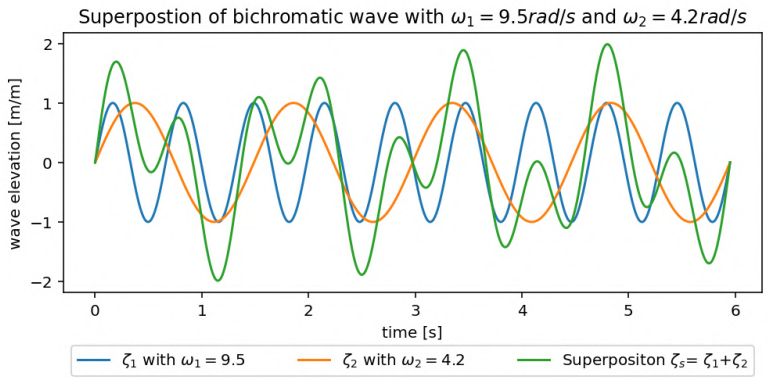

Figure 6.1: Wave surface elevation of superpositioned wave ζ_s for 9 periods of the short wave

The definition of the relative wave distance and relative velocity (Equations 5.5 and 5.6) should also be amended to include the bichromatic wave effect. The result of the superposition effects is displayed in Equations 6.1 and 6.2. In the equations, the subscripts H, P and w indicate motions resulting from heave, pitch and wave surface elevation, respectively. Subscripts 1 and 2 specify the wave which induces the motion. The main difference with the equation of monochromatic wave loading is that each motion component now has a term for each incoming wave. All the motion components are dependent

on an RAO consisting of an Amplitude depicted by RAO and phase ϵ with the corresponding subscript. The equations can be simplified when wave amplitudes are equal, $\zeta_{a,1} = \zeta_{a,2}$. An amplitude of 0.0175 is utilised, as experimental measurements from Katsouros [4] indicate slamming and global vibration response. Then the same steps are repeated as in Section 5.2.1 to determine the most significant wetting and wave. It should be noted that if two waves of 0.0175 m are superposed, the combined undisturbed wave amplitude alone would be 0.035 m. This is a full-scale 12.6-meter wave amplitude, corresponding to sea state 8, and can occur in heavy storm conditions.

$$\begin{aligned} z_{rel,d}(x,y,t) = z_{H,1}(t) + z_{H,2}(t) + z_{P,1}(x,t) + z_{P,2}(x,t) - z_{w1,d}(x,y,t) - z_{w2,d}(x,y,t) + z_{AG}(x,y) = \\ \zeta_{a,1} \cdot RAO_{H,1} \cdot sin(\epsilon_{H,1} - \omega_1 t) + \zeta_{a,2} \cdot RAO_{H,2} \cdot sin(\epsilon_{H,2} - \omega_2 t) \\ + tan(\zeta_{a,1} \cdot RAO_{P,1}) \cdot x_{COG} \cdot sin(\epsilon_{P,1} - \omega_1 t) + tan(\zeta_{a,2} \cdot RAO_{P,2}) \cdot x_{COG} \cdot sin(\epsilon_{P,2} - \omega_2 t) \\ - \zeta_{a,1} \cdot RAO_{w1,d}(x,y) \cdot sin(k_1 x_O - \omega t) - \zeta_{a,2} \cdot RAO_{w2,d}(x,y) \cdot sin(k_2 x_O - \omega t) + z_{AG}(x,y) \end{aligned} \quad (6.1)$$

$$\begin{aligned} w_{rel,d}(x,y,t) = \dot{z}_{rel,d}(x,y,t) = \dot{z}_{H,1}(t) + \dot{z}_{H,2}(t) + \dot{z}_{P,1}(x,t) + \dot{z}_{P,2}(x,t) - \dot{z}_{w1,d}(x,y,t) - \dot{z}_{w2,d}(x,y,t) = \\ - \zeta_{a,1} \cdot RAO_{H,1} \cdot \omega_1 \cdot cos(\epsilon_{H,1} - \omega_1 t) - \zeta_{a,2} \cdot RAO_{H,2} \cdot \omega_2 \cdot cos(\epsilon_{H,2} - \omega_2 t) \\ - tan(\zeta_{a,1} * RAO_{P,1}) \cdot x_{COG} \cdot \omega_1 \cdot cos(\epsilon_{P,1} - \omega_1 t) - tan(\zeta_{a,2} * RAO_{P,2}) \cdot x_{COG} \cdot \omega_2 \cdot cos(\epsilon_{P,2} - \omega_2 t) \\ + \zeta_{a,1} \cdot RAO_{w1,d}(x,y) \cdot \omega_1 \cdot cos(\epsilon_{w1,d}(x,y) - \omega_1 t) + \zeta_{a,2} \cdot RAO_{w2,d}(x,y) \cdot \omega_2 \cdot cos(\epsilon_{w2,d}(x,y) - \omega_2 t) \end{aligned} \quad (6.2)$$

6.2. Immersion Bichromatic Waves

The process of determining immersion from Section 5.2.1 is repeated for the superpositioned wave. The wave amplitudes and phasing are displayed in Figures 6.2 and 6.3. The first wave has an angular frequency of 9.5 rad/s, the same as in Section 5.2.1 but with a smaller amplitude. The second wave is of frequency 4.2 rad/s, which is within 0.5% of 4/9th ω_1. This second frequency is a ratio of the first frequency, which reduces calculation time, as explained in Section 6.1. The second wave ζ_2 results in a smaller amplitude of surface elevation compared to the first wave ζ_1. In Figure 6.3a, the largest amplitude is near the front, and it reduces over the length due to interaction with the hull. For the first wave, the interactions result in a wave surface amplitude greater than that of the incoming wave, as is displayed in Figure 6.2a.

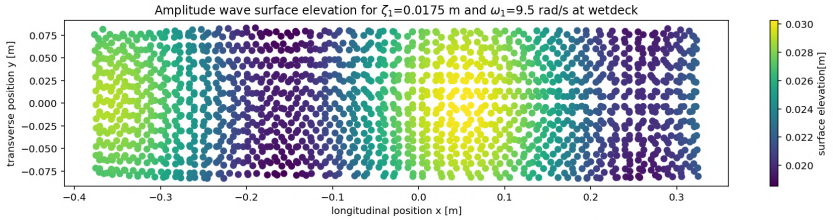

(a) Amplitude of wave surface elevation for ζ_1

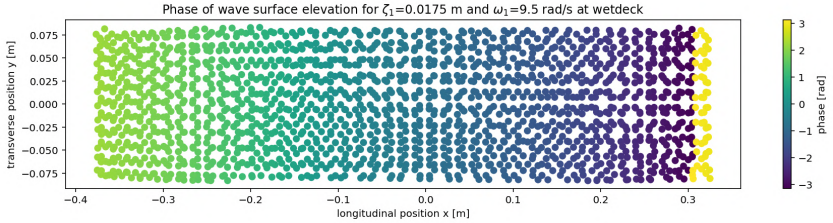

(b) Phase of wave surface elevation for ζ_1

Figure 6.2: Amplitude and phasing of ζ_1 for $\zeta_{a,1} = 0.0175$m and ω_1=9.5 rad/s

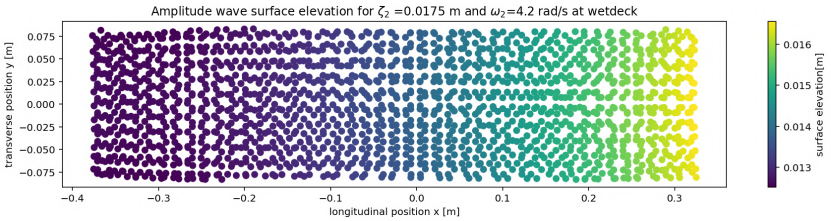

(a) Amplitude of wave surface elevation for ζ_2

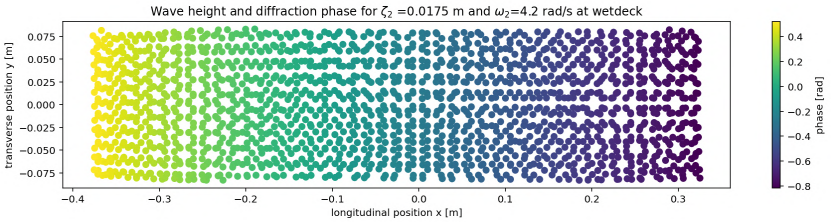

(b) Phase of wave surface elevation for ζ_2

Figure 6.3: Amplitude and phasing of ζ_2 for $\zeta_{a,2} = 0.0175$m and ω_2=4.2 rad/s

To observe the bichromatic wave effect on a panel, the whole domain of the superposition should be examined. All panel identifiers are shown in Figure 6.4, where the red dot indicates panel 1692. Figures 6.5 and 6.6 display the relative wave height and relative velocity, respectively. It can be seen that multiple immersion events occur for the superposition wave components. The relative velocity is approaching peak negative values when immersion occurs.

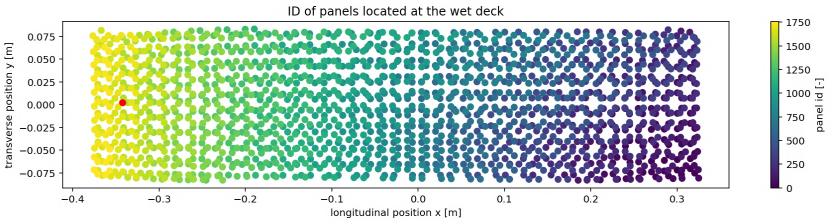

Figure 6.4: ID of panels where panel 1692, located aft, is highlighted red

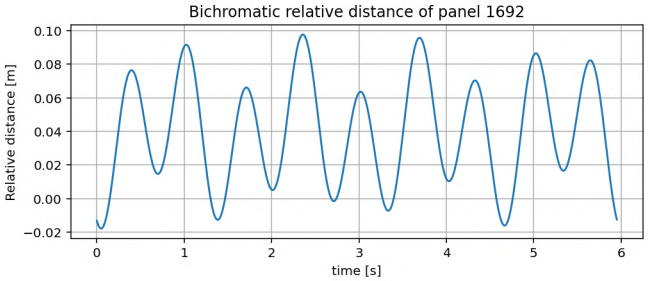

Figure 6.5: Relative distance z_{rel} for bichromatic wave $\zeta_s = \zeta_1 + \zeta_2$ excitation at panel 1692, which is located aft

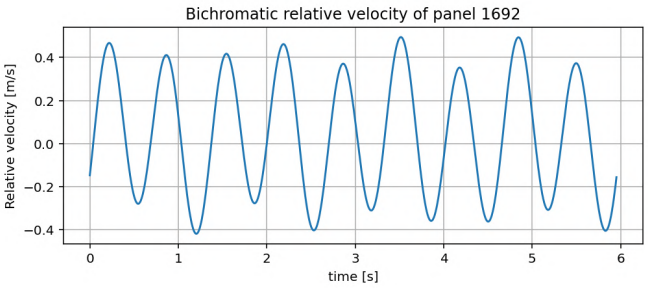

Figure 6.6: Relative velocity for bichromatic wave $\zeta_s = \zeta_1 + \zeta_2$ excitation at panel 1692, which is located aft

The investigation of point 1692 is conducted on the entire wet deck, and all slamming events can be obtained in the domain of the superposition wave ζ_s. Figure 6.7 shows that some panels were immersed multiple times, but the largest area of the wet deck was never submerged. This was especially true for the area in the centre. To investigate the response, the most extreme immersion event is used to calculate the slamming pressure and time trace. The most significant immersion event is defined as the greatest negative relative distance of the panel shown in Figure 6.9. The time of the most significant immersion event varies for each panel of the wet deck. Figure 6.8 showcases three significant immersion events along the hull. Among the various immersion events, a single one should be selected for evaluating the force and subsequent response. Interaction between the response to a previous slam event and the slam force will be discussed in Section 6.5.3. What can also be seen in Figures 6.9 and 6.10 is that both the relative wave height and the relative velocity are the greatest aft for the immersion event starting at 5.9 seconds. Thus, the immersion event occurring at 5.9 seconds will be used to calculate the slamming forces resulting from the immersion.

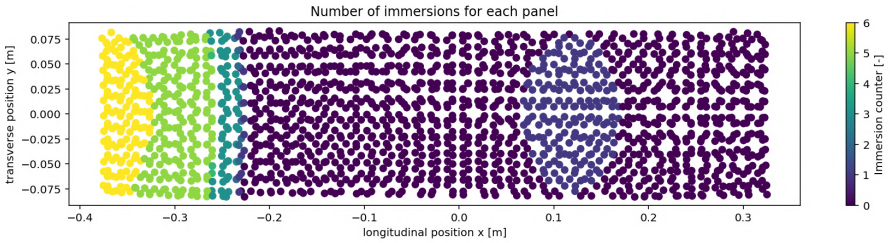

Figure 6.7: Number of immersions for each panel on the wet deck

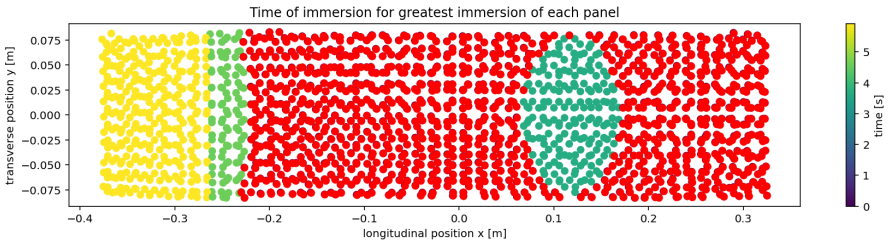

Figure 6.8: Time of the largest immersion for each panel on the wet deck, the red panels were not immersed

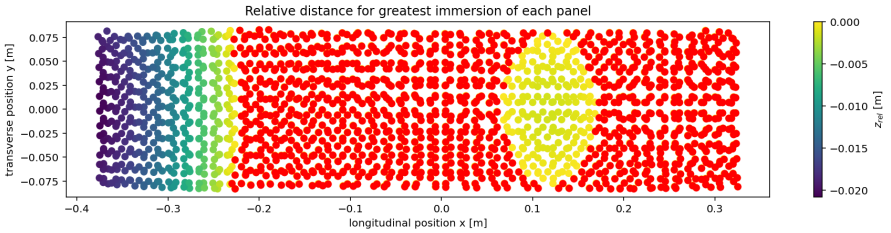

Figure 6.9: Relative distance of the largest immersion for each panel on the wet deck, the red panels were not immersed

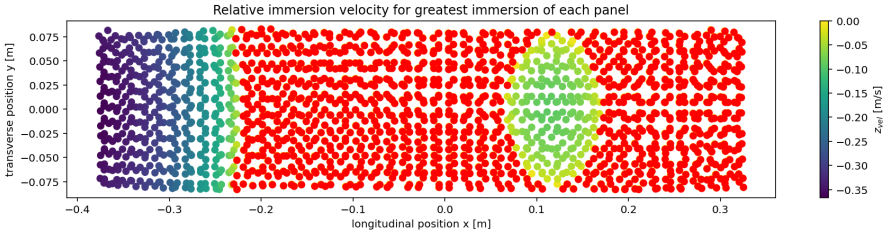

Figure 6.10: Relative velocity at the largest immersion for each panel on the wet deck, the red panels were not immersed

When investigating the slam related to the most significant immersion event, it is isolated by only taking immersion within 0.2 seconds of the initial immersion. Figures 6.11 and 6.12 show the immersion time into the slam event and relative wave height. The immersion time indicates that the slam event lasts only 14 ms. It can also be seen that it is of flat plate impact type, with the slam moving in both directions. Thus, the goal of applying bichromatic waves appears to be successful in terms of an immersion event of short duration. Then all parameters of the equation 3.15 are present. The wetted length c(t) and immersion velocity are extracted. Two variants of the equation will be applied to derive the pressure. The first is Equation 6.3 where the slamming velocity is the average of all wetted panels. The second variant (Equation 6.4) is defined with a constant slamming velocity per panel but averaged over space. As can be seen in Figure 6.10, the slamming velocity mainly changes in the longitudinal direction, resulting from a combination of more extreme wave RAO and pitching velocity due to motions. wave RAO and pitching velocity as a result of ship motions.

$$P_{slam}(x,t) = \rho \bar{V} \frac{c(t)}{\sqrt{c(t)^2 - x^2}} \frac{dc}{dt} \tag{6.3}$$

$$P_{slam}(x,t) = \rho V(x) \frac{c(t)}{\sqrt{c(t)^2 - x^2}} \frac{dc}{dt} \tag{6.4}$$

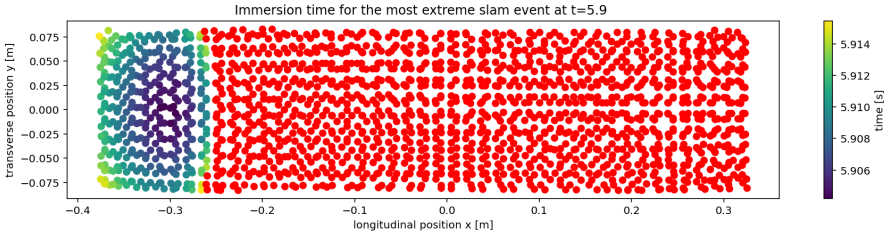

Figure 6.11: Wetting time of each panel for the most significant slam at t=5.9s

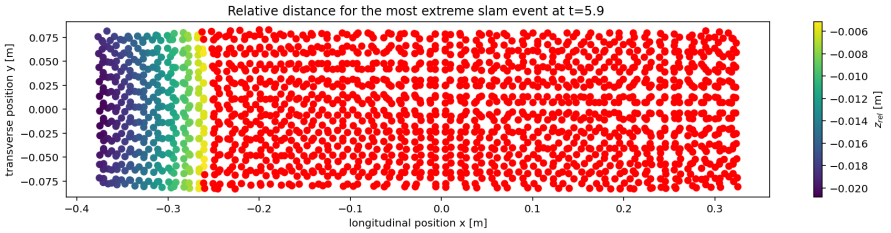

Figure 6.12: Relative distance z_{rel} of each panel for the most significant slam at t=5.9s

6.3. Wetted Length and Immersion Velocity

In Figure 6.13, the c(t) over time and relative velocity over space are plotted. These are both backwards and forward propagating from $x_{COG,initial} = -0.3067$ m. Figures 6.13a and 6.13b plot the points of wetting length against wetting time for the backwards and forward slam. Through these plots, linear, quadratic, and cubic polynomials are fitted. Quality of the fit appears to be relatively poor for the forward-propagating wave 6.13b, but the wetting length is also quite limited. The differences between the fits are almost negligible, except that the linear and quadratic polynomial fits tend to overshoot the wetting length. For the immersion velocities, Figures 6.13c and 6.13d show that the immersion velocity is greater for the backwards propagating slam. The figure also illustrates why an averaged velocity might be a crude estimate of the actual situation at hand. Whilst the immersion time is very short, the slam impact and resulting motions have minimal time to affect the magnitude of individual slam velocities. Additionally, the global ship motions are more determined by wave loading instead of a local excitation as a result of a slam. This is likely to induce only an oscillatory response due to the short loading period. Both the linear and quadratic fits of the c(t) will be utilised. For the velocity, a global constant slamming velocity $\bar{v}$ and a cubic fit for the relative immersion velocity $v(x)$ are investigated.

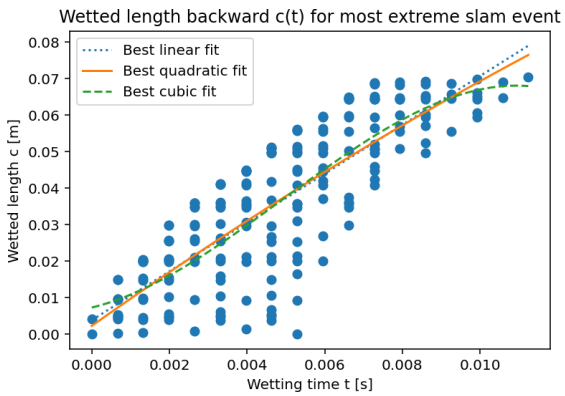

(a) Wetted length over time for backwards propagating slam

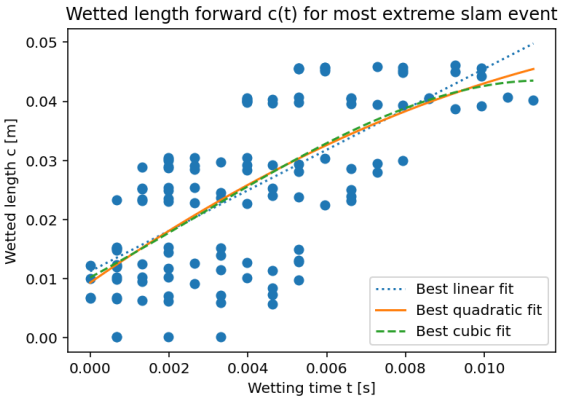

(b) Wetted length over time for forward propagating slam

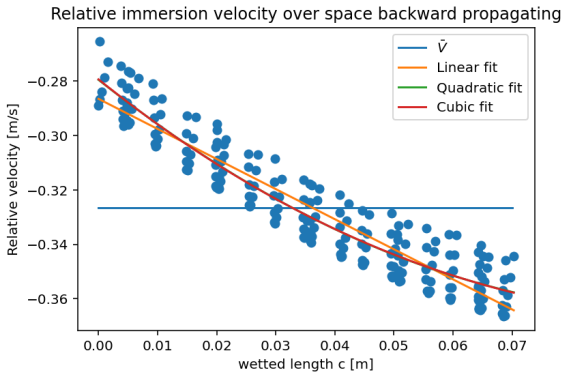

(c) Immersion velocity over length for backwards propagating slam

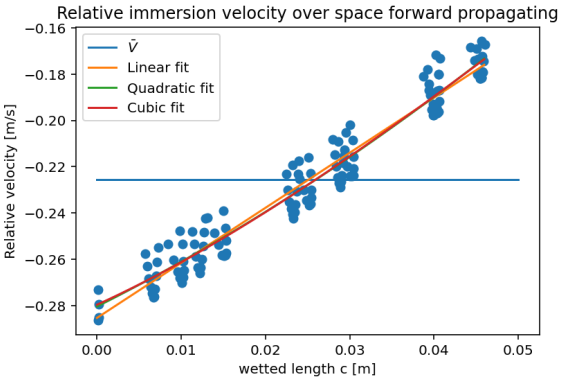

(d) Immersion velocity over length for forward propagating slam

Figure 6.13: Wetted length and velocity of most significant slam event of $\zeta_s = \zeta_1 + \zeta_2$, starting at 5.9 seconds

6.3.1. 3-Dimensional Effects in Immersion

Initially, the slamming events appeared to be mostly 2D propagating in the longitudinal direction. However, as shown in Figure 6.8, the very short-duration slam also exhibits a transverse component. The transverse component primarily affects the immersion time and has virtually no impact on the relative wave height. The minor 3D effects also lead to the large horizontal spread in the c(t) Figures 6.13a and 6.13b. The spread causes the fit for the c(t) propagating forward to be of poor quality. One way to improve the inclusion of these 3D effects would be to use small transverse strips, on which this process is repeated, to more accurately model the slam. This will be further discussed in Chapter 9. These 3D effects also impact the slamming angles; therefore, they cannot accurately be described by only the longitudinal direction. However, the impact case closely represents a wave plate impact where the angle of the wave surface limits the effect of air inclusion for very shallow slamming angles. The criteria on the relative angle cannot be checked numerically in this way and will be further discussed when validating numerical results in Chapter 7.

6.4. Relating Bichromatic Wave Immersion to Forces

Now, with various definitions of the wet length and immersion velocities, the slamming pressures can be evaluated. In Figure 6.14, the pressure over the wet deck is displayed at six time steps. It also indicates five points at which pressure time traces are depicted in Figure 6.15. It can be seen that, from the initial impact, the pressure travels in both directions. The peak slam values tend to increase later into the slam. However, the proximity to the singularity has a greater effect on the peak value. The reason for the prominent peak is that when the panel location and wetted length are very close, the $\sqrt{c(t)^2 - x^2}$ term approaches zero, and pressures then become much greater. The singular peak of pressure can be observed in Figure 6.15.

The pressure plots tend to increase for the points at greater wetted length. What also can be seen is that if a global slamming velocity $\bar{V}$ is used that it generates a higher pressure in the early stages (Figures 6.15a and 6.15b) while, in the later more advanced slamming stages the pressure is lower. What can also be observed is the difference between the linear and quadratic c(t) definitions. Where the quadratic wetted length slightly lags the linear wetted length. The difference is showcased by later slamming peaks (Figures 6.15a and 6.15e). However, the quadratic wetted length creates an earlier pressure peak at point C shown in Figure 6.15c. All these combinations of pressure definitions are considered in Chapter 7, which is the validation stage. To compare whether the various definitions have an impact on the comparison between numerical results and experimental measurements. The pressures resulting from other pressure definitions are shown in Appendix B.

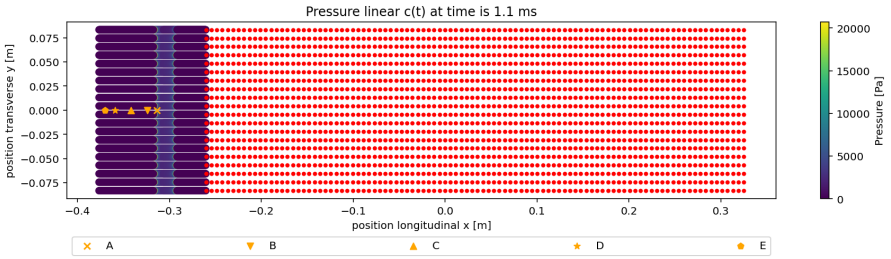

(a) Slamming pressure at 1.1ms into slam event

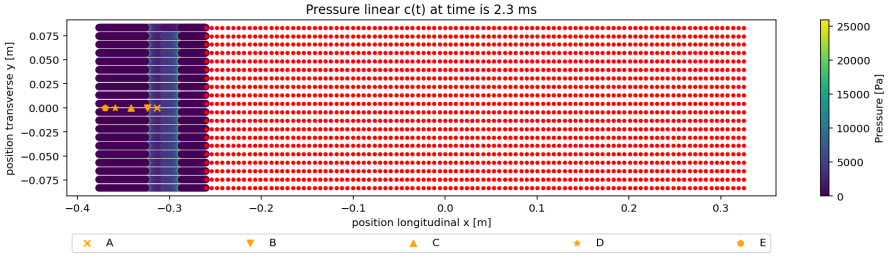

(b) Slamming pressure at 2.3ms into slam event

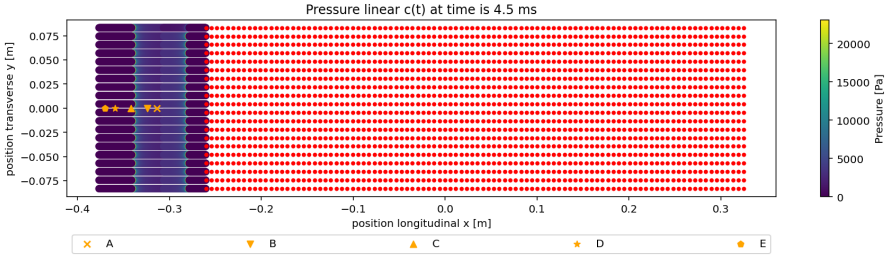

(c) Slamming pressure at 4.5ms into slam event

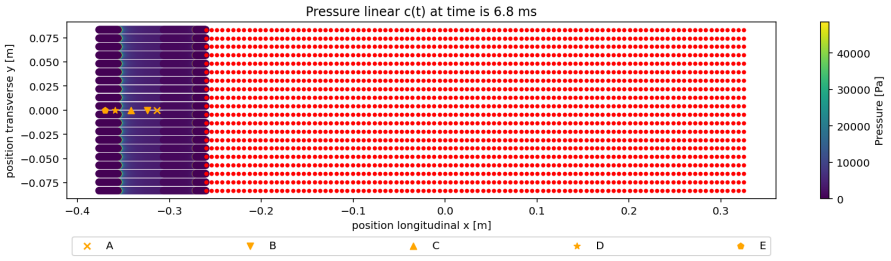

(d) Slamming pressure at 6.8ms into slam event

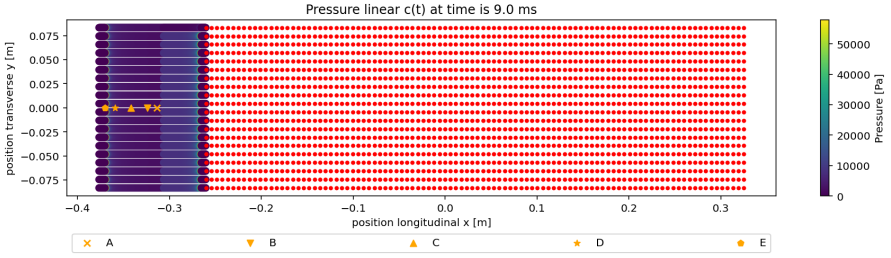

(e) Slamming pressure at 9.0ms into slam event

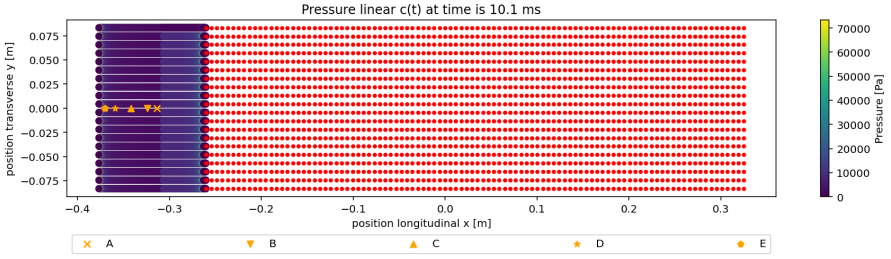

(f) Slamming pressure at 10.1ms into slam event

Figure 6.14: Pressures during slamming event starting at t=5.9s, resulting from pressure definition based on linear c(t) and slamming velocity V(x)

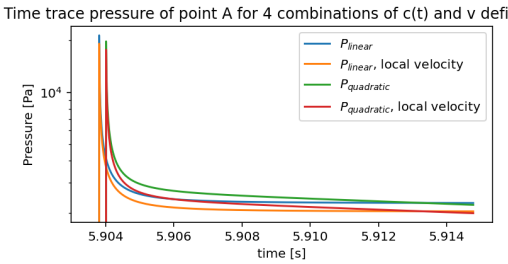

(a) Log-scaled slamming pressure at point A over slam event

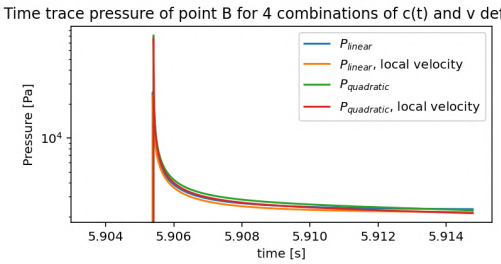

(b) Log-scaled slamming pressure at point B over slam event

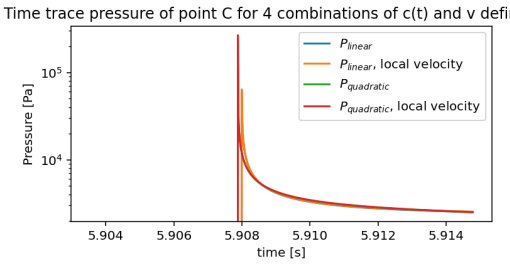

(c) Log-scaled slamming pressure at point C over slam event

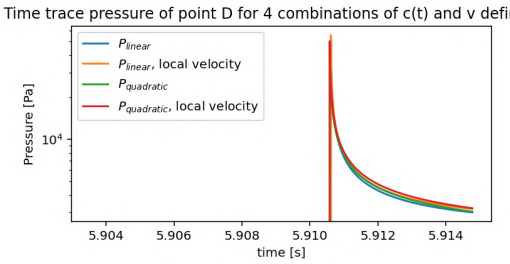

(d) Log-scaled s pressure at point D over slam event

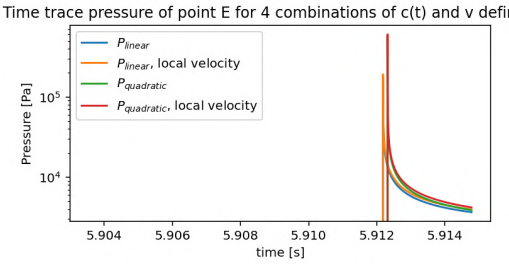

(e) Log-scaled slamming pressure at point E over slam event

Figure 6.15: Pressures of Points A through E during a slamming event starting at t=5.9s

6.5. Oscillatory Response to Slamming

6.5.1. Modal Force

The slam pressures obtained in the last section are mapped to the modal space with the Dry modal displacement vectors as explained in Section 4.3. In Figure 6.16, the various vertical modal displacements Ψ_z of the four flexible mode shapes are plotted. Only the z component of the mode shape is used, as this part represents the part of the normal vector to the wet deck. At the aft section, all mode-shapes have a large transverse gradient of the vertical modal displacements Ψ_z. A slam that travels in the longitudinal direction will result in a limited response. This results in partially cancelling out the excitation of the mode shape, except for the first mode displayed in Figure 6.16a, where all values are negative. As a result, the first mode will be excited more than the others for this slamming event.

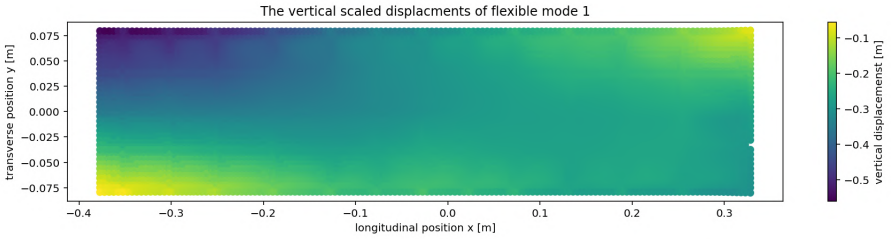

(a) Vertical displacements 1st mode shape Ψ_z on the wet deck

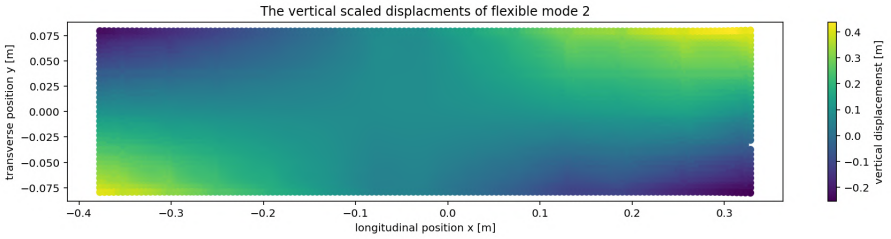

(b) Vertical displacements 2nd mode shape Ψ_z on the wet deck

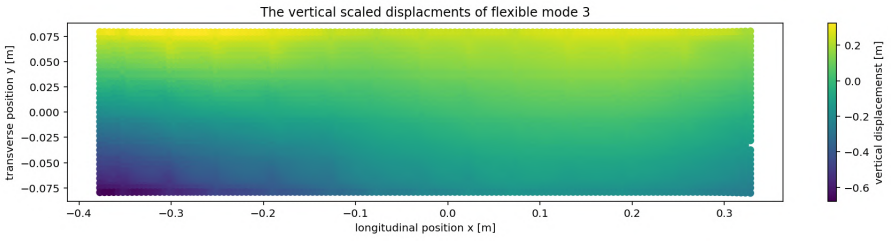

(c) Vertical displacements 3rd mode shape Ψ_z on the wet deck

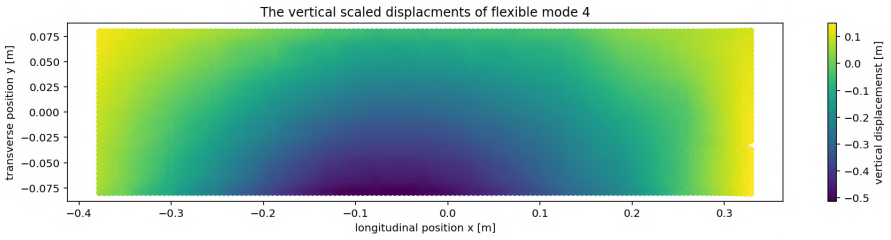

(d) Vertical displacements 4th mode shape Ψ_z on the wet deck

Figure 6.16: z-component of the four flexible modes of the wet deck

The modal force over time for each panel n is obtained with Equation 6.5. The pressures obtained in Section 6.4 then result in modal forcing over the wet deck, which is displayed in Figure 6.17. This indicates that the pressure remains zero until the material is wetted, and the immersion front makes a significant contribution to the modal force. As a result of the mode shape from Figure 6.16c, the pressures can lead to both positive and negative modal forces at the same time due to the sign of $\Psi z, n, i$. By doing this for all elements and summing the result, the modal force excitation $f_{m,total,i}(t)$ is obtained. The i indicates the mode of the modal force. In the calculation of excitation, the four modes are combined into the vector $\vec{f}_{m,total}(t)$

$$f_{m,n,i}(t) = A_n * P_{slam,n}(t) * \Psi_{z,n,i} \tag{6.5}$$

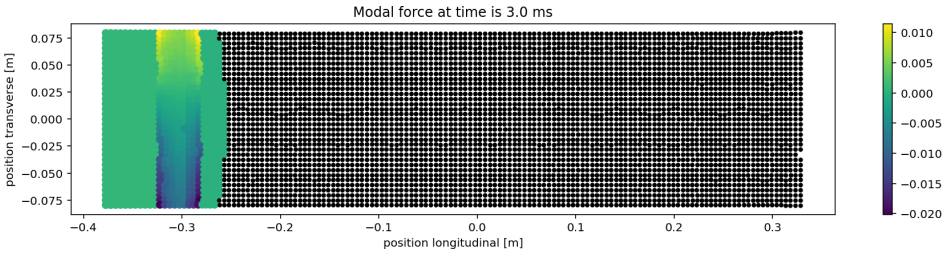

Figure 6.17: Modal force of the 3rd mode at 3ms into the slamming event

6.5.2. Wet Mode Excitation

The forced modal excitation, as described in Equation 2.6, is listed below again. Now the modal masses, stiffness and forces are known. What remains unknown is the resulting displacements $\vec{u}$ and accelerations $\ddot{\vec{u}}$ over time. To evaluate those, a 4th-order Runge-Kutta integration scheme is applied. It is a forward-propagating scheme where, from initial conditions and a time trace of the force, a derivative is approximated for a given time step. This derivative is subsequently used to calculate the value of the next time step. This process is iterated until the end time is reached. One thousand time steps were used for the integration of the wetting length, resulting in a time step of 0.0119 milliseconds, or $1.19 \cdot 10^{-5}$ seconds. The end time was set at 0.047 seconds, which is four times the wetting time.

$$([M_m] + [A])\ddot{\vec{u}}(t) + ([K_m] + [C])\vec{u}(t) = \vec{f}_{m,total}(t)$$

The modal excitation over time of the four modes is displayed in Figure 6.18. What can be observed is that the various modes are excited as a result of the force, which ends at t = 11.9 ms. Peak amplitudes as a result of the slamming force are reached after the slam peak, where the first two modes with a lower frequency reach their peak much later as compared to the third and fourth flexible modes. The a_i, plotted on the y-axis, indicates the value which is subsequently multiplied by the mode shape to obtain the displacements. The magnitude of a_i is quite small at a largest value of approximately 10^{-4}, but the corresponding mode shapes were scaled to a unit vector of 1 meter. Thus, the largest displacement values should be on the order of 0.1 millimetres; this still appears to be small and should be compared to experimental results. The largest displacement value can also occur for a position that is not on the wet deck. Thus, the vertical wet deck response would be of even smaller magnitude than the 0.1 millimetres indicated.

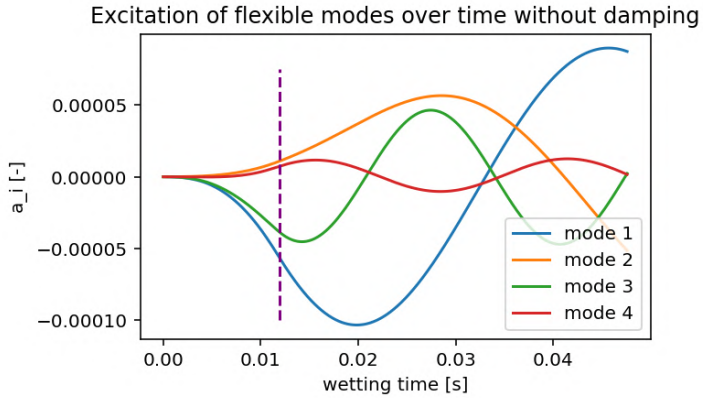

Figure 6.18: Modal excitation of flexible modes over time, purple dashed line indicates end of application slamming force

Response of the top deck

In Figures 6.19, 6.20, 6.21, and 6.22, the displacements of the top deck at 20 ms into the slam event are displayed for the four flexible modes. The flexible mode shapes of the wet deck from Figure 6.16 can be recognised. There is a difference; instead of plotting the displacements only on the wet deck, they are now plotted on the top deck, causing some deviation from the mode shapes.

On local response

There are some essential factors to discuss. The information about the position and the quantity of slamming pressure is lost in the step of calculating the response. In reality, an initial local response will be excited. The local loads and response then propagate to a global response. This process of transfer from local to global response is not modelled. The entire local part of the calculation is omitted.

The feasibility of local response calculation was investigated, but significant issues arose. The elemental stiffness and mass matrices of the model made the calculations impractical. The resulting dry modal matrices are approximately 900,000 by 900,000; the partial results of Capytaine should then be mapped to the corresponding elements to obtain the wet modal data. However, there is a limit to the small mesh sizing that could be evaluated in Capytaine, as was explained in Section 4.2.2. This could be interesting for further investigation, as will be further discussed in Chapter 9. The implications are that a smaller response on the wet deck might be displayed in the early slamming stages compared to experimental measurements. This is a result of the excited mass being the total modal mass of the structure for the particular mode. Nevertheless, after the propagation stage of the loading, the results reflect the global motions. The global displacements and accelerations can be compared to research data; this validation step will be taken in Chapter 7.

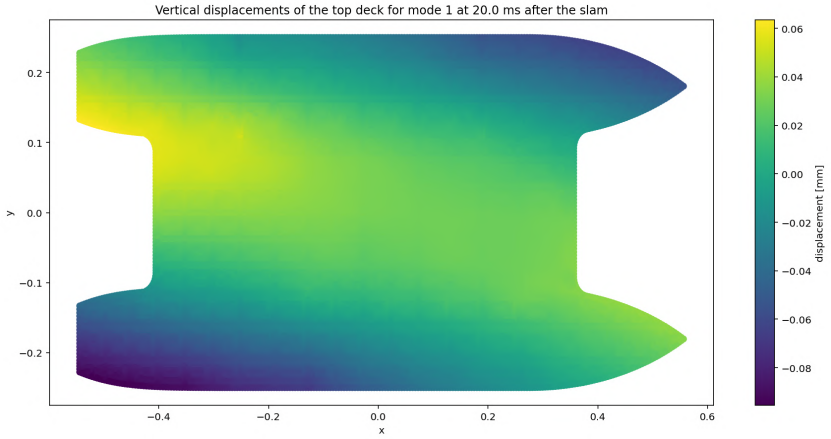

Figure 6.19: Vertical modal displacements 1st mode of the top deck as a result of slamming impact at 20ms after impact.

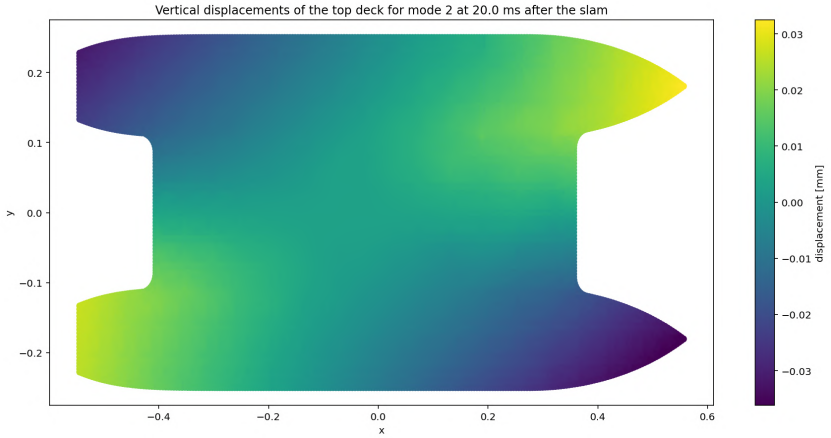

Figure 6.20: Vertical modal displacements 2nd mode of the top deck as a result of slamming impact at 20ms after impact.

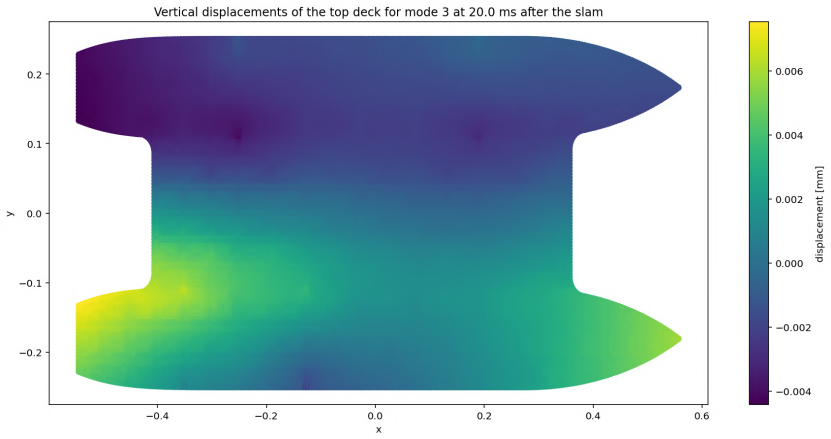

Figure 6.21: Vertical modal displacements 3rd mode of the top deck as a result of slamming impact at 20ms after impact.

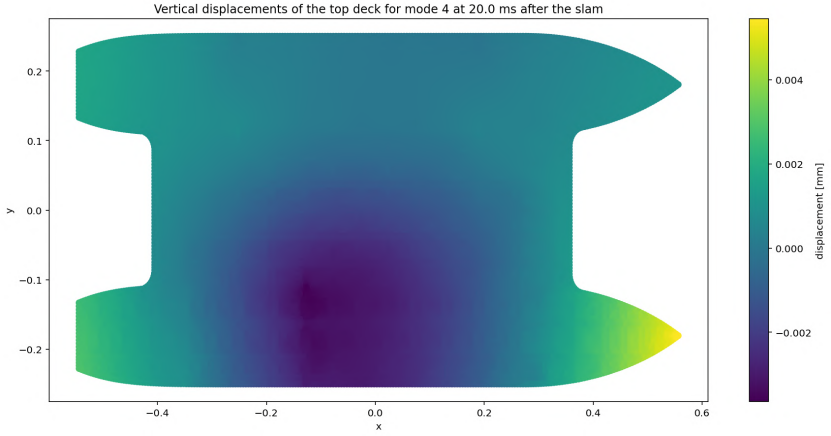

Figure 6.22: Vertical modal displacements 4th mode of the top deck as a result of slamming impact at 20ms after impact.

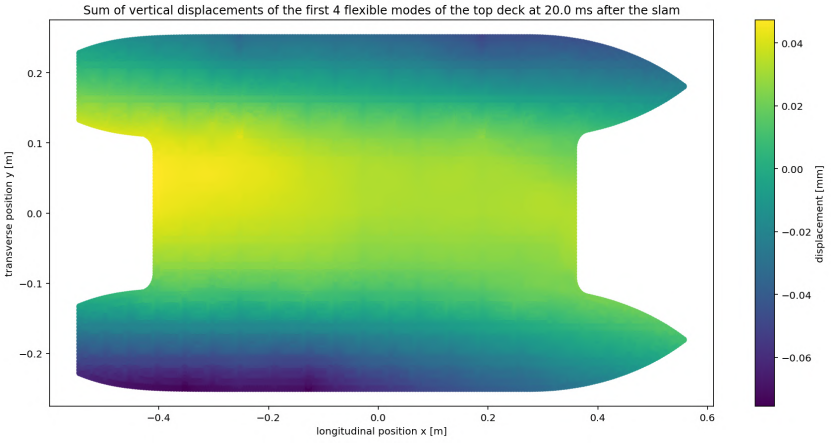

Figure 6.23: Summed vertical displacements of the first four flexible modes of the wet deck at 20ms after slamming impact

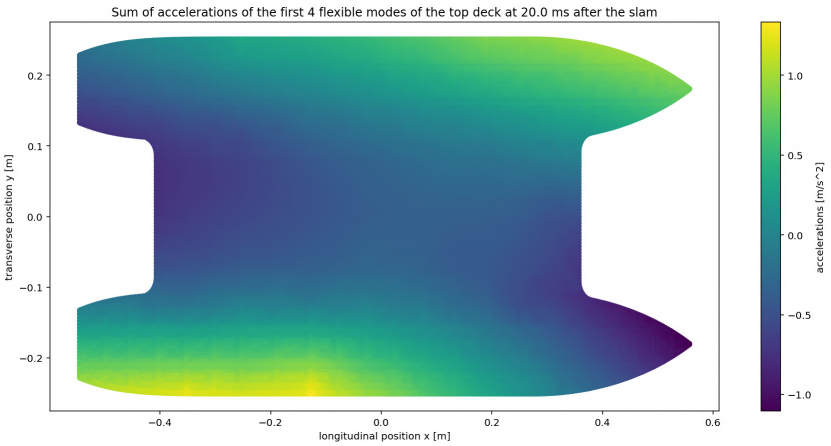

Figure 6.24: Summed accelerations of the first four flexible modes of the wet deck at 20ms after slamming impact

6.5.3. Damping of the Flexible Modes

After the initial excitation, the decay of the flexible response can be of interest for fatigue evaluation. Vibrations at high frequencies can accumulate significant load cycles quickly. Whilst the resulting stresses of the slamming response may not be substantial, it should be noted that these are in addition to the stresses already experienced from wave loading and the still-water bending moment. The stress levels at which the cycles are experienced can still lead to an oscillatory response that is of importance.

In Figure 6.25, the peak excitation is plotted with a subsequent decay of 3% per cycle. This value is representative of values found in the literature. The damping is also comparable to values found in experimental measurements by Katsouros [4], where almost all of the flexible response would decay within one second after a slamming event. The decay has further implications for the application of two-way coupling. In the methodology, it was proposed to use the flexible response in the immersion velocity. Through this step, the structural response would also affect the slamming loads. However, if the flexible response has fully decayed before the next slamming event, no two-way coupling of this effect is possible. If the intervals between slamming events were small enough, it is feasible to include flexible motions in the slamming velocity. The immersion intervals of the bichromatic wave are 1.5 seconds (Figure 6.5) in which the response has almost entirely decayed. Thus, it is not possible to include a two-way response in the immersion velocity. There is one caveat: the required accuracy of the response is very high. Since a slight difference in time could have a significant impact on the instantaneous slamming velocity, due to the vibrations occurring at high natural frequencies compared to the incoming waves.

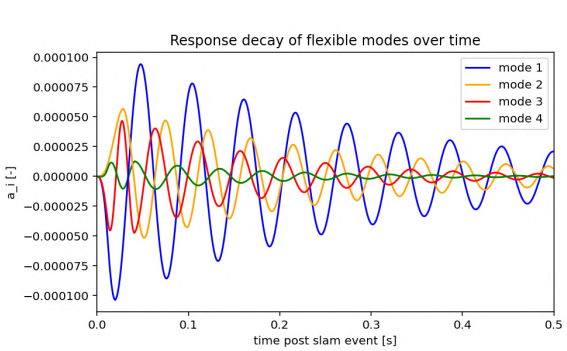

(a) Initial decay of flexible response as a result of damping

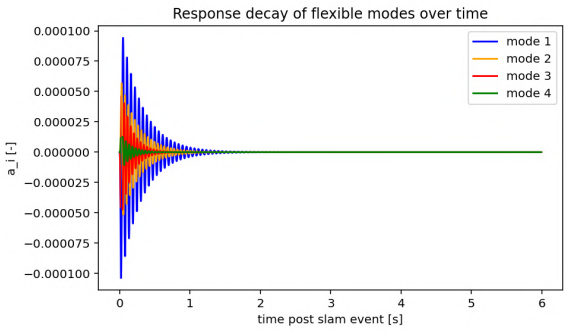

(b) Decay of flexible response as a result of damping until the next significant slam event

Figure 6.25: The decay of flexible response as a result of forced 3% damping

7. Validation Against Experimental Measurements

Katsouros [4] measured the accelerations and displacement resulting from slamming impacts in both monochromatic and bichromatic wave conditions. In this chapter, the experimental setup and its implications will be briefly covered and compared to the numerical results. Following previous verification steps within the various modelling programmes, this validation step will assess whether the model applied accurately represents the dominant physical phenomena.

7.1. Experimental Measurements

To obtain the accelerations and displacements, a rather complex experiment was required due to the combination of measuring devices and the flume tank. The water is recirculated in the flume tank, allowing for longer test runs, since there is no limit to the towing tank length. This is desirable for a frequency domain analysis, as the vessel should exhibit motion similar to the calculated RAOs over time. The data was further processed, and the flexible accelerations obtained resulting from slamming impacts. To identify whether whipping occurred due to the slamming impacts, an instantaneous energy criterion was applied.

7.1.1. Experimental Setup

The experiment is conducted in a flume tank with currents of 0.1 and 0.2 m/s. The waves are created by an actuated flap controlled by a voltage signal. To compensate for the vessel's drifting, a mooring system is applied. Avoidance of the natural surge period was achieved; this is possible since mono- and bichromatic waves have constant frequencies. The entire setup is displayed in Figure 7.1.

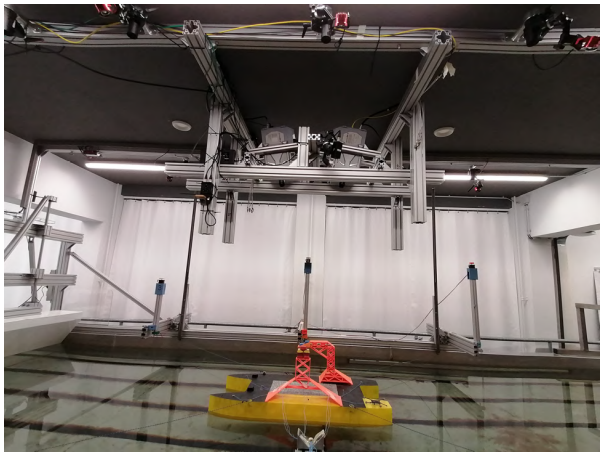

Figure 7.1: "Experimental setup"[4]

A tracking marker is recorded with multiple cameras at various angles to determine the rigid body motions. On an area of 100 by 200 millimetres, A speckle pattern was applied. The speckle pattern is positioned in the centre of the top deck, shown in Figure 7.2. The speckle pattern is applied to make Direct Image Correlation (DIC) measurements during the wave loading. The DIC measurements are utilised to extract displacements of the top deck. Displacements of the wet deck are preferred. However, a clear line of sight through the structure is not possible. The last type of data measurement device used was accelerometers, located in eight positions. Dewesoft was used for synchronising the sensor's signals. This synchronisation is required for further analysis of the measurements. The

accelerometers were positioned in locations where significant deflection occurs, as determined by the dry and wet modal analysis. The accelerometers were attached to the top of the deck. The longitudinal and transverse positions of the accelerometers are displayed in Figure 7.2 and Table 7.1.

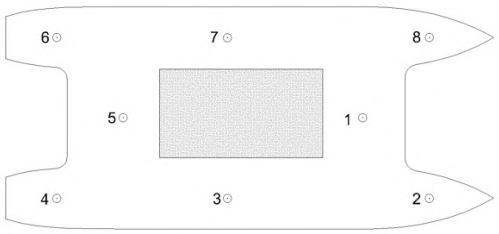

Figure 7.2: "Position speckle pattern and accelerometers" [4]

Table 7.1: "Coordinates Accelerometers" [4]

Sensor	x_O [mm]	y [mm]
1	850	0
2	955	-180
3	500	-180
4	115	-180
5	265	0
6	115	180
7	500	180
8	955	180

Limitations Experiment

There were a couple of limitations to the experiments; The first was that wave frequencies up to 7 rad/s could be applied. For higher wave frequencies, refraction would occur against the walls and the wave-damping beach. These refraction effects created standing waves that interacted with the flexible model.

The second limitation was that DIC measurements could not accurately determine the excitation of the flexible modes. This was a result of a combination of three factors, the first of which was a relatively small measured area. The second factor is that in the small area, the flexible mode shapes did not differ significantly. The last factor is that the quality of the speckle pattern was not great. All factors combined resulted in difficulties in separating the flexible response from noise in the signal.

The measurement of local response was not possible because the acceleration sensors were not located on the wet deck. This is not as much of a problem for validation as the method applied in this thesis also does not model the local structural response.

7.1.2. Experimental Acceleration and Slamming Data

Many combinations of frequencies of the bichromatic waves were tested. In the experiment, slamming and global whipping responses were found for multiple cases. The global response was most notable for run 5_76, where the parameters included a maximum wave height of 0.07 m, two wave frequencies of 4 and 7 rad/s, and a current of 0.1 m/s was applied.

The acceleration signal in this case was decomposed into eleven intrinsic mode functions using the empirical mode decomposition (EMD) method. The decomposition, combined with a Butterworth filter allowed to asses the flexible response. In Figure 7.3, the flexible accelerations are displayed. The accelerations were filtered to include only frequencies within the range of 10 to 50 Hz, which are essential for the flexible response. The accelerations reached peak amplitudes between 0.5 and 3.2 m/s^2 with random noise on the order of 0.1 m/s^2. Commenting on the exact time trace at a highly detailed time scale is not relevant. Due to the effect of simplifying assumptions and noise in the measurements, the proposed method lacks the detail to include the local excitation effects.

Nevertheless, comparing against the order of magnitude and the intervals between slam occurrences is meaningful for validation. In Figure 7.3, the interval between a smaller slam and a subsequent larger slam is 0.7 seconds, after which no slam occurs for the next 4 seconds. In Figure 7.4, A longer time trace with identified slams is displayed. It can be seen that even though bichromatic wave loading is applied, the response is not only bichromatic. The slamming events are clusters of small slams, occurring between 1 and 3 seconds, with a few heavy slamming events.

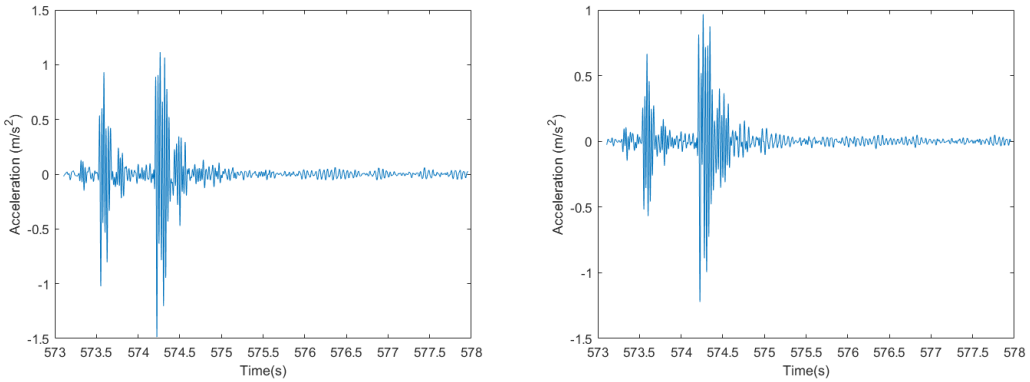

(a) Sensor 1

(b) Sensor 5

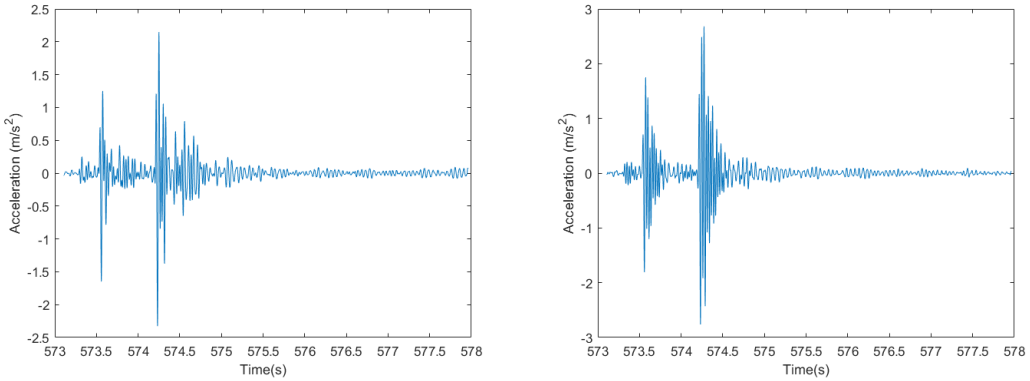

(c) Sensor 8

(d) Sensor 2

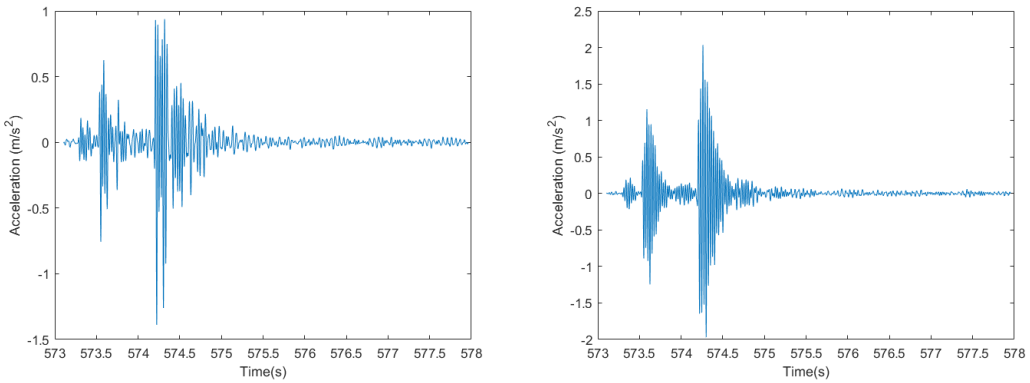

(e) Sensor 7

(f) Sensor 3

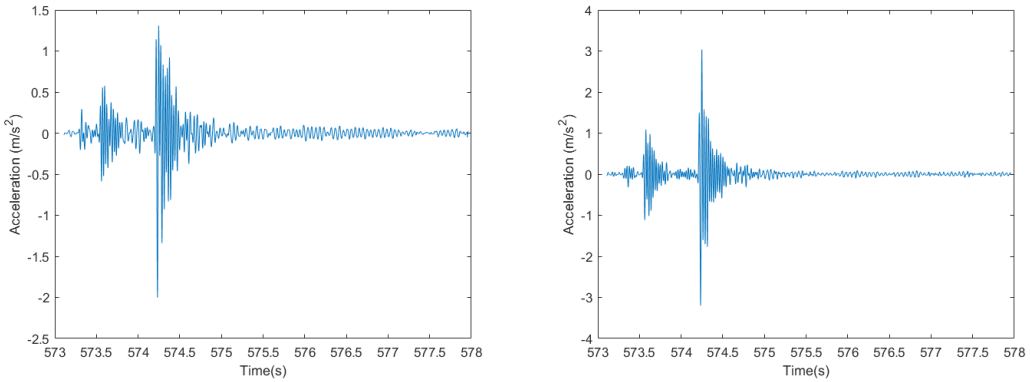

(g) Sensor 6

(h) Sensor 4

Figure 7.3: ”Zoomed in hydroelastic responses of slamming for run 5_76” [4]

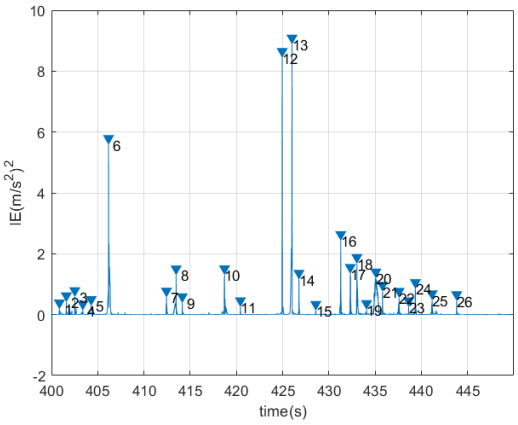

Figure 7.4: "Slamming events identified by the EMD of run 5_76"[4]

7.1.3. Experimental Whipping Evaluation

A whipping-based slamming criterion proposed by Alsalah [7] was applied. The criterion identified a slamming occurrence when the instantaneous energy (IE) after a slam was above a threshold value. The IE is obtained by taking the amplitude of the signal with a real $g(t)$ and imaginary component $\hat{g}(t)j$. The IE is then calculated with Equation 7.1. Katsouros identified the threshold value as 0.1 $(m/s^2)^2$.

$$IE(t) = g^2(t) + \hat{g}^2(t) \tag{7.1}$$

What is interesting is the difference between the identifiers. The EMD-based and whipping-based methods identified mostly the same slamming events, although the EMD method identified more slams and a couple of events with significantly higher severity. The severity of identified events was thus inconsistent between the two methods. The whipping criteria yielded more consistent periods between more severe slamming events, ranging from 4 to 6 seconds.

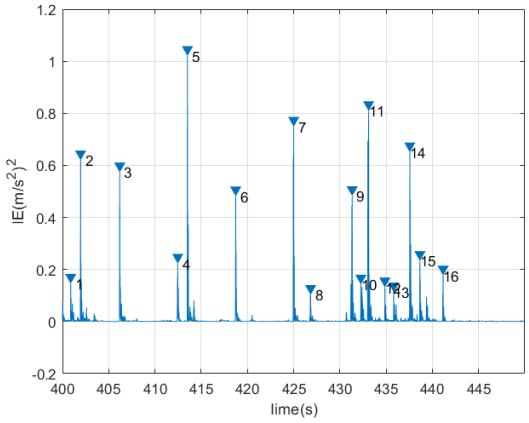

Figure 7.5: "Slamming events identified by the whipping criterion of run 5_76" [4]

Katsouros [4] found that while the EMD-based method overestimated the number of significant slams, the spacing of smaller slamming events is interesting to compare with immersion to see whether the proposed method is representative for the case at hand. Whilst the criteria of IE can be utilised to asses whipping occurrence in the numerical method as a result of a slam.

7.2. Numerical Case of Experimental Measurement

To obtain values which can be compared with the experimental measurements, it is essential to recreate the same case in close detail. The applied wave amplitude for the bichromatic case remained 0.0175, such that the largest wave height was 0.07 m. A couple of amendments were made to the previous modelling related to the draught and forward speed.

Draught of Experimental Model

As listed in Table 2.2, the weight of the flexible model was 9% higher than that of the full-scale plans on which the model was based. For accurate validation of the numerical model, it is then essential to use a draught that is representative of the higher weight. The new draught, at a weight of 15.89 kg, became 0.0632 m. The impact on the motions will likely remain limited as the geometry of the hull does not change significantly, and the hull above the waterline is primarily vertical on all sides. Nevertheless, the motions will also be recalculated for the investigated wave frequencies. A greater impact is expected on the immersion calculation. As the change in draught will result in a smaller air gap height. This will result in increased severity of immersion, but also increase its occurrence.

Inclusion of Forward Speed

In the proposed slamming model, the inclusion of forward speed is not resolved directly. Due to the small magnitude of the forward speed, it was assumed that an increase in the encounter frequency could approximate the motions. The frequency shift is calculated with Equation 7.2. The result is that the wave frequencies $\omega_1 = 4$ rad/s and $\omega_2 = 7$ rad/s become the wave encounter frequencies $\omega_{e,1} = 4.163$ rad/s and $\omega_{e,2} = 7.499$ rad/s. This frequency shift will result in slightly different RAOs and phasing of the motion, which is displayed in Table 7.2.

$$\omega_e = k(c + U) = \omega(1 + U \cdot \omega/g) \tag{7.2}$$

ω [rad/s]	RAO_{heave} [mm/mm]	$\epsilon_{heave}[rad]$	RAO_{pitch} [deg/mm]	$\epsilon_{pitch}[rad]$
4	0.9285	1.693e-03	1.693	1.625
4.163	0.9126	1.202e-03	1.819	1.630
7	0.3717	-0.3478	3.587	2.077
7.499	0.2718	-0.5327	2.961	2.161

Table 7.2: Effect of forward speed on wave frequency and resulting motions

7.2.1. Numerical Acceleration and Slamming Data

The accelerations of the numerical model are extracted for the positions of the eight different accelerometers. The accelerations resulting from the four flexible mode excitations and their sum are displayed in Figure 7.6. The accelerations are plotted during the slamming event. The accelerations are mainly affected during the force application, after the initial slam, the accelerations will reduce as the vibrations decay. What primarily can be extracted from Figure 7.6 is the order of magnitude of the accelerations resulting from the slam.

Smoothness of Accelerations

Additionally, some comments can be made on the acceleration signal. There is a sawtooth pattern in certain parts of the acceleration signal. This is the result of a combination of the pressure formulation and the mesh spacing. In Figures 6.13a and 6.13b, the points that represent the mesh longitudinal position were located in vertical groups with equal longitudinal position. The grouping of these centres and the $\frac{1}{\sqrt{c(t)^2 - x^2}}$ term in the pressure formulation results in larger modal forces in the first time step after a new group gets wetted. The modal force then reduces as the slam front moves away until the next group of panels, with equal longitudinal position, becomes wetted. This creates minor disruptions in the acceleration, which become more noticeable later in the slamming event. Later in the slam, the direction of the force can be opposite to the oscillatory movements.

Duration of Slam Event

Another effect that can be observed is limited modal excitation due to a prolonged wetting time. The wetting time of the slam event is 96 milliseconds, which is longer than the natural period of the flexible modes. When the slamming event is longer than half the natural period of the natural frequency, the contributions will partially negate the excitation. If a constant force were applied for exactly the wetting period, the resulting vibration response after the slam would be approximately zero. As a result, the flexible modes are only excited to a limited extent. Although there is still excitation of the modes as a result of increasing slamming pressures throughout the slamming event. Due to the longer duration, the vibration response is not excited efficiently. The peak accelerations found were on the order of 0.6 to 1.5 m/s^2 during the slamming event.

Pressure Definitions

In Section 6.2 and 6.3, a combination of two definitions for the wetted length and immersion velocity for the slamming pressure was proposed. All combinations are used in evaluating the accelerations, but no significant differences were found between the various definitions. Although the Linear c(t) definition did result in some erratic behaviour near the end of the slamming event. Thus, the quadratic c(t) and space-averaged slamming velocity $\overline{V}$ are used to compare the accelerations. The other acceleration data resulting from the various pressure formulations are shown in Appendix C.

On Accelerations During the Slamming Event

It should be noted that the accelerations in the calculated time frame for the measurements would include some local effects. This model does not accurately represent all the local effects. Therefore, it would be better to compare the accelerations of the different modes after the slamming event to the experimental peaks. This would lead to a more accurate comparison with the experiment, as the very high accelerations resulting from the slamming event were also filtered out in the flexible response of the experimental data. Assuming the structure remains oscillating with the corresponding accelerations and frequencies, the signal will then decay. The highest combined accelerations resulting from the four flexible modes at the accelerometers are calculated using Equation 7.3 and shown in Table 7.3. These absolute values are summed to indicate the highest acceleration possible; the measured values should be less than the numerical ones due to decay before the combination of the highest accelerations is reached.

$$\sum a_p = |a_{1,p}| + |a_{2,p}| + |a_{3,p}| + |a_{4,p}| \tag{7.3}$$

Table 7.3: Accelerations at the end of the slamming event of the four eigenmodes

sensor number p	$a_{1,p}$ $[m/s^2]$	$a_{2,p}$ $[m/s^2]$	$a_{3,p}$ $[m/s^2]$	$a_{4,p}$ $[m/s^2]$	$\sum a_p$ $[m/s^2]$
1	0.021	-0.2377	0.0009	-0.1133	0.3729
2	0.0154	1.5671	0.0187	-0.6368	2.238
3	-0.0151	0.1495	0.0031	0.718	0.8857
4	-0.0423	-1.0999	0.0215	-0.3078	1.4715
5	0.0265	-0.1868	0.0047	0.0714	0.2895
6	0.0254	1.2152	-0.0167	-0.2761	1.5333
7	-0.0004	0.0702	-0.0092	0.001	0.0808
8	-0.0304	-1.3501	-0.0075	-0.1599	1.5478

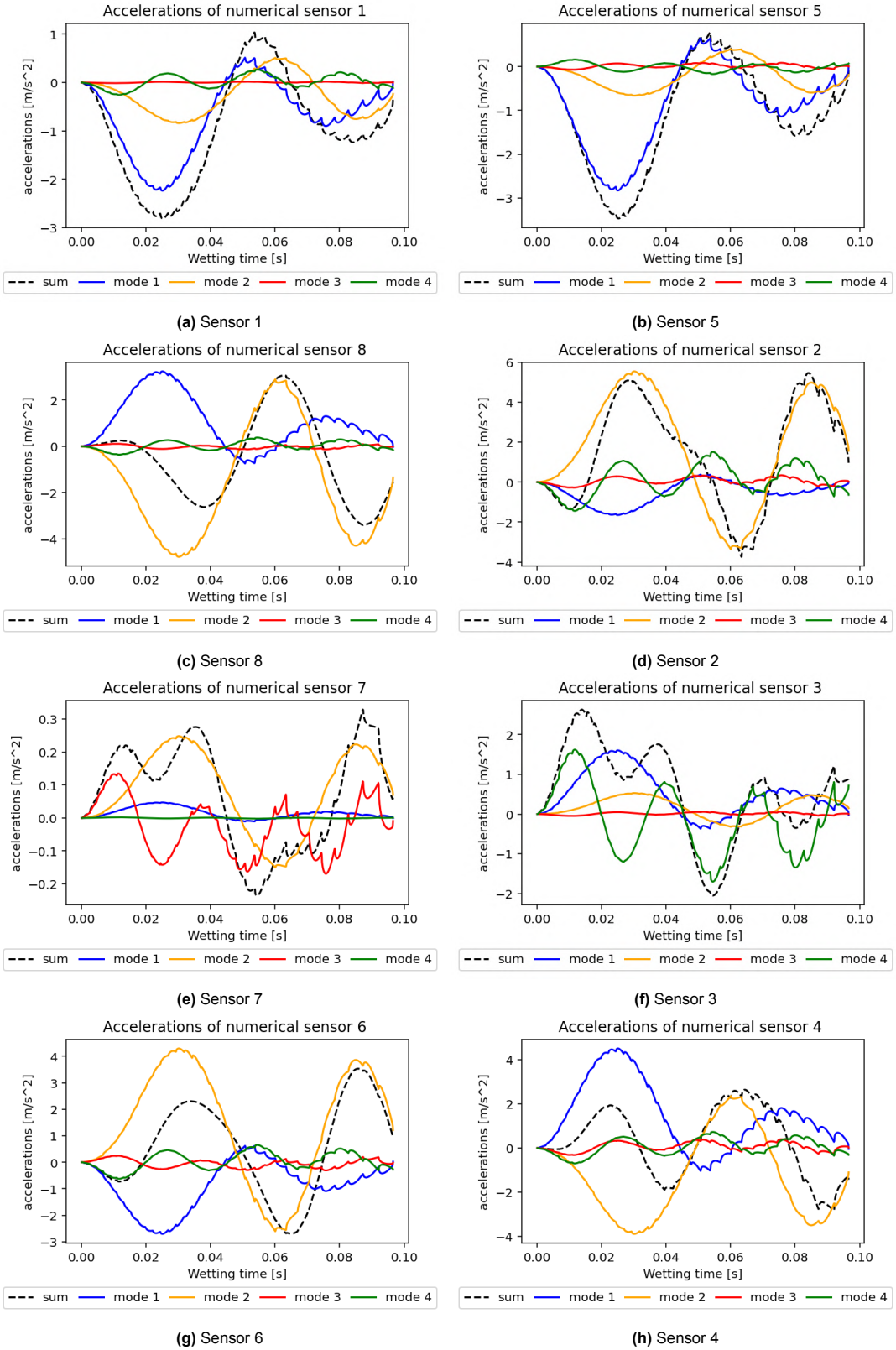

(a) Sensor 1 **(b)** Sensor 5

(c) Sensor 8 **(d)** Sensor 2

(e) Sensor 7 **(f)** Sensor 3

(g) Sensor 6 **(h)** Sensor 4

Figure 7.6: Numerical accelerations as a result of the first four flexible modes with pressure definition based on quadratic c(t) and space-averaged slamming velocity $\overline{V}$

7.2.2. Numerical Whipping Evaluation

The same criteria for Instantaneous energy from experimental measurements are applied to the numerical acceleration. When the IE exceeds 0.1 $(m/s^2)^2$, whipping effects occur as a result of the slam. The sum of absolute acceleration amplitudes is used, which is listed in Table 7.3. The sum of the amplitudes is utilised as the different modes each vibrate with their frequency. In an unfavourable condition, the most significant accelerations would then be the sum of all amplitudes. This is a conservative assumption, as damping effects would reduce the amplitudes before such an unfavourable condition occurs.

The condition is triggered for sensors 1, 2, 3, 4, 6 and 8. The greatest accelerations and thus whipping effects are found on the sensors located fore and aft on the demi-hulls. The structure was mainly excited by a significant mode two contribution, which involves vibrations of the demi hulls pitching in opposite directions. There is one problem with extending the whipping evaluation effects beyond this ship model. As the criteria on IE set at 0.1 showed whipping effects in this hull. However, it cannot be said with certainty that the criteria would be accurate for all flexible models. Through this method, further analysis is required to relate the accelerations and IE to stresses. Only with the resulting stresses can something meaningful be said about the whipping effects.

7.3. Comparison Between Numerical Method and Experimental Measurements

The resulting peak accelerations of the slamming impact are listed in Table 7.4. It can be seen that sensors 2, 4 and 6 yield approximately the same accelerations in both methods, while the numerical acceleration of sensor 8 is close to those of the first experimental slam. Accelerometers 2 and 8 are positioned near the port side bow and starboard bow, respectively. Accelerometers 4 and 6 are located aft in the starboard and port side demi-hull, respectively. The position of all accelerometers is listed in Figure 7.2 and Table 7.1. For all numerical accelerometers, the accelerations were less than the second peak of the experimental values. This was more noticeable in accelerometers 1, 3, 5, and particularly in 7. These accelerometers were located fore and aft in the cross deck (1 & 5) or in the centre of the demi-hulls (3 & 7).

Method	Sensor 1	Sensor 2	Sensor 3	Sensor 4	Sensor 5	Sensor 6	Sensor 7	Sensor 8
Experimental	[1.0-1.2]	[1.8-2.5]	[1.2-2.1]	[1.0-3.0]	[0.6-0.9]	[0.6-2]	[0.7-1.4]	[1.6-2]
Numerical	0.37	2.24	0.89	1.47	0.29	1.53	0.08	1.55

Table 7.4: Peak experimental accelerations [m/s^2] noted as [first-second] and numerical acceleration [m/s^2] values post-slam.

7.3.1. Differences Between Numerical Method and Experiment.

In the simplifying assumptions, a couple of modelling differences show up. In this section, the assumptions and their effects will be further discussed. To argue causes for differences between numerical and experimental results.

Connection Between Cross Deck and Demi-Hulls

The slamming is modelled on the flat part of the cross-deck. However, a quarter-circular plate connects the cross-deck to the wet deck. This plate is below the wet deck and would thus get immersed with a smaller relative motion due to a lower air gap height z_{AG}. Currently, no slamming force is applied to the area of this plate. This would then result in an underestimation of the total slamming force and the resulting accelerations. The force on the curved plate cannot be included in the proposed theory relating immersion to pressure. The theory is only valid for a flat plate geometry. This problem could be addressed by taking the instantaneous wetted surface into account, as will be further discussed in Chapter 9.

An additional effect of the radii is that it could lead to air introduction into the flow. If the slam propagates from the radius inwards, it could enclose the air. Air inclusion and effects related to wetting propagating from the demi-hulls inward are not modelled. The effects should be limited since the wave interactions for head waves cause slamming to start in the centre.

Experimental Bichromatic Waves

In the experimental measurements, a wave is created which does not perfectly represent a constant bichromatic wave. Due to friction on the walls of the flume tank, the wave amplitude varies slightly over the width of the tank. Additionally, the bichromatic frequency and wave height produced by the wave maker are not perfect, causing some variation in the wave loading applied. Both factors increase uncertainty, but it is not possible to determine whether they would cause overestimation or underestimation of the slamming forces and resulting accelerations.

Flexible Model

The flexible model, created by Keser [1], was made to represent a computer model of the heavy-lift catamaran. However, it is not a perfect representation of the initial computer model.
The vessel was not made all at once; segments were joined with epoxy. The numerical model used continuous properties and not segments joined with epoxy. In a 3D-printed flexible model, slight variations occur in the stacked layers along the vertical printing direction when compared to the properties in the printing direction. Lastly, lead was added to model the point masses. In the numerical model, the mass and connected plate were made to behave rigid; in the real flexible model, the masses and plates would behave somewhere in between fully flexible and fully rigid.

All these factors combined have an impact on the eigenmodes and frequencies of the model. There will therefore be an inherent difference between the numerical accelerometers and measured accelerations on the various sensors. This is evident in the numerical acceleration of sensor 7, which is close to zero due to the very low magnitude of the mode shape at that position. The experimental accelerations are much larger, likely a result of the actual mode shape values of the flexible being greater at that position.

Fore and Aft Slamming

In the case of bichromatic waves with wave encounter frequencies of 4.16 and 7.49 rad/s, the immersions are located at the front and aft of the wet deck. This means that the slam would also propagate onto the radius at the front of the wet deck. As previously mentioned, the definition of slamming pressure cannot include this part accurately. This would also result in an underestimation of the slamming forces. However, more importantly, slamming against the front of the cross-deck would cause forces in the longitudinal direction. The effect of longitudinal forces on modal excitation and motions varying as a result of the slam are both not included.

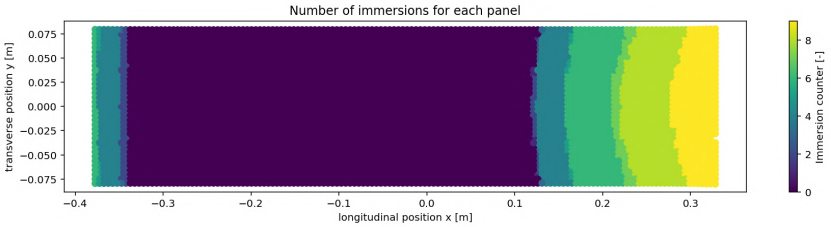

Figure 7.7: Number of immersions for bichromatic waves with frequencies $\omega_1 = 4.16$ and $\omega_2 = 7.49$ rad/s in a period of 14 seconds.

Validity of Motions in Frequency Domain After Slam

In the proposed method, it was assumed that the slamming impacts would cause only a limited influence on the motions. There is some uncertainty about whether this is an acceptable assumption. Mainly if slamming impacts occur on the front of the cross deck. If these slamming impacts disrupt the motions, a frequency domain solution of the slamming impacts and the resulting accelerations would not be accurate.

To check whether the motions are affected, the fore and aft immersions are compared, as shown in Figure 7.8 to the identified slamming events in Figure 7.4. Immersions of significant magnitude appear to occur approximately every 1.8 seconds in Figure 7.8a. However, due to the bichromatic interactions, there can also be periods of about 4 seconds with almost no slamming occurring. In the identified slamming events in Figure 7.4, a large slam occurs at 406 seconds. The next slam event occurs at 413 seconds; there is a 7-second period without any slamming events. It would appear that the motions are

then affected as a result of a slam. The proposed frequency domain method would then not accurately represent the experimentally measured values.

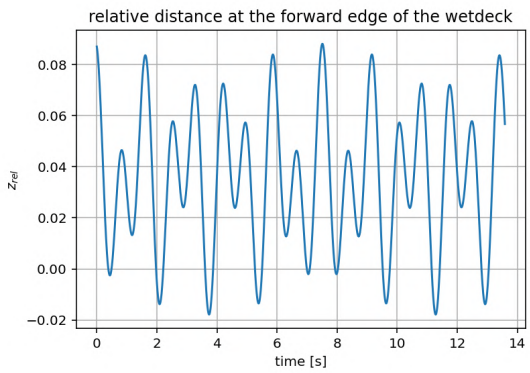

(a) Relative distance between water and the wet deck at the front of the wet deck.

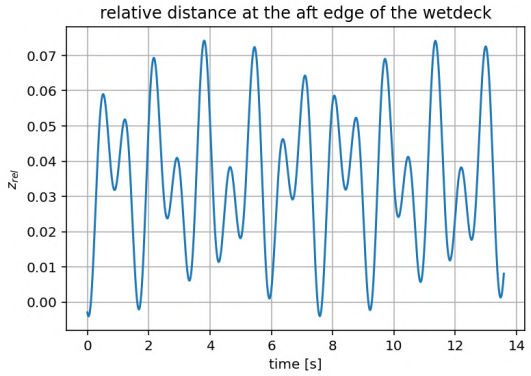

(b) Relative distance between water and the wet deck at the aft of the wet deck.

Figure 7.8: Relative distance over time, showing the regularity of slamming intervals.

7.3.2. Conclusions of Validating The Numerical Method

Overall, the numerical accelerations are underestimated compared to the experimental measurements. Various causes for the differences were identified. However, the proposed method did not account for the slamming effects in the motions. It was found, that a frequency-domain method relating slamming forces and accelerations can not be accurate due to the affected motions. With a time-domain method, it is possible to include the slamming forces in the motion. The proposed frequency-domain method could provide insight into the magnitude of the accelerations. Although slightly underestimating the accelerations, many different wave loading cases could quickly be evaluated. The ones that are found to be most problematic could then be further investigated with a method in the time domain. Further research could be conducted on the exact limitations where the proposed method no longer produces accurate results.

8. Conclusion

The goal of this thesis was to find a fast method to evaluate the global dynamic response resulting from excitation by wet deck slamming. The first chapter (1) discussed the available literature and its implications on the thesis, presented the research questions and provided a methodology.

In Chapter 2 the structural model of the catamaran is presented. A Finite Element Method (FEM) was applied to obtain the dry mode shapes and natural frequencies, the program used was 'ANSYS Mechanical'. The four flexible modes with the lowest natural frequencies were extracted. The FE model showed sufficient mesh convergence, providing a starting point for coupling to the hydromechanical model.

A hydromechanical model for wave loading and slamming pressure was introduced in Chapter 3. A Boundary Element Method (BEM) solver was applied to calculate the motion response to wave loading. The BEM solver used was 'Capytaine', a Python-based program that allows for the inclusion of flexible modal behaviour. A mesh convergence study was conducted, yielding reliable results for RAOs describing the ship's motions. There are limitations as the BEM solver does not evaluate water coming in contact with the wet deck; the immersion and slamming behaviour should be modelled with a different method. A theory is introduced that relates the wetted length over time and the immersion velocity to a slamming pressure.

Chapter 4 applies Capytaine and the dry mode shapes to obtain wet mode shapes and wet natural frequencies. Since the structural and hydromechanical mesh had different requirements, mapping of the dry modes to the hydromechanical mesh is required. Added mass contributions reduced the natural frequencies. The resulting wet mode shape calculation in Capytaine did result in a loss of local mode shapes. Therefore, the dry mode shapes are subsequently used for the displacements.

The immersion of the wetdeck as a result of monochromatic waves was investigated in Chapter 5. Expressions for relative wave height and relative velocity between the structure and the wave surface are introduced. Immersion events were found for various incoming waves. However, there was one problem with monochromatic wave loading. The waves would propagate and roll against the bottom of the wet deck, resulting in quite long wetting times and relatively slow increase of wetted length. The slam pressure theory described is unable to model such long immersions accurately since the vessel's motions change significantly throughout the event. Additionally, the resulting slams would likely result in minor excitation of flexible modes, as the wetting times are much longer than the natural periods of the flexible modes.

To induce shorter loading events, bichromatic waves were employed in Chapter 6. A superposition of two monochromatic waves resulted in immersion events with wetting times shorter than the natural periods of the flexible modes. For the time that spanned all unique combinations of the waves, some panels would experience more than one immersion. The largest relative immersion identified the most significant immersion event, which was subsequently used to model the slamming pressures. To obtain the pressures, a fit was made of the wetted length over time c(t) and the relative velocity at immersion. The fits showed some indication that a 2D wetted length propagation might not accurately represent the problem. The resulting slamming pressure was mapped to the modal space. With a 4th-order Runge-Kutta integration, the oscillatory displacements and accelerations were found. To investigate the decay, a damping coefficient was applied, which was representative of the structural model. The vibration response would decay before the next slamming impact occurred. There were no remaining effects that could be included in the subsequent slamming force evaluation.

In Chapter 7, the proposed numerical method for slamming response was validated against experimental measurements obtained from a fully flexible heavy-lift catamaran model. After creating a numerical case representative of the experiment, the accelerations and slamming intervals were compared. Overall, the numerical model captured the occurrence of slamming and the resulting vibration response;

however, it underestimated peak acceleration values compared to the experimental results. It was found that a large slamming event could disrupt the motions of the vessel, which can not be accurately resolved in the frequency domain. To achieve accurate displacement, acceleration, and stress predictions during severe slamming events, a time-domain analysis is necessary.

Although it is not possible to obtain the exact response, the proposed method can still be used in the early design stages of the catamaran. Due to short calculation time, it is possible to evaluate many different conditions, hull shapes or air gap heights. The values could be used as an indication of slamming severity and compared relatively to gauge the effect of different parameters.

In the next chapter 9, the recommendations for further research will be discussed. Further improvements or shortcomings will be explained in detail.

8.1. Discussion

The thesis aimed to develop a fast numerical method that relates slamming to dynamic response. This method is only viable for a slow-sailing vessel in head seas, but it provides a practical and computationally efficient method for evaluating the response. Numerous assumptions and their validity will be discussed in this chapter.

The method is only applicable in head waves because the flow below the wet deck will certainly include 3D effects when sailing under an angle. Additionally, BEM methods are not well-equipped to accurately model roll, as the assumption is that the viscosity is zero, and thus there is no friction, which damps the roll motion. In terms of fluid modelling, the irrotationality of the fluid is a pretty acceptable assumption. Minor vortices would occur in the flow. However, their impact will be negligible for short time scales. In terms of incompressibility, no air must be included in the flow. A requirement was set that the wedge impact angle must be greater than 5°, but this can not be verified in the calculation. It was found that the immersion was closer to a plate wave impact. In a plate wave impact, air inclusion is less problematic due to varying surface angle, but is not certainly eliminated.

For the dry modal analysis, no damping was included. However, for low damping and a short timescale, this is deemed quite acceptable. Only the first four modes are included with the assumption that higher mode shapes are not excited significantly. In literature, this has been found to be a common practice which still yields meaningful results. Nevertheless, the inclusion of additional modes would marginally increase the accuracy.

The slamming pressure derived from a Wagner momentum theory approach relates the wetted length and immersion velocity to the slamming pressure. The slamming events are required to be of short duration, which could only be achieved for bichromatic waves. Random seas might exhibit the same response as a bichromatic wave loading, but this could only be evaluated by taking the instantaneous wetted surface into account. Capytaine and many commercial BEM solvers are not well equipped to deal with such a problem. The other requirement for the frequency-based response calculated by BEM is that the slamming impacts do not significantly affect the global motions. This then mainly leads to an oscillatory dynamic response.

Regarding the wet modal frequencies, it was not possible to discretise the panels into the prescribed element size for the high frequencies of the higher-order flexible modes. Evaluating the wet properties at a lower frequency than the eigenfrequencies introduces a small error in the added mass and stiffness fluid effects. It would be more accurate to calculate the added mass and stiffness at the higher flexible eigenfrequency if the computation cost allowed it. Additionally, in this step the wet nodal flexible displacements of the entire structure are lost. Subsequent forces are, therefore, multiplied by the dry mode shapes. The added masses are calculated on a per-panel basis for all submerged panels. The resulting wet mode shapes take the total added mass into account and only reflect the wet mode shapes locally for the mean submerged hull. The local values are added to obtain the wet frequencies, but no mode shape data is available for the non-submerged hull. This requires the utilisation of dry mode shapes, which will impact the accuracy of the results, as the dry mode does not entirely represent the ship in the water.

There was the intention to include the flexible response back into the slamming impact. However, due to a combination of only limited excitation and considerable damping, there would be no impact of a previous slamming event on the subsequent one according to the numerical method. As previously mentioned, the experimental response did indicate effects of previous slamming events; however, these effects were related to the motions rather than the flexible response of the structure.

During the wetting time, when the force was applied, larger accelerations were found. These accelerations during the slamming event were ignored because, in the experiment, the measured accelerations were also filtered for the slam event. Additionally, the accelerations indicated by the summed response of the different modes are assured to be higher than the actual response since part of the signal will decay before the time is reached where all values are at their peak. The calculated accelerations are able to create insight. However, they should only be utilised to investigate different modelling parameters relative to each other in terms of slamming significance.

With all the flexible responses appearing to be relatively small, the flexible response to slamming has a negligible impact on the eventual slamming loads. In this case, a simpler, rigid analysis would not have yielded much different slamming pressures. Nevertheless, if the flexible behaviour is not modelled, it would also not be possible to find the flexible accelerations.

8.2. Research Questions

To conclude, the research questions set out in the research proposal (Section 1.4) will be answered. Resulting in a clear description of what this research found on the characteristics of the dynamic response of a heavy lift catamaran induced by wet deck slamming.

On the efficient numerical method for slam response

The proposed method is rather efficient, being able to indicate the slamming response within 30 minutes of calculation time. If many frequencies were to be tested, it could be worthwhile to optimise the code further. The size of the time steps could be optimised for convergence, using fewer time steps in the response calculation.

On the effect of two-way coupling on slamming-induced response

The proposed method was not able to apply a two-way coupling of the flexible response in the slamming events. This is a result of damping such that only a negligible flexible response remains for the next slamming event. Even if it were possible, the accuracy required for the timing is exceptionally high. The high frequencies result in very short natural periods, where the flexible response could either dampen or intensify the slamming event, depending on a slight change in timing that impacts the phase.

On the comparison of numerical slamming-induced response with experimental data

While the order of magnitude of accelerations is similar in some cases, it generally understates accelerations compared to measured values; the exact values should not be utilised for assessing the design load. Time-related effects play a role in the precise acceleration calculation, which are not well modelled in the frequency domain. The method can identify frequencies or cases that require further investigation using a time-domain approach. The application of the numerical method could still prove helpful in the design stages, not for exact load calculations, but in assessing the effect of design parameters on slamming severity by comparing their relative impact on accelerations.

On whipping effects for a heavy-lifting catamaran due to wet deck slamming

There is an indication that a whipping effect occurs when the same parameter as in the experimental setup is applied. However, the magnitude of the vibration response is relatively small; the most significant displacement found was 0.06 millimetres on the model scale. The resulting whipping effects would also have a minimal impact on the maximum load. Nevertheless, it does affect the fatigue life of the structure. Slamming causes cycles at a high frequency, and the slamming loads are added to the other loads applied. A high number of cycles with a base load can result in significant consumption of fatigue life in a short period. To assess whether whipping effects are problematic, a further fatigue analysis should be conducted for the design case.

9. Recommendations for future research

The presented thesis provides a fast numerical method to predict the dynamic response. It could be further improved regarding a couple of topics. For fluid modelling techniques, it would be a significant improvement to apply a BEM potential flow solver that uses the instantaneous wetted surface. Rankine sources should then be applied as the requirements of the Green function no longer hold for a changing wetted surface. It comes at a cost; the main benefit of being a fast calculation method would then be lost. The additional computation cost arises from the transient instantaneous wetted surface, which necessitates source strength calculations for every time step. At that point, it could be more attractive to apply for a RANS-based CFD programme. However, a benefit of BEM models is not to model the entire fluid, but rather to mesh the surface. In BEM, not meshing all the grids allows for easier coupling with vessel movements compared to CFD, as a result of not remeshing around the moving vessel. The frequency domain BEM method can still be used to determine the initial inputs for more complex calculations.

With modelling of the instantaneous wetted surface, it would become possible to determine the applied pressures directly through potential theory on the wetted part of the wet deck. This could prove to be more accurate than the current definition of pressure, approximating such effects.

An increased quality of dry mode mapping could further improve the wet modal results. Currently, at the boundary between different sections of the hull, there is no smooth transition. This inconsistency in displacement will certainly introduce a small error; however, with very small magnitudes of excitation, it may not yield significant improvements.

Another way to create a model closer to reality is to add the forward speed of the vessel. This will result in additional advection effects of the hull fluid interactions. As a result, there could be a difference in flow behaviour with more pronounced effects near the aft.

Due to some of the 3D effects that occurred in the bichromatic slam cases, it may prove interesting to model the wetted length definition in terms of multiple longitudinal strips. With the strips, the 3D effects can be partially included.

A way the structural model could be improved is to model the excitation of the modes at a local level. Determining the excitation of mode shapes on each panel propagating over time, which consequently excites the global response. The emphasis then lies more on the local effects occurring as a result of the slam. The vibration response could also be connected to the fluid model to include local vibration effects on the fluid loading. In the end, it might not be desirable to go into so much detail about the local effects. Due to the flexible modelling method for scaled stiffness, the internal structure is quite different and might not be representative of the local effects of the full-scale vessel.

Further experimental measurements can be conducted to determine the limits of the numerical model's slamming indication. However, with the magnitude of accelerations not aligning with the experimental measurements, it would be better to first put effort into developing a numerical model that can more accurately represent the slamming accelerations.

Another interesting topic that could be further researched is an investigation into different slams. For now, it was found that most of the flexible response would decay before the next impact. Here is the assumption of either mono or bichromatic wave loading. In a true random sea, there could be cases where there is still a flexible response when the next slam occurs. To model the waves of irregular frequency, a method in the time domain is once again suggested. In the time domain, wave loading cases could be simulated with closer subsequent slamming events. Such loading cases allow for further analysis of the flexible response to slamming events.

Bibliography

[1] A. Keser, "The design, production and verification of a fully elastic model of a catamaran for hydroelastic experiments," M.S. thesis, Delft University of Technolgy, 2023.

[2] G. Kapsenberg and E. Thornhill, "A practical approach to ship slamming in waves," in *28th International Symposium on Naval Hydrodynamics*, 2010. [Online]. Available: https://repository.tudelft.nl/record/uuid:0efd69ec-e0aa-4ff6-81e6-318137742b25.

[3] H. Bredmose, A. Hunt-Raby, R. Jayaratne, and G. N. Bullock, "The ideal flip-through impact: experimental and numerical investigation," *Journal of Engineering Mathematics*, vol. 67, no. 1-2, pp. 115–136, Nov. 2009. DOI: 10.1007/s10665-009-9354-3. [Online]. Available: https://doi.org/10.1007/s10665-009-9354-3.

[4] M. Katsouros, "Experimental Investigation of Wet-Deck Slamming on Fully Elastic Catamaran Model," M.S. thesis, Delft University of Technolgy, 2024.

[5] P. Shan, Y. Wang, F. Wang, J. Wu, and R. Zhu, "Froude–krylov nonlinear computations of three dimensional wave loads by a hybrid time domain boundary element method," *Ocean Engineering*, vol. 195, p. 106 763, 2020, ISSN: 0029-8018. DOI: https://doi.org/10.1016/j.oceaneng.2019.106763. [Online]. Available: https://www.sciencedirect.com/science/article/pii/S0029801819308674.

[6] D. Dessi, "Whipping-based criterion for the identification of slamming events," *International Journal of Naval Architecture and Ocean Engineering*, vol. 6, no. 4, pp. 1082–1095, Dec. 2014. DOI: 10.2478/ijnaoe-2013-0232. [Online]. Available: https://doi.org/10.2478/ijnaoe-2013-0232.

[7] A. Alsalah, D. Holloway, M. Mousavi, and J. Lavroff, "Identification of wave impacts and separation of responses using EMD," *Mechanical Systems and Signal Processing*, vol. 151, p. 107 385, Nov. 2020. DOI: 10.1016/j.ymssp.2020.107385. [Online]. Available: https://doi.org/10.1016/j.ymssp.2020.107385.

[8] A. Bereznitski, "Local hydroelastic response of ship structures under impact load (slamming)," Ph.D. dissertation, Technische Universiteit Delft, 2003.

[9] O. M. Faltinsen, "Hydroelastic slamming," *Journal of Marine Science and Technology*, vol. 5, no. 2, pp. 49–65, Jan. 2001. DOI: 10.1007/s007730070011. [Online]. Available: https://doi.org/10.1007/s007730070011.

[10] R. E. D. Bishop and W. G. Price, *Hydroelasticity of Ships*. Cambridge University Press, 1980. [Online]. Available: https://www.academia.edu/123485729/Hydroelasticity_of_Ships_R_E_D_Bishop.

[11] M. R. Davis and J. R. Whelan, "Computation of wet deck bow slam loads for catamaran arched cross sections," *Ocean Engineering*, vol. 34, no. 17-18, pp. 2265–2276, Jun. 2007. DOI: 10.1016/j.oceaneng.2007.06.001. [Online]. Available: https://doi.org/10.1016/j.oceaneng.2007.06.001.

[12] R. I. Julianto, T. Muttaqie, R. Adiputra, S. Hadi, R. L. L. G. Hidajat, and A. R. Prabowo, "Hydrodynamic and Structural Investigations of Catamaran Design," *Procedia Structural Integrity*, vol. 27, pp. 93–100, Jan. 2020. DOI: 10.1016/j.prostr.2020.07.013. [Online]. Available: https://doi.org/10.1016/j.prostr.2020.07.013.

[13] E. Haugen, "Hydroelastic analysis of slamming on stiffened plates with application to catamaran wetdecks," Ph.D. dissertation, Norwegian University of Science and Technology, 1999.

[14] Davis, B. French, and G. Thomas, "Wave slam on wave piercing catamarans in random head seas," *Ocean Engineering*, vol. 135, pp. 84–97, Mar. 2017. DOI: 10.1016/j.oceaneng.2017.03.007. [Online]. Available: https://doi.org/10.1016/j.oceaneng.2017.03.007.

[15] R. Hageman and I. Drummen, “Calculation of Structural Damping of the Global Hull Structure from In-Service Measurements,” in *Proceedings of the 14th International Symposium, PRADS 2019, September 22–26, 2019, Yokohama, Japan- Volume II*, Oct. 2020, pp. 345–364. DOI: 10.1007/978-981-15-4672-3\{_}22. [Online]. Available: https://doi.org/10.1007/978-981-15-4672-3_22.

[16] K. Iijima, T. Yao, and T. Moan, “Structural response of a ship in severe seas considering global hydroelastic vibrations,” *Marine Structures*, vol. 21, no. 4, pp. 420–445, Jul. 2008. DOI: 10.1016/j.marstruc.2008.03.003. [Online]. Available: https://doi.org/10.1016/j.marstruc.2008.03.003.

[17] F. Noblesse, “The Green function in the theory of radiation and diffraction of regular water waves by a body,” *Journal of Engineering Mathematics*, vol. 16, no. 2, pp. 137–169, May 1982. DOI: 10.1007/bf00042551. [Online]. Available: https://doi.org/10.1007/bf00042551.

[18] H. Wagner, “Über Stoß□ und Gleitvorgänge an der Oberfläche von Flüssigkeiten,” *ZAMM □ Journal of Applied Mathematics and Mechanics / Zeitschrift für Angewandte Mathematik und Mechanik*, vol. 12, no. 4, pp. 193–215, Jan. 1932. DOI: 10.1002/zamm.19320120402. [Online]. Available: https://doi.org/10.1002/zamm.19320120402.

A. Monochromatic immersions for ω of 9.5 rad/s and 10.1 rad/s

ω=9.5 rad/s

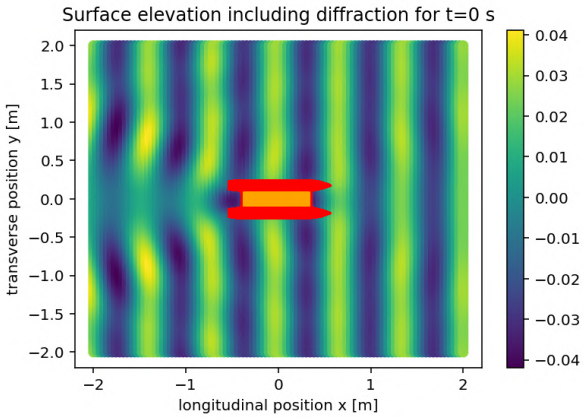

Figure A.1: Wave surface elevation around Catamaran in monochromatic waves with a frequency ω=9.5 [rad/s]

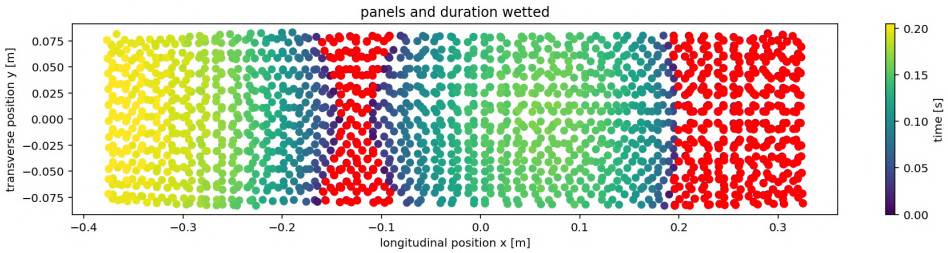

Figure A.2: Duration of immersion panels in one wave period, red panels were not immersed for ω=9.5 rad/s

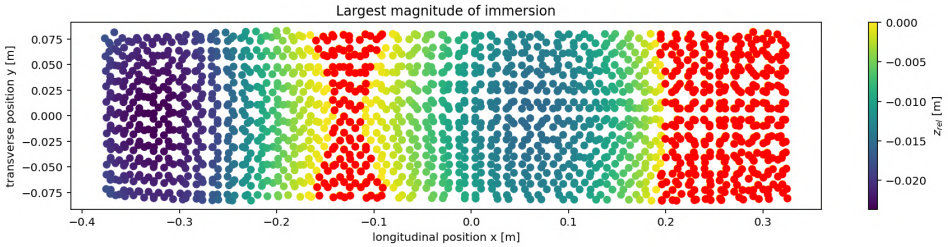

Figure A.3: Largest immersion experienced by each panel, red panels were not immersed for ω=9.5 rad/s

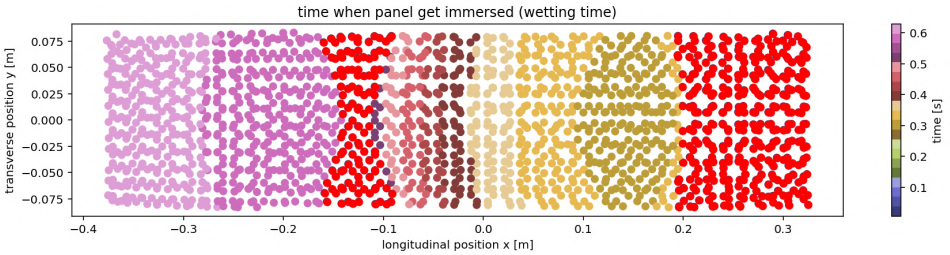

Figure A.4: Time of wetting for each panel, red panels were not immersed for ω=9.5 rad/s

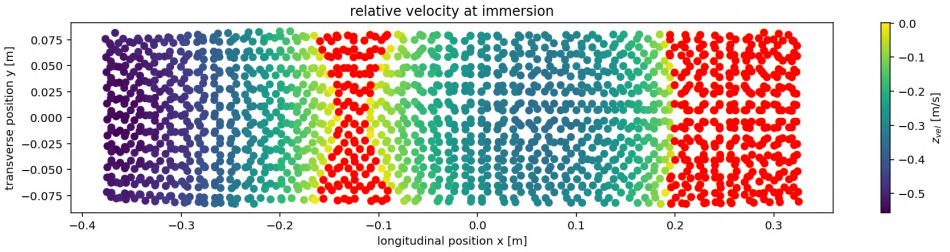

Figure A.5: Relative velocity between the water surface and the wet deck when the panels get immersed for ω=9.5 rad/s

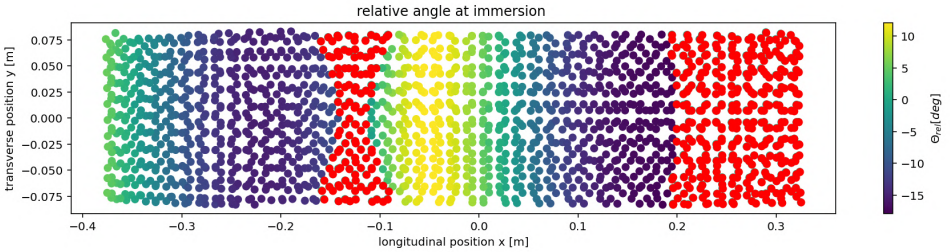

Figure A.6: Relative angle between the water surface and the wet deck when the panels get immersed for ω=9.5 rad/s

ω=10.1 rad/s

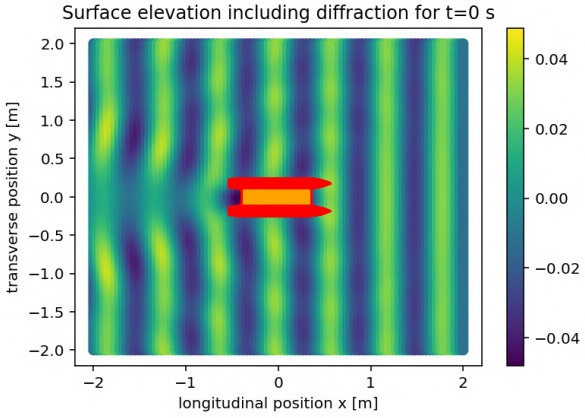

Figure A.7: Wave surface elevation around Catamaran in monochromatic waves with a frequency ω=10.1 [rad/s]

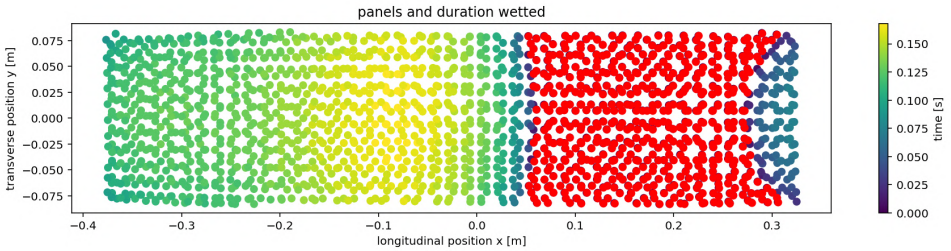

Figure A.8: Duration of immersion panels in one wave period, red panels were not immersed for ω=10.1 rad/s

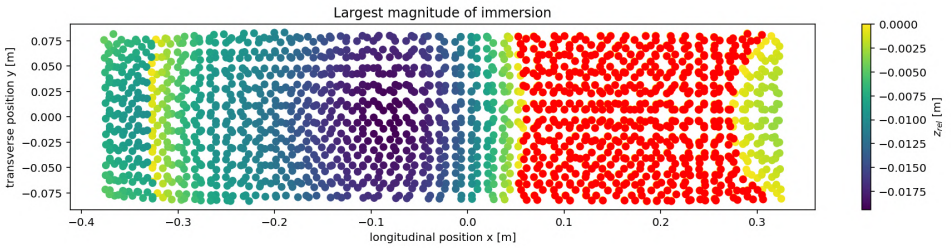

Figure A.9: Largest immersion experienced by each panel, red panels were not immersed for ω=10.1 rad/s

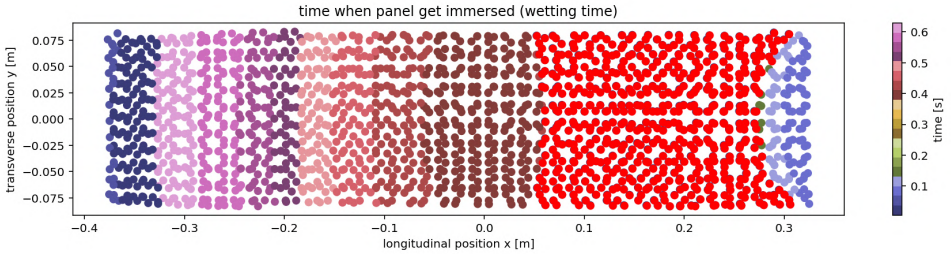

Figure A.10: Time of wetting for each panel, red panels were not immersed for ω=10.1 rad/s

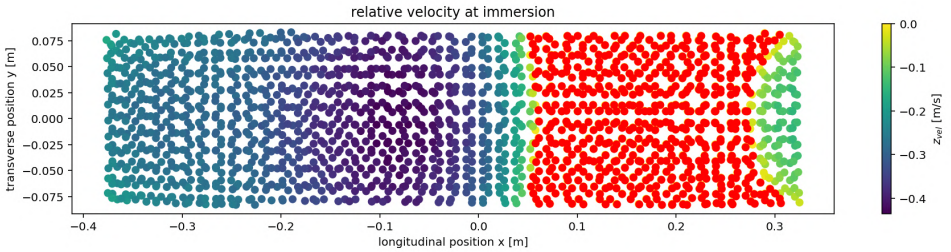

Figure A.11: Relative velocity between the water surface and the wet deck when the panels get immersed for ω=10.1 rad/s

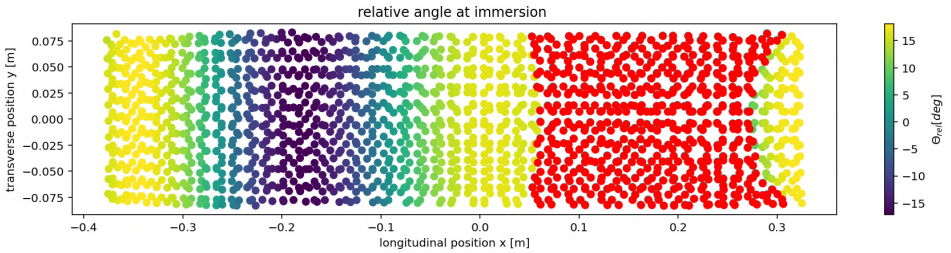

Figure A.12: Relative angle between the water surface and the wet deck when the panels get immersed for ω=10.1 rad/s

B. Slamming pressures on the wet deck from the various pressure formulations

Figures start on the next page due to the size requiring a full page.

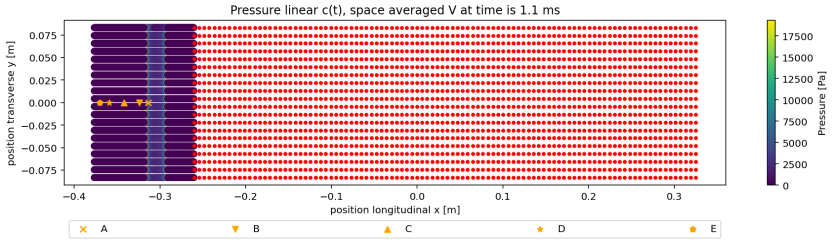

(a) Slamming pressure at 1.1ms into slam event

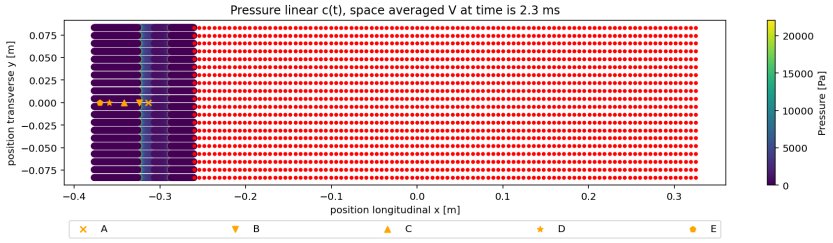

(b) Slamming pressure at 2.3ms into slam event

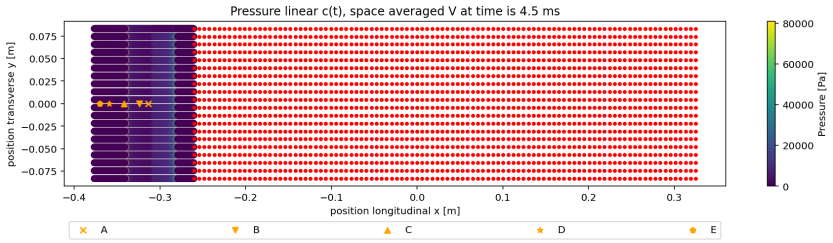

(c) Slamming pressure at 4.5ms into slam event

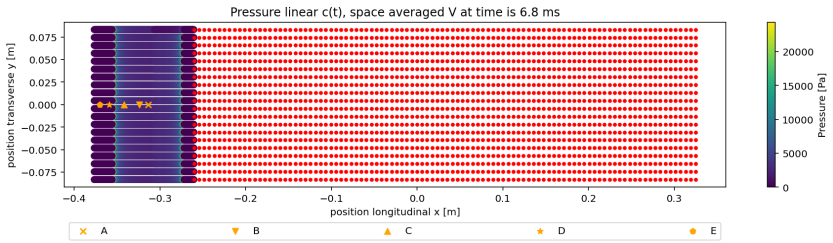

(d) Slamming pressure at 6.8ms into slam event

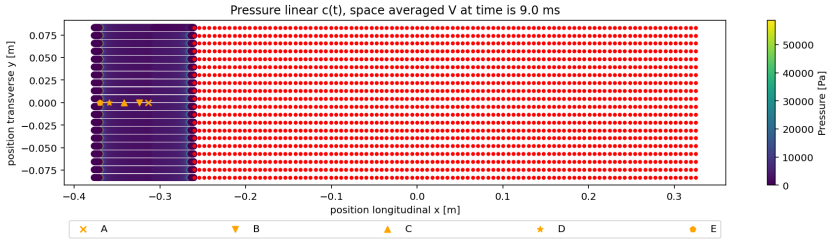

(e) Slamming pressure at 9.0ms into slam event

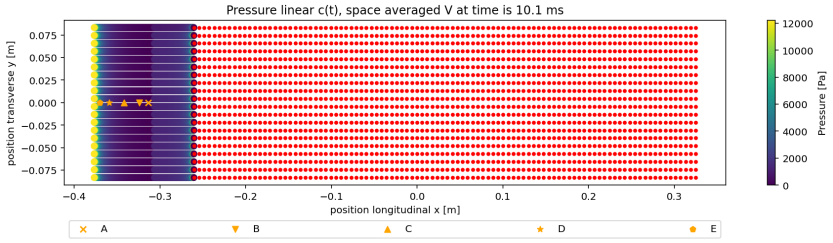

(f) Slamming pressure at 10.1ms into slam event

Figure B.1: Pressures during slamming event starting at t=5.9s, resulting from pressure definition based on linear c(t) and averaged slamming velocity $\overline{V}$

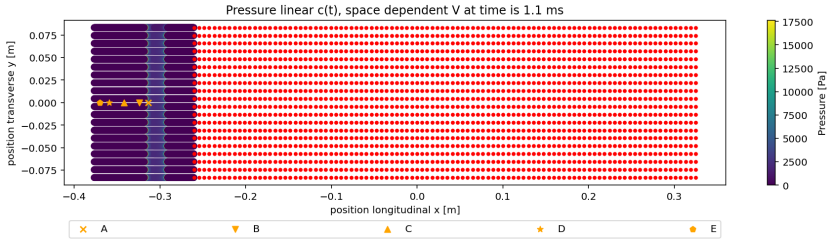

(a) Slamming pressure at 1.1ms into slam event

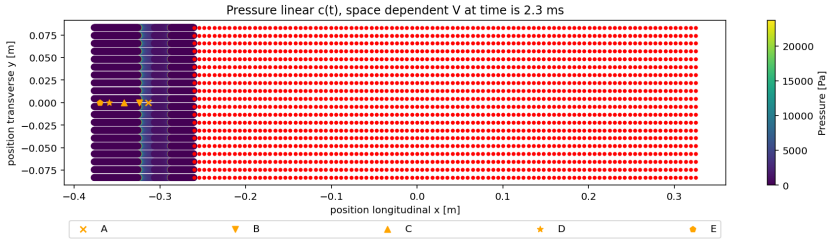

(b) Slamming pressure at 2.3ms into slam event

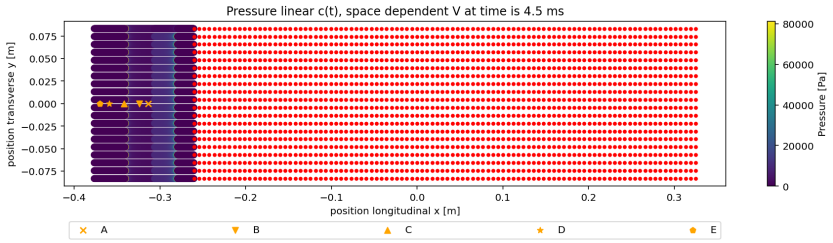

(c) Slamming pressure at 4.5ms into slam event

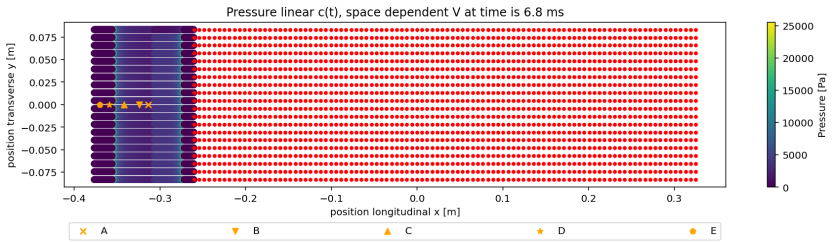

(d) Slamming pressure at 6.8ms into slam event

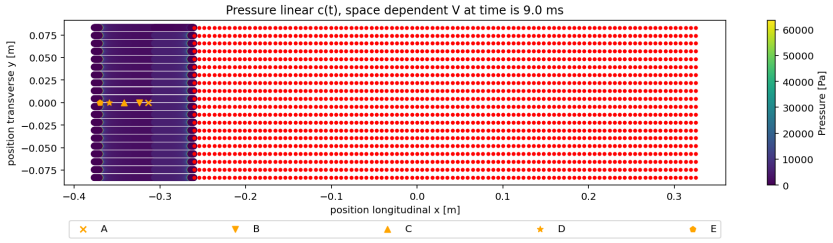

(e) Slamming pressure at 9.0ms into slam event

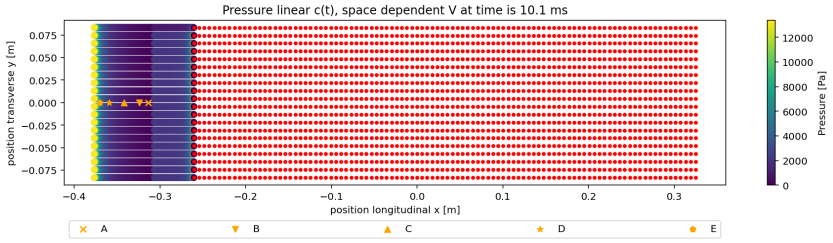

(f) Slamming pressure at 10.1ms into slam event

Figure B.2: Pressures during slamming event starting at t=5.9s, resulting from pressure definition based on linear c(t) and space dependent slamming velocity $V(x)$

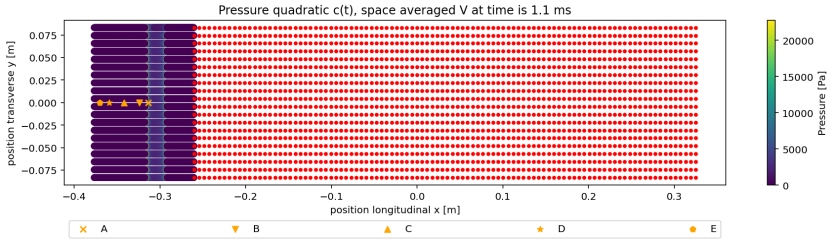

(a) Slamming pressure at 1.1ms into slam event

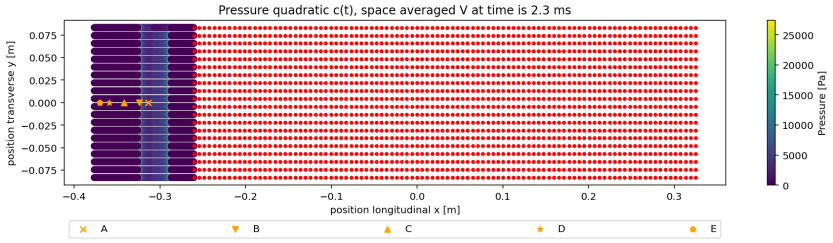

(b) Slamming pressure at 2.3ms into slam event

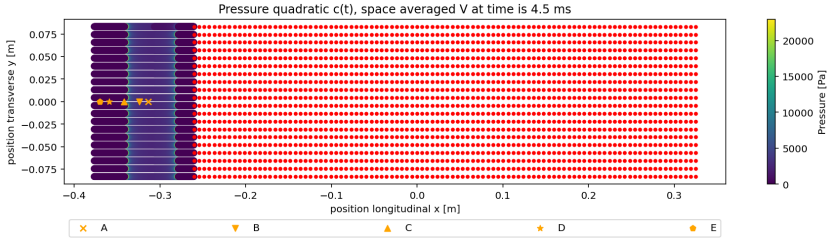

(c) Slamming pressure at 4.5ms into slam event

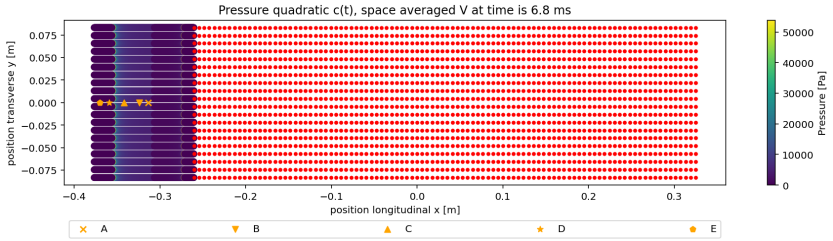

(d) Slamming pressure at 6.8ms into slam event

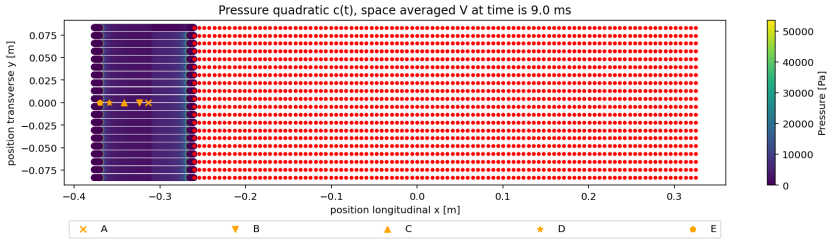

(e) Slamming pressure at 9.0ms into slam event

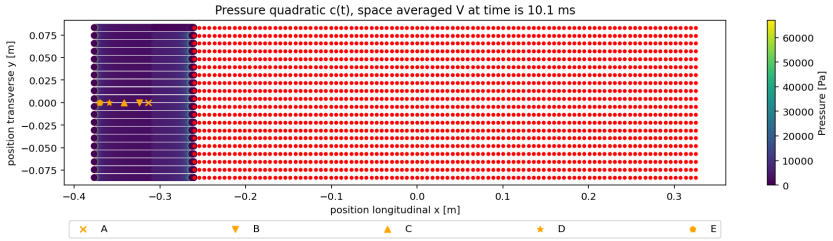

(f) Slamming pressure at 10.1ms into slam event

Figure B.3: Pressures during slamming event starting at t=5.9s, resulting from pressure definition based on quadratic c(t) and averaged slamming velocity $\overline{V}$

C. Accelerations of accelerometer locations for the various pressure formulations

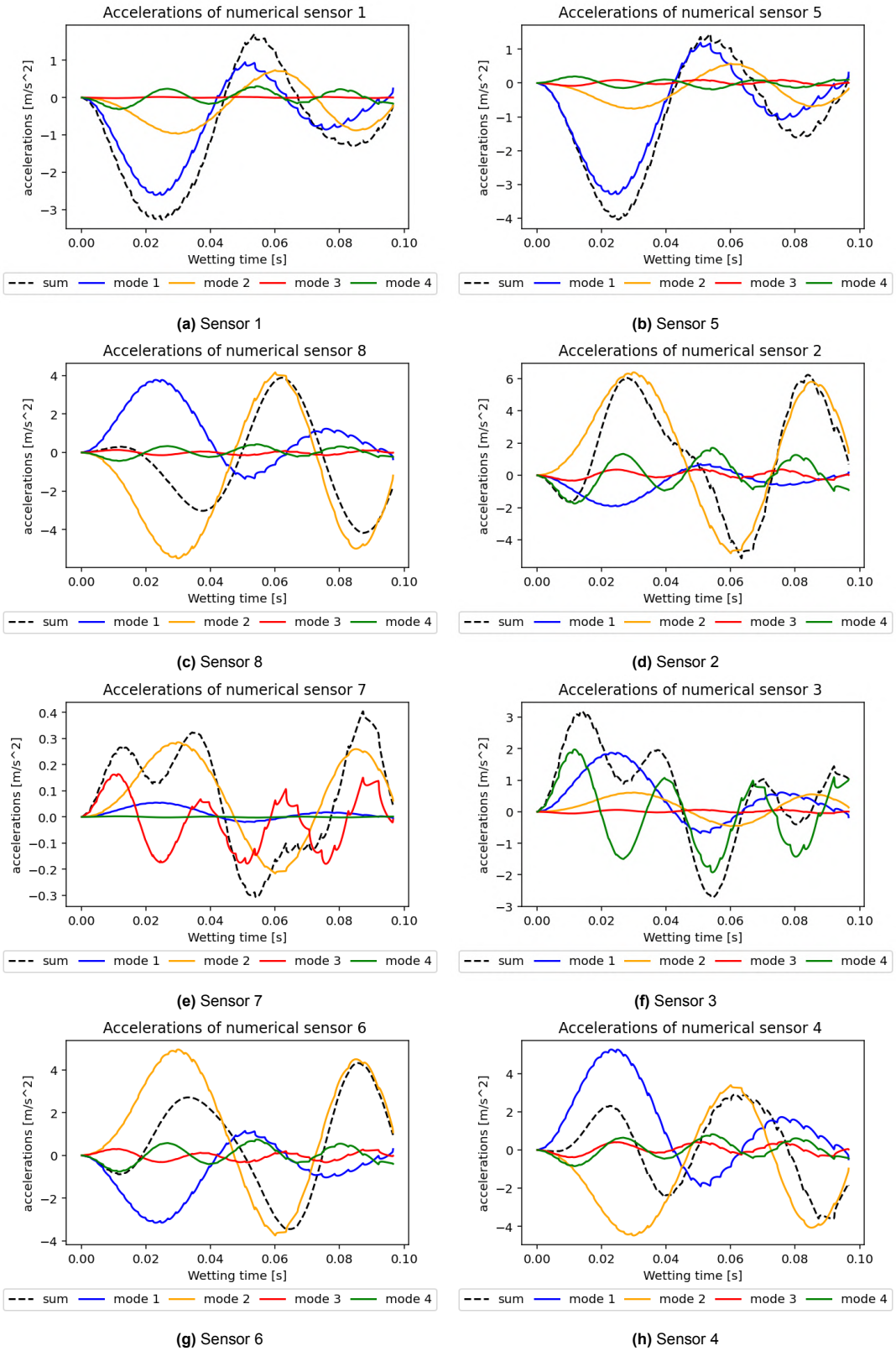

(a) Sensor 1 **(b)** Sensor 5 **(c)** Sensor 8 **(d)** Sensor 2 **(e)** Sensor 7 **(f)** Sensor 3 **(g)** Sensor 6 **(h)** Sensor 4

Figure C.1: Numerical accelerations as a result of the first four flexible modes with pressure definition based on quadratic c(t)

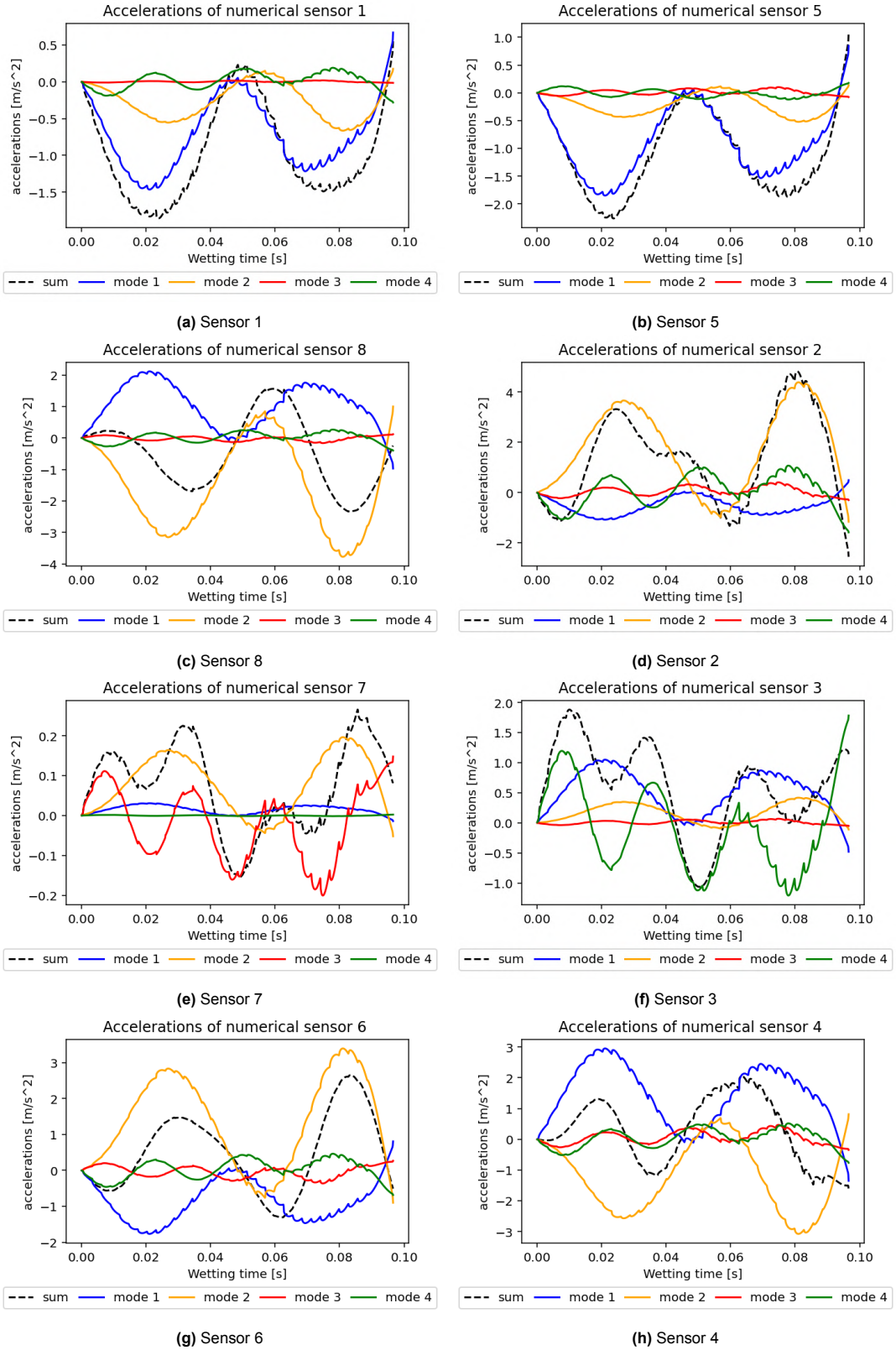

(a) Sensor 1 **(b)** Sensor 5

(c) Sensor 8 **(d)** Sensor 2

(e) Sensor 7 **(f)** Sensor 3

(g) Sensor 6 **(h)** Sensor 4

Figure C.2: Numerical accelerations as a result of the first four flexible modes with pressure definition based on linear c(t) and space-averaged velocity $\overline{V}$.